Testbeam studies on the LHCb Vertex Locator modules and a measurement of the mass of the reconstructed B_s meson

Thesis submitted in accordance with the requirements of the University of Liverpool for the degree of Doctor in Philosophy

by

Lisa Bernadette Dwyer

September 2009

UNIVERSITY OF LIVERPOOL

Abstract

The Large Hadron Collider at the European Organisation for Nuclear Research, CERN, is in its final stages of commissioning. The LHCb experiment is one of four experiments at the LHC. It will exploit the copious amounts of $b\bar{b}$ pairs produced to make precision measurements of the properties of B mesons. The real time identification of B mesons is provided by the Vertex Locator, designed and built by physicists and engineers at the University of Liverpool it is the primary tracking detector of the LHCb experiment. Testbeam studies of a subset of Vertex Locator modules found that the data taken with these modules exhibited the effects of crosstalk. A method for identifying, modelling and correcting the data for the effects of crosstalk has been developed. Results show that the channels on both R and ϕ sensors have approximately a 30 % anti-correlation with the channel that is read out immediately after it. The $B_s \rightarrow J/\psi(\mu^+\mu^-)\phi(K^+K^-)$ decay will have a clean experimental signature at the LHC. It is expected that in one nominal year of data taking 0.97 million $B_s \rightarrow J/\psi(\mu^+\mu^-)\phi(K^+K^-)$ signal events will be produced within the LHCb acceptance. A Monte Carlo study of this decay mode has found that it can be selected with an efficiency of 13 % and a signal to background ratio of 0.6. In $2fb^{-1}$, one nominal year's data, the estimated measurement of the B_s mass in this channel is $5.3686 \pm 0.0004\,GeV/c^2$, where $0.4\,MeV/c^2$ is the statistical error only.

In memory of my much loved grandparents:

Kathleen Duffy

and

William John Dwyer

Contents

List of Figures

List of Tables

Acknowledgements

I am immensely grateful to John Dainton and Themis Bowcock for giving me the opportunity to work on the LHCb experiment at the University of Liverpool. I also recognise that this PhD would not have been possible if it were not for the funding provided by STFC.

I would like to express my gratitude to my supervisor, Tara Shears, for her guidance and support throughout my PhD. Tara: you have been brilliant. Thank you!

I am greatly indebted to David Hutchcroft. Every aspect of the work outlined in this thesis has benefited from his time, patience and willingness to share his knowledge.

My thanks go to Girish Patel for answering my many questions related to the VeLo modules performance statistics.

I would like to thank my silicon gurus, Gianluigi Casse and Ilya Tsurin for their willingness to educate me in all things silicon. Thank you, also, to Tony Smith for answering my questions about the detector electronics.

My thanks go to Phil Turner and Mike Wormald who took me under their wing in the cleanroom and provided me with an excellent grounding and perspective with which to write about the VeLo.

Thanks to the terrible twosome of Dave Muskett and George Sim whose friendly faces and little chats during their visits to CERN were much anticipated. Dave also deserves thanks for dealing with my many batch farm incidents!

I would like to thank my fellow PhD students and office mates: Nick Austin, Ian Bingham, Mike Flowerdew, Paul Prichard, Abdi Noor, Craig Wiglesworth and Stephanie Donleavy for their friendship and interesting conversations, physics related and otherwise. Admittedly there have been more of the latter! Not forgetting the now Dr. AJ Rahmat, who always managed to liven the place up!

Special thanks my parents, Barbara and Brian, for their continued love, support and encouragement. Mum, Dad: without you both I'd never have made it this far. Thank you for everything! Thanks also to my sister, Jenny, and brother, Andrew, for putting up with me all these years! My thanks go to fiancé, David, for his love and support throughout and for never complaining when he was made to listen to my prattling about this thesis.

Lastly, but by no means least I'd like to thank Molly for always being there to give kisses. My theory chapter was so much easier to write with your company and willingness to be dragged out for a walk during my numerous breaks. I love you Mol!

Chapter 1

Introduction

In the Big Bang Model of the Universe matter and antimatter were created in equal quantities. Today our Universe is matter dominated. Matter and antimatter are known to have the same mass, meaning that when they come into contact with each other they annihilate. Why a small but significant amount of matter has survived to create us and the Universe we live in remains unknown. It is believed that there is a subtle difference between them that will provide an explanation for this asymmetry.

In particle physics knowledge of nature at small scales is obtained by accelerating particles to high energies and colliding them together. The Large Hadron Collider at CERN is in its final commisioning stages and will become the world's most powerful particle acceleration facility. It will collide two beams of protons each with an energy of 7 TeV to recreate the conditions that existed in our Universe one billionth of a second after it was created. The LHCb experiment will study the copious amounts of beauty (b) quarks and their antiparticle, $\bar{\mathrm{b}}$, that will be produced. These are unstable short lived particles that will travel approximately one millimetre on average before decaying into other particles. It is believed that studying the differences between the decay of b and $\bar{\mathrm{b}}$ quarks will lead to a better understanding of why nature prefers matter and not antimatter.

The LHCb experiment will make precision studies of the B_s meson system. The B_s meson is composed of a b and s quark-antiquark pair. It has the ability to oscillate into its antiparticle, $\bar{B}_s$, via a process known as B_s mixing. This mixing gives rise to two

eigenstates; heavy and light that are an admixture of the B_s and $\bar{B}_s$ mesons, and have a mass difference of Δm_s. At the LHC the $B_s \rightarrow J/\psi(\mu^+\mu^-)\phi(K^+K^-)$ decay channel will have a clean experimental signature and will enable LHCb to make competitive measurements of both the average mass of the B_s meson and the mass difference between the two eigenstates.

The precise measurement of the production and decay positions of b and $\bar{b}$ quarks is provided by the Vertex Locator. This detector is the principal component of the LHCb tracking system and has been designed and built by physicists and engineers at the University of Liverpool. The quality assurance and performance of the Vertex Locator modules accounts for a significant part of the author's PhD and that is reflected within this thesis.

This thesis summarises the studies of the author during a four year period and is structured as follows:

Chapter 1 introduces the Standard Model of Particle Physics, a theoretical framework that describes fundamental particles and their interactions. The mechanism by which Charge Parity violation is introduced into the Standard Model and how this is tested is discussed. The motivation for making a measurement of the mass of the B_s meson and recent theoretical predictions via lattice QCD is also provided.

Chapter 2 provides an overview of the LHC, concentrating on the LHCb experiment and its subdetctors. The Vertex Locator is discussed in some detail. A discussion of the LHCb trigger system and software framework is also provided.

Chapters 3 and 4 are dedicated to the analysis of data taken with a subset of the final production Vertex Locator modules during a testbeam in 2006. Chapter 3 discusses a method of identifying, quantifying and removing the effects of crosstalk seen in the testbeam data. In Chapter 4 the experimental signal to noise ratio of the silicon sensors is determined and compared to theoretical values.

In **Chapter 5** the selection of the $B_s \rightarrow J/\psi(\mu^+\mu^-)\phi(K^+K^-)$ decay is discussed and a

measurement of the average mass of the B_s meson is extracted.

Chapter 2

Theoretical Overview

2.1 Introduction to Standard Model

The Standard Model of Particle Physics is a theoretical framework, which describes elementary particles and their interactions via the electro-weak and strong forces. The elementary particles are the constituents of matter, they are point-like and are known to be *fermions*. The forces between fermions are carried by *vector bosons*.

The fundamental fermions are half integer spin particles and are sub-divided into *leptons* and *quarks*. Three flavours of leptons are postulated in the Standard Model; electron (e), muon (μ) and tau (τ), each have a neutral partner, the neutrino (ν). Six flavours of quarks are believed to exist; up (u), down (d), charm (c), strange (s), truth(t) and beauty (b). Quarks possess a colour charge, of which three types are postulated in the Standard Model; red, blue and green.

Both leptons and quarks are arranged into three generations as shown in Table 2.1.

The fundamental vector bosons are the mediators of the electro-weak and strong forces. The electro-weak force has two components, the electromagnetic and weak interactions. Electromagnetic interactions are conveyed by the exchange of a massless photon, whereas the weak component is carried by the massive $W^{\pm}$ and Z bosons. The strong force is mediated by eight massless gluons, like quarks these also carry colour charge. The vector bosons of the Standard Model are summarised in Table 2.2.

Fermions b	Generations			Charge
	I	II	III	
Leptons	e	μ	τ	-1
	ν_e	ν_μ	ν_τ	0
Quarks	u	c	t	$+\frac{2}{3}$
	d	s	b	$-\frac{1}{3}$

Table 2.1: The fermions of the Standard Model.

Boson	Charge	Force
Photon	0	Electromagnetic
$W^{\pm}$	± 1	Weak
Z^0	0	Weak
Gluon	0	Strong

Table 2.2: The vector bosons of the Standard Model.

Although very successful the Standard Model is incomplete. For example, gravity is not accommodated in the Standard Model, and the matter-antimatter asymmetry observed in our Universe can not be accounted for.

2.2 The Standard Model as a gauge theory

Mathematically, the Standard Model is a quantum field theory in which the electro-weak and strong interactions are discussed in terms of *gauge theories.* A gauge theory is invariant under a set of local transformations, these are transformations in which the parameters are space-time dependent. The Standard Model is said to be a theory in which the Electro-Weak theory and Quantum Chromodynamics are unified into a structure denoted by the gauge groups SU(3)⊗SU(2)⊗U(1).

Three gauge theories will be discussed in this section; Quantum Electrodynamics, Quantum Chromodynamics and the Electro-Weak theory.

2.2.1 Quantum Electrodynamics

Quantum Electrodynamics (QED) [1] is the quantum field theory that describes electromagnetic interactions. The Lagrangian of QED transforms under the U(1) group, where the 1 indicates that it describes all 1×1 unitary matrices.

The Lagrangian form of the Dirac equation for a free particle of mass, m and spin $\frac{1}{2}$, is given in Equation 2.1, where ψ is the wave function of the fermion, γ^μ are the gamma matrices [29] and ∂_μ is the partial derivative with respect to μ.

$$\mathcal{L} = \bar{\psi}(i\gamma^\mu\partial_\mu - m)\psi \tag{2.1}$$

It is invariant under *global* (space-time independent) phase transformations of the fermion field, meaning that $\psi \rightarrow e^{-i\omega}\psi$ and $\bar{\psi} \rightarrow e^{-i\omega}\bar{\psi}$, where ω is the phase. However, it is not invariant under *local* gauge transformations (space-time dependent). To restore gauge invariance an additional term must be added to the Lagrangian. It is assumed that the fermion field interacts with a vector field, A_μ, this is known as the *gauge field* and represents the coupling between a photon and a fermion with charge, e. The interaction term is given by:

$$-e\bar{\psi}\gamma^\mu A_\mu\psi \tag{2.2}$$

This term transforms under local gauge invariance as:

$$A_\mu(x) \rightarrow A_\mu(x) - \frac{1}{e}\partial_\mu\omega(x) \tag{2.3}$$

The propagation of the field A_μ is described by the addition of a kinetic term, $\frac{1}{4}F_{\mu\nu}F^{\mu\nu}$, that does not break the invariance of the QED Lagrangian under gauge transformations. The field strength tensor, $F_{\mu\nu}$, is given by:

$$F_{\mu\nu} = \partial_\mu A_\nu - \partial_\nu A_\mu \tag{2.4}$$

A covariant derivative, D_μ, can be defined as:

$$D_\mu = \partial_\mu + ieA_\mu \tag{2.5}$$

The resultant QED Lagrangian density is given in Equation 2.6.

$$\mathcal{L} = \bar{\psi}(i\gamma^\mu D_\mu - m)\psi - \frac{1}{4}F_{\mu\nu}F^{\mu\nu} \tag{2.6}$$

The application of a local U(1) gauge transformation yields the vector field A_μ, which can be identified as the propagator of the electromagnetic force - the photon.

2.2.2 Quantum Chromodynamics

Quantum Chromodynamics (QCD) [3] is a non-abelian gauge theory that describes the strong interaction. Gauge invariance of a non-abelian theory in which the elements of the group do not commute, is achieved by the addition of n^2-1 gauge bosons for SU(n). QCD is based upon the preservation of gauge invariance of the $SU(3)_C$ group, where C denotes the colour quantum number, and, therefore, requires eight massless gauge fields known as *gluons*. These are the propagators of the strong force. Gluons carry a colour charge, which means that they are able to couple to each other.

The Lagrangian density for QCD is constructed analogously to that of QED (see Section 2.2.1). The complete expression for the QCD lagrangian density is given in Equation 2.7.

$$\mathcal{L} = \sum_f \bar{q}_f(x)(i\gamma_\mu D^\mu - m_f)q_f(x) - \frac{1}{4}F^a_{\mu\nu}(x)F^{\mu\nu}_a(x) \tag{2.7}$$

It is written in terms of quark fields, $q(x)$, and is summed over the quark flavours, f. The mass of a quark with flavour, f, is denoted by the term m_f. The covariant derivative, D^μ, is defined as:

$$D^\mu q(x) = \left(\partial_\mu - ig_s\left(\frac{\lambda_a}{2}\right)A_\mu\right)q(x)$$

where g_s is the gauge coupling constant, A^a_μ represents the eight gluon fields and $\frac{\lambda_a}{2}$

denotes the SU(3) generators [4].

The kinetic term $\frac{1}{4}\mathrm{F}^{a}_{\mu\nu}(x)\mathrm{F}^{\mu\nu}_{a}(x)$ contains the field strength tensor, $\mathrm{F}^{a}_{\mu\nu}(x)$, of the gluon field, A^{a}, which is defined by Equation 2.8.

$$F^{a}_{\mu\nu}(x) = \partial_{\mu}A^{a}_{\nu} - \partial_{\nu}A^{a}_{\mu} - \sqrt{4\pi\alpha_s} \cdot f^{abc}A^{b}_{\mu}A^{c}_{\nu} \tag{2.8}$$

The term f^{abc} are the structure functions for the $\mathrm{SU}(3)_C$ algebra, where the indices a, b, c run from one to eight. The strong coupling constant, α_s, is given in Equation 2.9.

$$\alpha_s = \frac{g_s^2}{4\pi} \tag{2.9}$$

Quark confinement and asymptotic freedom

The QCD theory possesses two important features; *asymptotic freedom* and *quark confinement*. Asymptotic freedom describes how inside hadrons, where the quarks are closely confined, the forces between them are weak and asymptotically approach zero, meaning that the quarks behave as essentially free objects. As the quarks are pulled apart the binding between them increases such that at a point it becomes energetically more favourable to create a quark-antiquark pair than to isolate an individual quark. This mechanism is known as quark confinement and explains why quarks can not be observed freely.

2.2.3 Electro-Weak theory

The Electro-Weak gauge theory is a unified theory of the electromagnetic and weak interactions. It transforms via the $\mathrm{SU}(2)\otimes\mathrm{U}(1)_Y$ group [5][6][7]. The weak hypercharge, Y, is related to the charge, Q, and the third component of the weak isospin, I_3, by Equation 2.10.

$$Q = I_3 + \frac{Y}{2} \tag{2.10}$$

The propagators of the electro-weak interaction are four gauge fields B_{μ}, W^{1}_{μ}, W^{2}_{μ} and W^{3}_{μ}. B_{μ} is required to maintain invariance under electromagnetic transformations (U(1)), whereas W^{1}_{μ}, W^{2}_{μ} and W^{3}_{μ} conserve invariance under weak transformations

(SU(2)).

The weak interaction violates parity, meaning that the helicity, H, of a fermion is not conserved, which in turn means that there is no symmetry between left-handed (H=-1) and right-handed (H=+1) fermions. Thus, the Dirac field of a fermion can be separated into left-handed and right-handed components, with each generation of leptons and quarks represented by left-handed doublets and right-handed singlets. This grouping is illustrated by considering the first generation of fermions:

$$q_L \equiv \begin{pmatrix} u_L \\ d_L \end{pmatrix} \; ; \; u_R, \; d_R \qquad l \equiv \begin{pmatrix} e_L \\ \nu_L \end{pmatrix} \; ; \; e_R$$

The subscripts L and R denote the left-handed and right-handed fermions, respectively. Note that the right-handed neutrino is not shown. The Standard Model postulates a massless neutrino and although observations have proved the neutrino to carry a mass [8] this section considers the traditional Standard Model Lagrangian only, and it is therefore omitted.

SU(2) singlets are invariant under SU(2) transformations, and therefore, do not couple to the corresponding gauge bosons.

Spontaneous Symmetry Breaking

The invariance of a gauge theory requires that the gauge field is massless. Experimental observations have found that the W and Z bosons are massive [9]. This is explained by the introduction of the *Higgs Mechanism*, which postulates the existence of a weak isospin doublet of four complex scalar fields known as the *Higgs fields*. The Higgs fields have a non-zero expectation value for the potential. The ground state is degenerate with an infinite number of solutions. Choosing a solution arbitrarily breaks the electro-weak symmetry and is an example of *Spontaneous Symmetry Breaking* [10][11][12]. The spontaneous symmetry breaking process causes the weak gauge bosons to acquire a mass.

The Higgs mechanism results in the physically observed massive weak gauge bosons

being an admixture of the massless fields associated with the electromagnetic and weak interactions. The $W^{\pm}$ bosons are related to the fields W^1 and W^2 via Equation 2.11.

$$W_{\mu}^{\pm} = \frac{1}{\sqrt{2}}(W_{\mu}^{1} \mp W_{\mu}^{2}) \tag{2.11}$$

The physical fields Z_{μ}^{0} and A_{μ} are related to W_{μ}^{3} and B_{μ} via Equation 2.12, where θ_W is the Weinberg angle. Z_{μ}^{0} and A_{μ} can be written explicitly as shown in Equations 2.13 and 2.14, respectively.

$$\begin{pmatrix} Z_{\mu} \\ A_{\mu} \end{pmatrix} = \begin{pmatrix} \cos\theta_W & -\sin\theta_W \\ \sin\theta_W & \cos\theta_W \end{pmatrix} \begin{pmatrix} W_{\mu}^{3} \\ B_{\mu} \end{pmatrix} \tag{2.12}$$

$$Z^0 = W_{\mu}^{3}\cos\theta_W - B_{\mu}\sin\theta_W \tag{2.13}$$

$$A_{\mu} = W_{\mu}^{3}\cos\theta_W + B_{\mu}\sin\theta_W \tag{2.14}$$

Spontaneous symmetry breaking and the Higgs mechanism is said to be responsible for the way in which all fermions acquire a mass.

Quark mixing

In the quark sector quarks are admixtures of the mass and weak isospin eigenstates. The degree of admixture can be described quantitatively by the Cabbibo-Kobayashi-Maskawa matrix. This is discussed further in Section 2.4.

Electroweak Lagrangian

The complete Lagrangrian density for the electro-weak theory has three components; the Lagrangian due to fermionic interactions, the Lagrangian due to the interactions of the massless gauge bosons and the Lagrangian that describes the Higgs mechanism.

2.3 Symmetries in Particle Physics

The relationship between the laws of conservation and symmetries of nature is a fundamental principle in physics. There are two types of symmetries; continuous and discrete. Noether's theorem [13] states that if a physical system is invariant under a

continuous transformation there exists a conservation law associated with that quantity. For example, the laws of physics are invariant under time translation, which leads to the conservation of energy.

In contrast discrete symmetries can be broken under certain physical interactions. The discrete symmetries of charge conjugation, parity and time reversal are important in particle physics.

- **Charge Conjugation (C)** inverts the sign of all internal quantum numbers of a particle, therefore, changing a particle into its anti-particle.
- **Parity (P)** inverts the sign of the space co-ordinate system, thus changing a left-handed particle into a right-handed particle.
- **Time reversal (T)** reverses the momenta and angular momenta of a particle, thus inverting the sign of the time co-ordinate system.

The electromagnetic and strong interactions are invariant under C, P and T transformations. The combined C and P symmetries have been found to be non-invariant under certain conditions in the weak interaction. This is known as *CP violation.* It was first observed in the kaon system [14] by J. W. Cronin and V. L. Fitch in 1964 and can also be seen in the B meson system [15].

2.4 Cabbibo-Kobayashi-Maskawa matrix

The Cabbibo-Kobayashi-Maskawa (CKM) matrix [16][17] describes mathematically the rotation between the weak eigenstates (d, s, b) and mass eigenstates ($d^{'}$, $s^{'}$, $b^{'}$) of quarks and parameterises the mixing between the three quark generations. This relation is shown in Equation 2.15. Each element corresponds to the possible quark transitions and represents the strength of the weak charged current coupling between the quark flavours. The element V_{ij} represents the coupling of the i^{th} up-type quark to the j^{th} down-type quark. Experimental observations show that charged weak transitions between quarks of the same generation are common, whereas transitions between different quark generations are rare. Thus meaning that the diagonal terms of the CKM matrix are empirically close to one whilst the off-diagonal terms are small.

$$\begin{pmatrix} d' \\ s' \\ b' \end{pmatrix} = V_{CKM} \begin{pmatrix} d \\ s \\ b \end{pmatrix} = \begin{pmatrix} V_{ud} & V_{us} & V_{ub} \\ V_{cd} & V_{cs} & V_{cb} \\ V_{td} & V_{ts} & V_{tb} \end{pmatrix} \begin{pmatrix} d \\ s \\ b \end{pmatrix} \tag{2.15}$$

The CKM matrix is a 3×3 unitary matrix. The nine complex elements yield eighteen free parameters, nine of which are unitarity constraints; six orthogonality and three normalisation. Of the nine remaining free parameters five are arbitrary phases associated with the six quark fields, and so can be discarded. Thus leaving four independent parameters which describe the CKM matrix; three Euler angles associated with the rotation in 3-dimensional space and one complex phase, δ. This phase enters the CKM matrix in the form:

$$e^{i(\omega t+\delta)}$$

This is not invariant under T violation and equivalently under CP violation. Therefore, it is through this complex phase that CP violation is introduced into the Standard Model.

2.5 Wolfenstein Parameterisation

The Wolfenstein parameterisation [18] of the CKM matrix is based on the hierarchy of the strengths of quark transitions via charged current interactions. It takes into account that the elements of the matrix can differ from each other in orders of magnitude by expanding each element as a power series in terms of λ, where

$$\lambda \equiv \sin\theta_C \simeq |V_{us}| \sim 0.22$$

and θ_C is the Cabibbo angle. The hierarchy of the strengths of quark transitions is illustrated in Figure 2.1, as indicated in the key the lines represent the orders of λ.

The Wolfenstein representation of the CKM matrix is given in Equation 2.16. In addition to the real parameter, λ, it has three other parameters; A and η and ρ that are denoted in the complex form: $(\rho + i\eta)$.

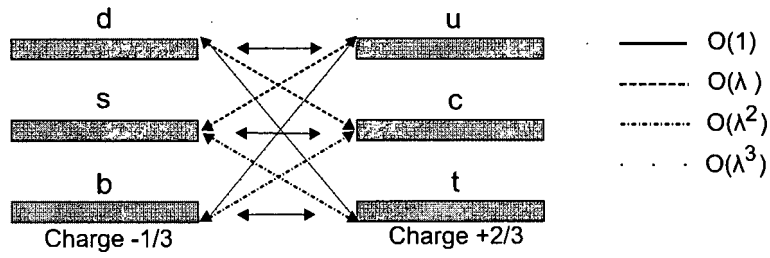

Figure 2.1: A schematic diagram illustrating the strength of the quark transitions expressed in orders of λ.

$$V_{CKM} = \begin{pmatrix} 1-\frac{\lambda^2}{2} & \lambda & A\lambda^3(\rho - i\eta) \\ -\lambda & 1-\lambda^2 & A\lambda^2 \\ A\lambda^3(1-\rho-\eta) & -A\lambda^2 & 1 \end{pmatrix} + \mathcal{O}(\lambda^4) \tag{2.16}$$

2.6 The Unitarity Triangle

The unitarity of the CKM matrix, $V_{CKM}V_{CKM}^{\dagger} = V_{CKM}^{\dagger}V_{CKM} = \mathbb{1}$, yields six orthogonality relations between any two rows or any two columns of the matrix. The sum of the complex numbers in each relation is zero, and, therefore, it can be represented geometrically as a triangle in the complex plane. Of these six *unitarity triangles* four have one side that is much shorter than the other two leaving only two triangles whose sides are of comparable length (order of λ^3). The orthogonality relations that yield these two triangles are given by Equations 2.17 and 2.18 with the triangles they represent shown in Figure 2.2.

$$V_{ud}V_{ub}^* + V_{cd}V_{cb}^* + V_{td}V_{tb}^* = 0 \tag{2.17}$$

$$V_{td}V_{ud}^* + V_{ts}V_{us}^* + V_{tb}V_{ub}^* = 0 \tag{2.18}$$

The triangle illustrated in Figure 2.2(a) represents the orthogonality relation given in Equation 2.17. It is generally referred to as *the* unitarity triangle. It is drawn by adopting a phase convention such that $V_{cd}V_{cb}^*$ is real and dividing the length of each side by the modulus of this term, $|V_{cd}V_{cb}^*|$. The angles of this triangle, α, β and γ, are defined as:

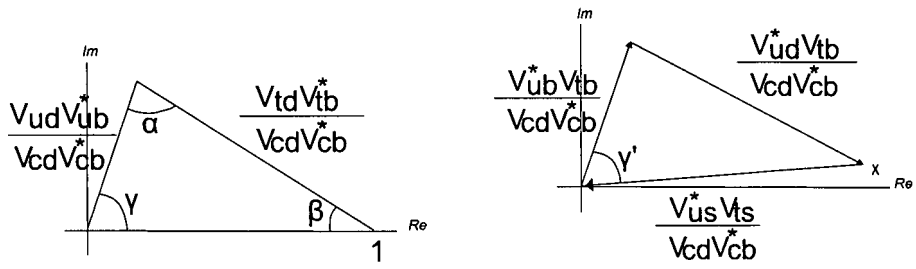

(a) (b)

Figure 2.2: An illustration of the unitarity triangles in the complex plane. (a) corresponds to Equation 2.17 and (b) represents the Equation 2.18.

$$\alpha = arg\left(-\frac{V_{td}V_{tb}^*}{V_{ud}V_{ub}^*}\right), \quad \beta = arg\left(-\frac{V_{cd}V_{cb}^*}{V_{td}V_{tb}^*}\right), \quad \gamma = arg\left(-\frac{V_{ud}V_{ub}^*}{V_{cd}V_{cb}^*}\right)$$

The angles are related by:

$$\alpha + \beta + \gamma = \pi$$

The second triangle shown in Figure 2.2(b) is of relevance to LHCb because its parameters can be measured by examining the B_s system. The angles of this triangle, β' and γ' are defined as:

$$\beta' = arg\left(-\frac{V_{ts}V_{us}^*}{V_{td}V_{ud}^*}\right), \quad \gamma' = arg\left(-\frac{V_{tb}V_{ub}^*}{V_{ts}V_{us}^*}\right) \tag{2.19}$$

and are related to β and γ by:

$$\beta' = \beta + \chi, \quad \gamma' = \gamma - \chi \tag{2.20}$$

The angle χ is defined as:

$$\chi = arg\left(\frac{-V_{cb}V_{cs}^*}{V_{tb}V_{ts}^*}\right) \equiv -\frac{1}{2}\phi_s \tag{2.21}$$

where ϕ_s is the phase of the B_s oscillations and can be determined from the $B_s \to J/\psi(\mu^+\mu^-)$ $\phi(K^+K^-)$ decay.

2.7 Theory in the context of the LHC

LHCb will test the Standard Model understanding of CP violation by measuring the decay of B mesons to various final states and extracting the values for the elements of the CKM matrix.

Both QCD and the Electro-Weak theory are important in understanding and describing the physics at the LHC. The relevance of QCD arises from the strong interactions between protons, which result in $b\bar{b}$ pair production. QCD describes the momentum of the *partons* (quarks and gluons) produced from the proton-proton collisions using *parton density functions* [19]. These describe the probability of a parton carrying a certain fraction of the momentum of the proton.

The mechanisms for the production of $b\bar{b}$ pairs at the LHC are illustrated in Figure 2.3. The primary production mechanism is gluon-gluon fusion, where the colliding protons create two gluons, which interact and create a $b\bar{b}$ pair. Quark-antiquark annihilation and flavour excitation can also produce $b\bar{b}$ pairs. The b quarks will then hadronise, forming mesons and baryons.

The decay of the particles containing the b quarks is described by the Electro-Weak theory. A Feynman diagram illustrating the decay of the B_s meson into a J/ψ and ϕ is shown in Figure 2.4.

2.7.1 The B_s mass measurement

The B_s meson is composed of a heavy b and a light s quark-antiquark pair. In the B_s meson system the flavour eigenstates and mass eigenstates are different, resulting in particle-antiparticle oscillations. This is known as B_s *mixing* [20]. It occurs due to second order weak interactions and has a dependence on the CKM matrix. The hierarchy of the elements of the CKM matrix means that only the top quark has a significant contribution to the mixing. B_s mixing gives rise to two eigenstates; heavy and light with a mass m_H and m_L, respectively. The heavy and light eigenstates of the B_s meson are an admixture of the two flavour states:

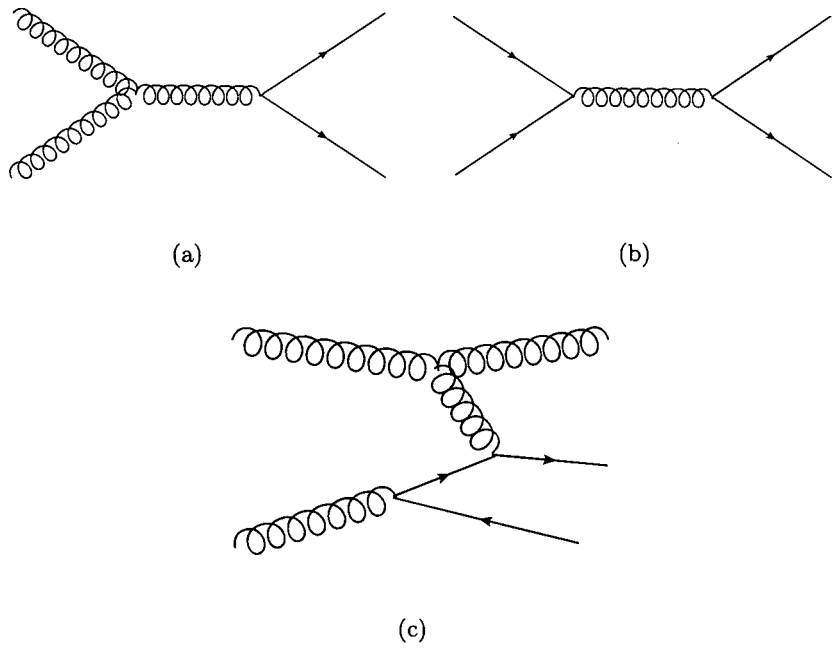

Figure 2.3: The mechanisms for $b\bar{b}$ production at the LHC. Gluon-gluon fusion is shown in (a), quark-antiquark annihilation is shown in (b) and flavour excitation in (c).

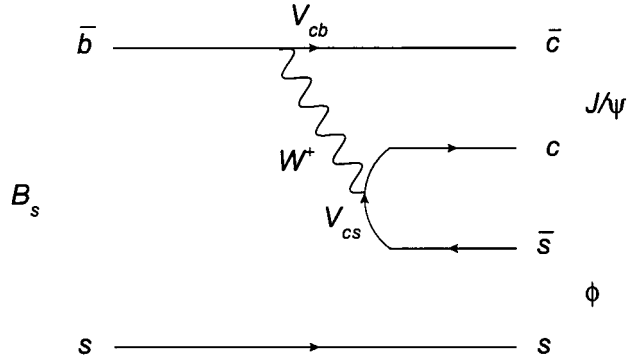

Figure 2.4: A Feynman diagram illustrating the $B_s \rightarrow J/\psi(\mu^+\mu^-)\phi(K^+K^-)$ decay.

$$|B_H\rangle = p|B\rangle + q|\bar{B}\rangle, \quad |B_L\rangle = p|B\rangle - q|\bar{B}\rangle$$

where p and q are fractions of the original states. The Standard Model postulates that the mass eigenstates of the B_s system are approximately the same as the CP eigenstates. The light mass eigenstate is said to be CP even with a larger decay width, and, therefore, a shorter lifetime than the heavy mass eigenstate.

At the LHC the $B_s \rightarrow J/\psi(\mu^+\mu^-)\phi(K^+K^-)$ decay mechanism will have a clean experimental signature and is therefore ideal for making two measurements; the average mass of the B_s meson and the mass difference between the heavy and light eigenstates, $\triangle m_s$. The content of this thesis focuses on extracting the average mass of the B_s meson.

A theoretical value for the B_s mass can be obtained from lattice QCD calculations [21]. Lattice QCD provides numerical simulations of QCD by representing the space-time continuum as a four-dimensional discrete lattice. The lattice grid has a spacing, a, with the quark fields represented by the sites (points) on the grid and the gluon fields by the links (lines) between them. Computing a path integral over the gluon fields results in a set of values for the gluon field on every link in the lattice together with the probability of how much the field will contribute to the integral. This information is used to evaluate the path integral, to which a fit is then applied to extract the mass of a hadron. The lattice QCD prediction for the B_s mass [22] is given in Figure 2.5. It can be seen that the lattice QCD predicted values are somewhat larger than the experimentally obtained average B_s mass, this arises from systematic uncertainties associated with the lattice QCD methodology.

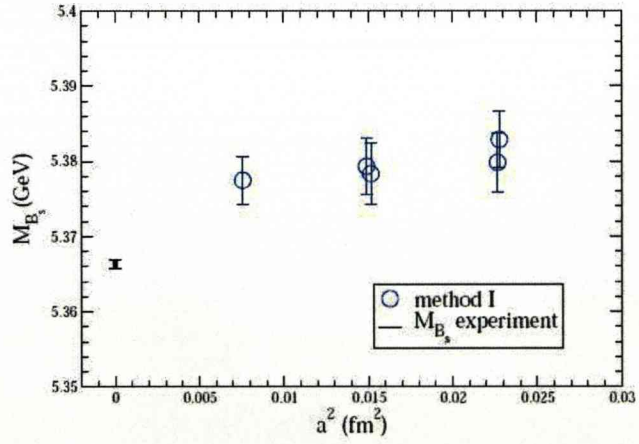

Figure 2.5: A plot showing the lattice QCD prediction for the mass of the B_s meson.

The first measurement of the B_s mass was made by the ALEPH collaboration in 1993 [23]. The B_s mass was found to be $5.3686 \pm 0.0056(\text{stat}) \pm 0.0015(\text{syst})$ GeV/c^2. To date the the average value for the B_s mass is 5.3663 ± 0.0006 GeV/c^2 [24].

Chapter 3

The LHCb Detector

This chapter discusses the Large Hadron Collider particle acceleration facility, focusing on the dedicated B physics experiment, LHCb. An overview of the acceleration facility is given in Section 3.1, followed by a discussion of the LHCb experiment and it's sub-detectors in Section 3.2. The silicon based Vertex Locator is discussed in detail because the analysis of testbeam data taken with part of this detector is presented Chapters 4 and 5. Section 3.3 provides an overview of the trigger system and Section 3.4 outlines the LHCb software framework.

3.1 The Large Hadron Collider

The Large Hadron Collider (LHC) is a particle acceleration facility at CERN, the European Organisation for Nuclear Research. The 27 km circumference ring will collide two counter rotating beams of protons at a centre of mass energy of up to $\sqrt{s}$ of 14 TeV and has a design luminosity of $10^{34}\,\mathrm{cm}^{-2}\mathrm{s}^{-1}$; becoming the world's most powerful particle accelerator and providing a means with which to search for physics beyond the Standard Model.

A complex acceleration process is required to achieve the centre of mass energy at which the LHC will run. The accelerator complex is illustrated in Figure 3.1. The protons are stripped from hydrogen gas in a duoplasmatron. They are then accelerated through a linear accelerator (LINAC), which increases their energy to 50 MeV, followed by the Proton Synchrotron Booster (PSB) that further increases their energy to 1.4 GeV. The protons are then fed through the Proton Synchrotron (PS), which will

accelerate them to 26 GeV. The final pre-LHC injection acceleration is done in the Super Proton Synchrotron (SPS), with the energy of the protons reaching 0.45 TeV. Two transfer lines will inject the protons into the LHC. The beams will travel in opposite directions, and will be accelerated up to the design beam energy of 7 TeV. The protons will maintain their orbit with the aid of a 8.3 T magnetic field in the bends provided by superconducting magnets operating at a cryogenic temperature of 1.9 K.

Each beam will contain 3564 bunches, 2808 of which are filled, each containing 10^{11} protons. The bunches will cross at a frequency of 40 MHz, which corresponds to a bunch crossing every 25 ns.

The beams will be brought together and collided at four interaction points, which each house an experiment. Figure 3.1 shows a diagram of the CERN accelerator complex indicating the positions of the four experiments on the LHC ring. There are two general purpose detectors, with 4π coverage; A Toroidal LHC AparatuS (ATLAS)[25] and the Compact Muon Solenoid (CMS)[26]. The aim of these experiments is to search for the Higgs boson, supersymmetric particles and other phenomena that are not described in the Standard Model. The heavy ion detector, A Large Ion Collider Experiment (ALICE)[27], will investigate the existence of QCD bulk matter and the quark-gluon plasma. The Large Hadron Collider beauty experiment (LHCb)[28] is a dedicated B physics experiment, the details of which will be discussed in the next section.

3.2 The LHCb detector

The LHCb experiment will exploit the copious amounts of B mesons produced at the LHC to study Charge Parity (CP) violation and the rare decays of B mesons. The experiment will extend the B physics results obtained by the B Factories [29] and the Tevatron [30], further constraining the elements of the unitarity triangle, and through the study of rare decays search for new physics.

The LHC will produce 10^{12} $b\bar{b}$ pairs per nominal year of data taking (10^7 s). Both of the B mesons originating from the same $b\bar{b}$ pair are produced in the same forward or backward cone and at low polar angles. A PYTHIA [31] simulation of the polar angle

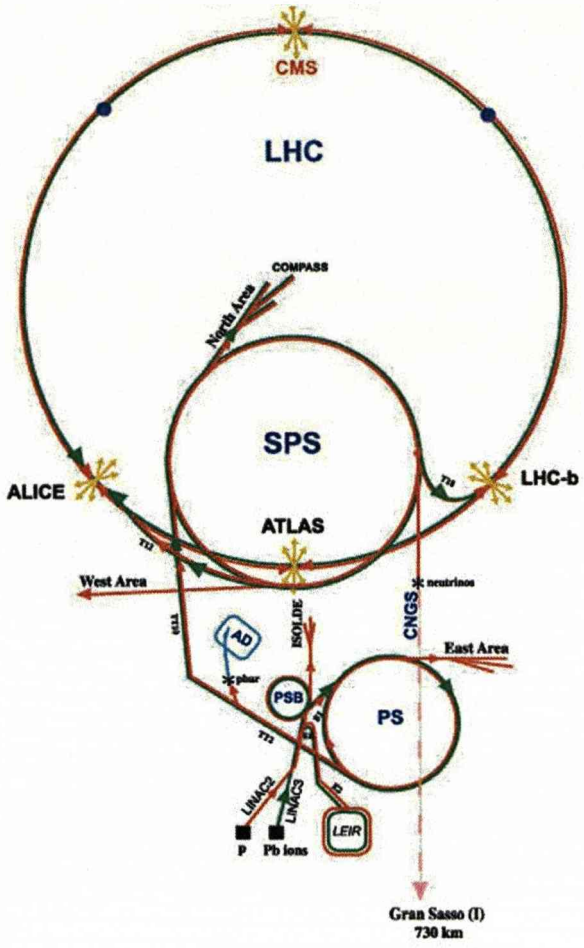

Figure 3.1: A schematic diagram illustrating the CERN accelerator complex, along with the positions of the four LHC experiments.

distribution of $b\bar{b}$ pairs produced from colliding protons at a centre of mass energy of 14 TeV is shown in Figure 3.2.

The LHCb detector is a single arm spectrometer covering the forward region, with an acceptance of 10-250 mrad in the horizontal (non-bending) plane and 10-300 mrad in the vertical (bending) plane, corresponding to a pseudorapidity range of $1.6(2.1)<\eta<4.9$, where the definition of pseudorapidity, η, is given in Equation 3.1. Approximately one third of the $b\bar{b}$ pairs produced at the LHC will lie within this acceptance.

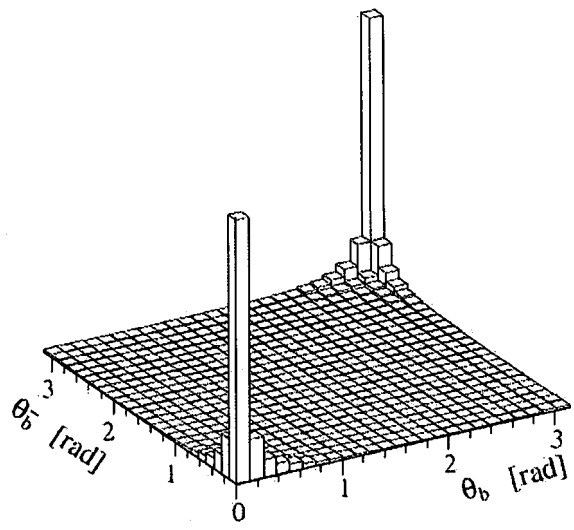

Figure 3.2: The polar angle distribution of the $b\bar{b}$ pairs produced at a centre of mass energy of 14 TeV as generated by PYTHIA.

$$\eta = -\ln\left[\tan\left(\frac{\theta}{2}\right)\right] \tag{3.1}$$

The LHCb experiment employs a right handed co-ordinate system, with the origin at the interaction point, the z axis along the beam line and the y axis in the vertical direction.

The luminosity, $\mathcal{L}$, is a measure of the performance of a collider experiment, quantifying the number of particles per second for a cross-section of $1\,\mathrm{cm}^2$. The probability of obtaining n proton-proton interactions in a given bunch crossing is described by the Poisson distribution as shown in Equation 3.2, where μ is the average number of collisions per bunch crossing. It is related to the luminosity, $\mathcal{L}$, and the inelastic $b\bar{b}$ cross-section, $\sigma_{inelastic}$, by Equation 3.3. At the LHC $\sigma_{inelastic}$ is 80 mb, the bunch crossing frequency, f_{LHC}, is 40 MHz, and the fraction of non-empty bunch crossings, ϵ_{filled}, is 0.744.

$$P(\mu, n) = \frac{\mu^n}{n!} \cdot e^{-\mu} \tag{3.2}$$

$$\mu = \frac{\sigma_{inelastic} \cdot \mathcal{L}}{f_{LHC} \cdot \epsilon_{filled}} \tag{3.3}$$

The average number of proton-proton interactions per bunch crossing at the LHC design luminosity is 27. Such conditions would make the fast identification and real time measurement of b quarks that is required by LHCb virtually impossible. The most desirable conditions in which to reconstruct b quarks is when there is a single proton-proton interaction in each bunch crossing. The probability of n proton-proton interactions in a single bunch crossing at the LHC as a function of the instantaneous luminosity is shown in Figure 3.3. Examining the figure it can be seen that the probability of one interaction per bunch crossing is at its greatest, 0.35, at a luminosity of $4\times10^{32}\,\mathrm{cm}^{-2}\mathrm{s}^{-1}$. At this luminosity the probability of multiple proton-proton interactions per bunch crossing is relatively high. Thus, LHCb will operate at a luminosity of $2\times10^{32}\,\mathrm{cm}^{-2}\mathrm{s}^{-1}$, a factor of one hundred lower than the design luminosity of the LHC. This reduction is achieved by defocusing the beams before they collide at the LHCb interaction point (IP8).

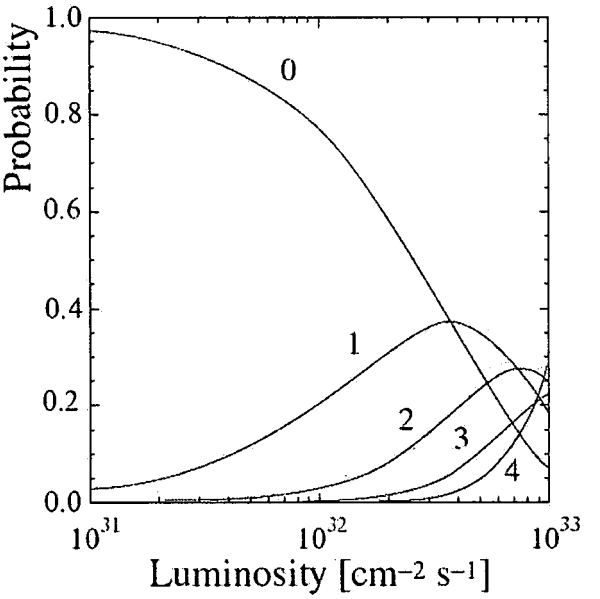

Figure 3.3: The probability distribution of the number of inelastic proton-proton interactions per bunch crossing as a function of the instantaneous luminosity.

A schematic diagram of the LHCb detector is given in Figure 3.4. It is composed of

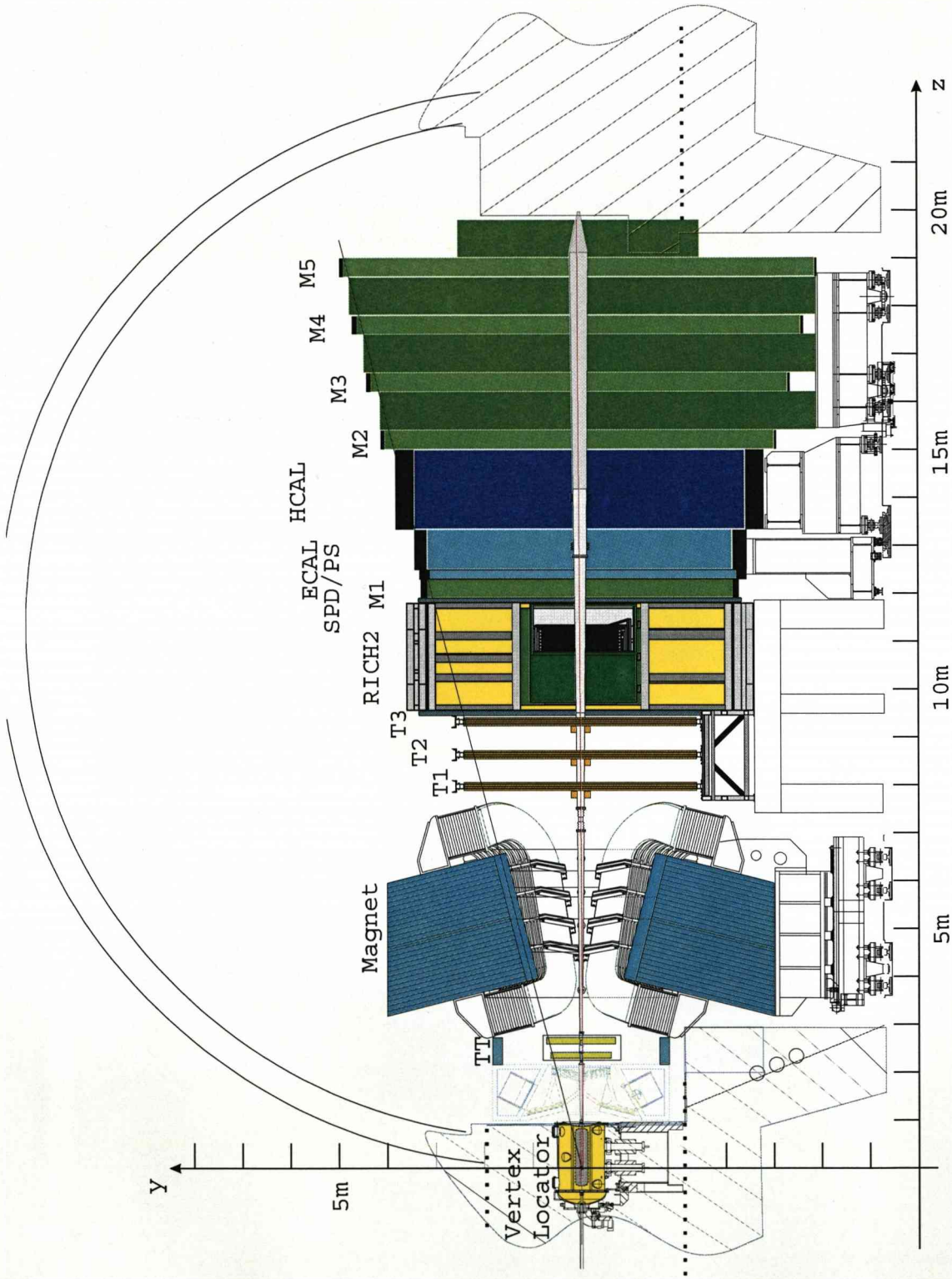

Figure 3.4: A schematic diagram of the LHCb detector showing the sub-detector elements; the Vertex Locator, Ring Imaging Cherenkov detectors, tracking detectors, the magnet, and the calorimetry and muon systems.

6 sub-detectors; the Vertex Locator, Ring Imaging Cherenkov detectors, the magnet, tracking detectors, calorimetry and the muon system. A description of each will be given in subsequent sections. A discussion of the Vertex Locator will be given in some detail because the analysis of data taken with part of this sub-detector is presented in Chapters 4 and 5.

3.2.1 Vertex Locator

The Vertex Locator (VeLo) [32][33] is the primary tracking detector of the LHCb experiment. It encompasses the interaction region, providing a measurement of the primary and secondary vertices. The primary vertex is the position at which the initial proton-proton interaction occurred, the secondary vertex is displaced a few millimetres downstream from this point and is where the decay products are produced. The VeLo has a primary vertex resolution of 45 μm along the beam direction (z) and 10 μm in the transverse plane (x and y) [34]. The secondary vertex can be determined with a resolution of 100 μm in z and 10 μm in the x and y directions [35].

The VeLo, illustrated in Figure 3.5, consists of two halves, each containing 21 double sided silicon modules that are positioned perpendicular to the beam axis (z) and cover a distance of 1 metre along it. The first stations of the VeLo are situated in the backwards hemisphere at z=-17.5 cm and they extend to z=+75 cm, with zero defined as the nominal interaction point. Each VeLo half also houses two single sided modules carrying radial measuring sensors, known as Pile-Up modules. The Pile-Up modules are positioned at the furthermost station in the backwards hemisphere and form the Pile-Up VETO system, which is used in the Level Zero trigger (see Section 3.3).

The distance of closest approach of a reconstructed track to a primary vertex is known as the impact parameter (IP). To obtain an optimal impact parameter resolution a short track extrapolation distance is required, therefore the distance between the VeLo modules and the beams must be as small as possible. The active areas of the modules, the silicon sensors, are placed at a radial distance of 8 mm from the beam. This imposes several constraints on the VeLo. To protect the VeLo from instabilities of the beam during injection it must be retractable. The aperture required by the LHC machine dictates that each VeLo half must be retracted by 3 cm during beam injection.

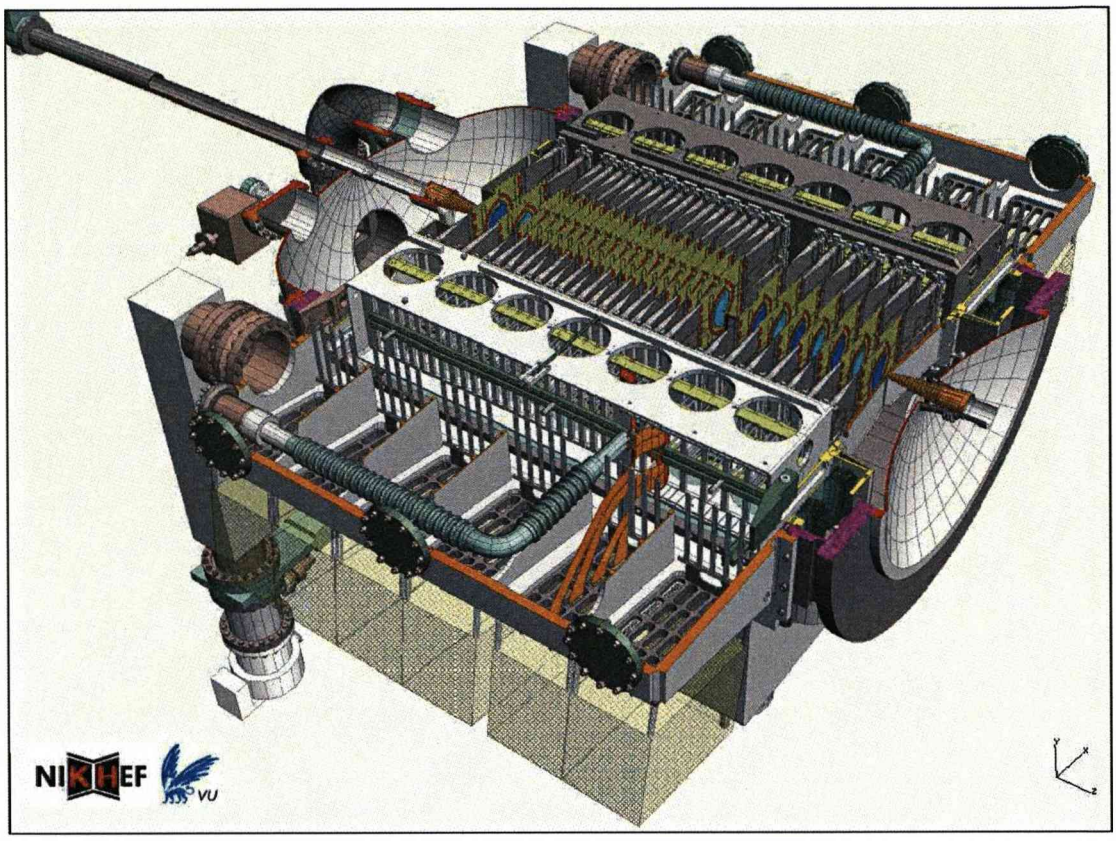

Figure 3.5: An illustration showing a cross section of the LHCb VeLo tank with the detector in closed position. The RF boxes, which house the detector halves are not shown, allowing the overlap between the halves to be seen.

Each VeLo half is mounted in a vessel known as a RF box, constructed from 250 μm thick aluminium. The RF boxes are positioned in a secondary vacuum within the primary vacuum of the LHC beams, which have a pressure of below 10^{-4} mbar and 10^{-8} mbar, respectively. On the top side of each box is the corrugated RF foil, as shown in Figure 3.6. The RF foil provides a separation between the VeLo system and the proton beams, shielding the VeLo from RF pick ups of the beams and protecting the beams from any components of the module material that out gas when the module is placed under vacuum, thus eliminating the possibility of beam-gas interactions as a background to the beam-beam interactions. It also enables an overlap of 2.6 mm between the sensors when the VeLo is in closed position and minimises the material through which the charged particles traverse.

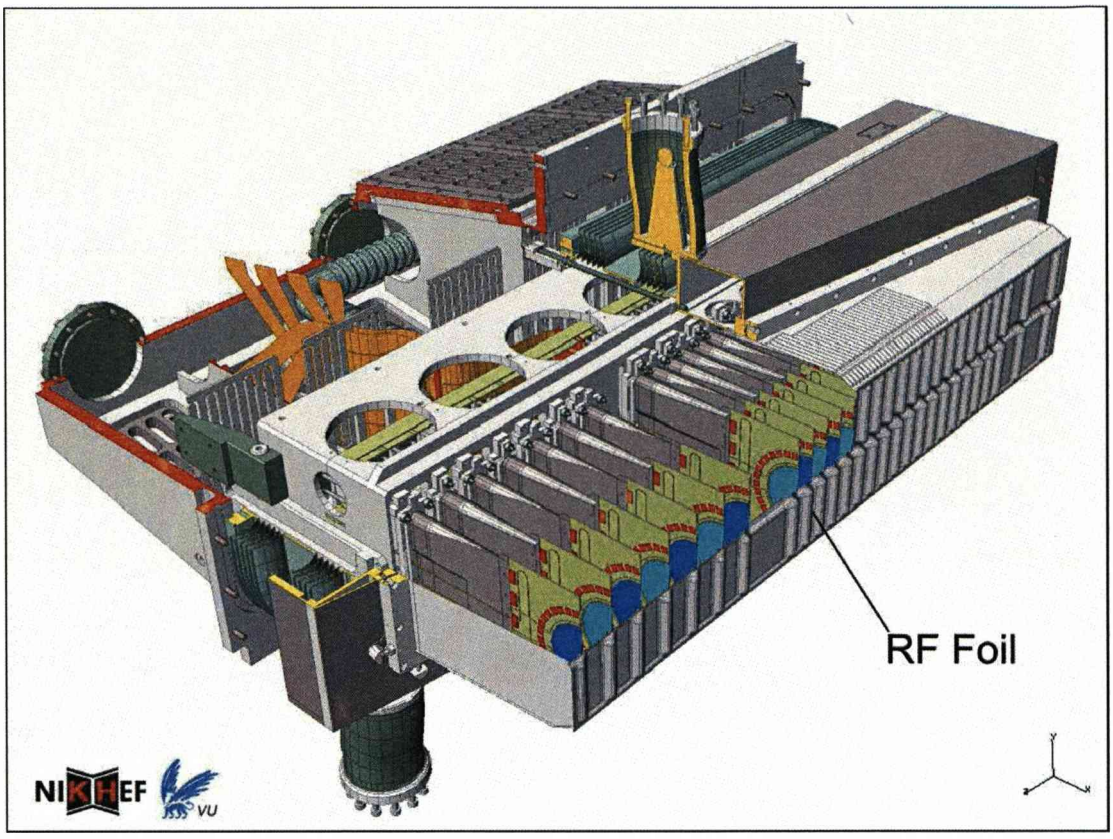

Figure 3.6: An illustration of a VeLo half, showing the corrugated RF foil on the top side of the RF box.

Silicon sensors

The principle of operation of the silicon sensors is the p-n junction, which occurs at the interface between two doped semi-conductor materials. The semi-conductor is doped by replacing some of the atoms in the silicon lattice with impurity atoms. It can be either n-doped or p-doped depending on the group of the Periodic Table that the impurity element belongs to. N-type silicon is implanted with an element from Group V, which has five electrons in the valence band. The impurity atom donates an electron to the conduction band of a silicon atom, resulting in a silicon lattice with free electrons. The n-type silicon used for the VeLo sensors has phosphorus donor atoms. P-type silicon is implanted with an element from Group III, which has three free electrons in the valence band. These are known as acceptor atoms. The impurity atom accepts an electron from the valence band of a silicon atom, creating positively charged holes. The p-type silicon used for the VeLo sensors has boron acceptor atoms. When the n-doped and p-doped silicon meet the free electrons and holes drift across the junction between

the two materials and re-combine, leaving a region around the junction that is free of charge carriers - the *depletion* region. The width of the depletion region is very narrow, it can be increased by applying a reverse bias voltage. The VeLo sensors operate fully depleted to yield good charge collection efficiencies. The sensors fall into three categories; those that reach full depletion at approximately 30 V, 50 V and 60 V [36]. In the experiment all sensors will initially operate above full depletion at 100 V.

The proximity of the sensors to the beams mean that they operate in a harsh non-uniform radiation environment, with an expected annual fluence ranging from 1.3×10^{14} neutron equivalents/cm^2 at the innermost radius to 5×10^{12} neutron equivalents/cm^2 at the outermost radius. Therefore, the sensors have to be extremely radiation hard.

The VeLo has 41 modules carrying n in n silicon sensor and one module carrying n in p sensors.

The two silicon microstrip sensors are 300 μm thick, semi-circular in shape and each have a coverage of 182°. The sensors have a double metal layer, which routes the signals between the strips and the bonding pads on the outer radii of the sensors. Both R and ϕ sensors have an active inner radius of 8.17 mm extending to an outer radius of 42.2 mm, containing 2048 readout channels.

An R sensor has channels of circular arc shape arranged in 45° quadrants, with 512 channels in each. The strip pitch increases as a function of the radius, ranging from 40 μm at the innermost radius to 101.6 μm at the outermost radius.

A ϕ sensor has radial channels. The sensor is divided into an inner and outer region, which contain 683 and 1365 channels, respectively, with an overlapping pitch region. The inner strip region ranges from 35.5 μm to 78.3 μm, whilst the outer strip pitch starts at a radius of 17.25 mm with a strip pitch of 39.3 μm, increasing to 96.6 μm at the outermost radius. The strips in each region slope in opposite directions; the strips in the inner region are inclined at an angle of 20° and those in the outer region are at an angle of -10° to the radial, forming a 'dog-leg' design.

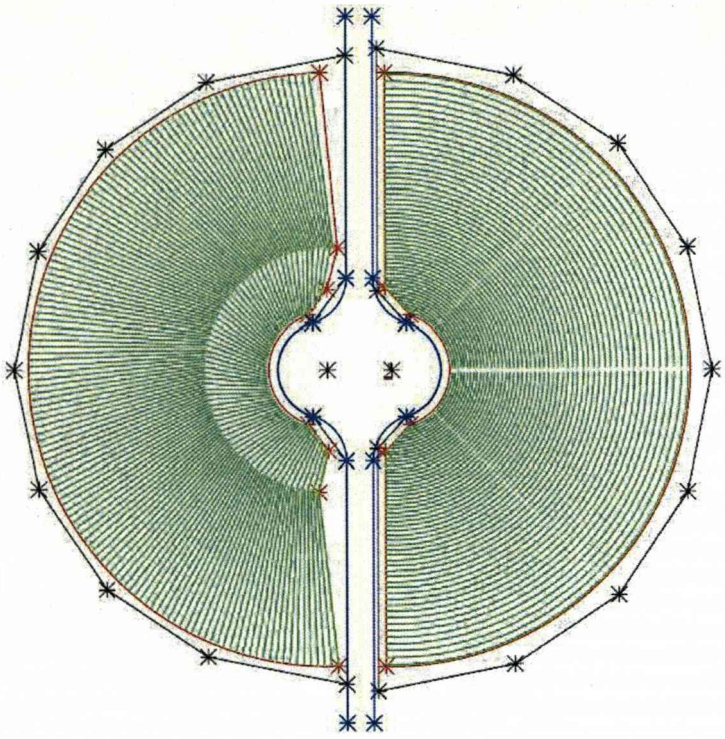

Figure 3.7: A schematic diagram of the VeLo sensors; the ϕ sensor on the left and the R sensor on the right. For clarity only every tenth strip is shown.

VeLo module

The VeLo modules are double sided silicon microstrip detectors, with a 'R' measuring sensor on one side and a 'ϕ' measuring sensor on the other. The R sensor provides a radial measurement from the beam axis, while the ϕ sensor provides a measurement of the azimuthal angle around the beam. When positioned in the experiment alternate VeLo modules are flipped, such that sensors of the same type are adjacent to each other.

A VeLo module, shown in Figure 3.8, consists of a 1.5 mm substrate made from 400 μm thick thermal pyrolytic graphite (TPG) encased in carbon fibre (CF) of thickness 250 μm, on to which two electrical circuits are laminated, forming the hybrid. The sensors are glued back-to-back on to the hybrid [37] with an accuracy of 10 μm [38]. A semi-circular hole smaller than the radius of the sensors is cut out of the top of the hybrid such that there is no material between the sensors at their inner radii. Sixteen *Beetle* front-end readout chips [39] and four kapton pitch adapters are glued beyond the outer radius of each sensor [40], with a total of 32 Beetle chips and 8 pitch adapters re-

quired for each module. The Beetle chips read out the analogue signal from the readout channels, which are arranged in two rows on the outer radius of the sensor. The pitch adapters are required to change the pitch of the spacing between the bonding pads on the sensor to match those of the readout chips making the connections between the module components possible. Connections are made between the module components via wire bonding using a 25 μm thick aluminium alloy wire, containing 99% aluminium and 1% silicon. Three wire bonding steps are required; back end bonding [41] during which all the wire connections betweens the Beetle chips and the hybrid are made, front end bonding [42], which connects the 128 readout channels per Beetle chip to the pitch adapters, and finally the sensor end bonding, connecting the sensors to the hybrid by placing wire bonds between the pitch adapters and the sensors. The populated hybrid is glued to a pedestal; a low mass CF paddle and base with Invar feet[44]. The pedestal can be glued to either the side carrying the R sensor or the side carrying the ϕ sensor; the modules are mounted alternately R-glued and ϕ-glued.

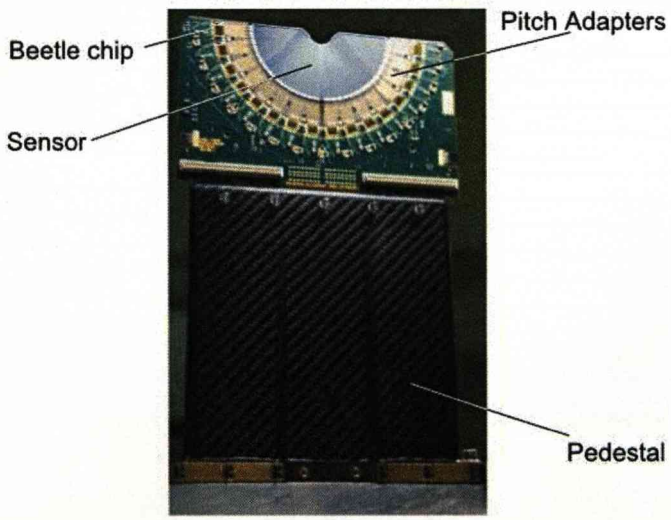

Figure 3.8: A photograph of a VeLo module.

During operation each VeLo module will dissipate 24 W of heat, which has to be removed from the secondary vacuum before it affects the operation of the electronics and silicon sensors. An increase in temperature increases the radiation damage of the

sensors. To limit the effect of radiation damage on the sensors they must be kept at a temperature of below -5°C. This is maintained using a two-phase carbon dioxide (CO_2) cooling system. The CO_2 is served to the VeLo modules via a 60 m transfer line, which delivers the CO_2 to the five cooling blocks that are attached to each module.

Electronics chain

The silicon sensors are read out by radiation hard Beetle chips, custom designed for the LHCb experiment and fabricated using 0.25 μm CMOS process. The Beetle chip integrates 128 channels, each containing a low noise charge sensitive pre-amplifier, a CR-RC pulse shaper and a buffer. This forms the analogue front-end of the chip. The output of each front-end is sampled, in parallel, at 40 MHz into the analogue pipeline memory, which is implemented as a switched capacitor array with a latency of 4 μm. The 128 channels are multiplexed and transmitted off the chip by four current output drivers in 900 ns.

The data signal is transmitted via two kapton cables; a short cable connecting the hybrid to a fixed connector and a long cable from the connector to the vacuum feed through on the vessel, to the repeater boards [46] housed immediately outside of the VeLo tank. The repeater boards each contain six cards; one Low Voltage (LV) card, one Experiment Control System (ECS) card and four driver cards. The LV and ECS cards provide and monitor the low voltage supply to the hybrids. The driver cards boost the analogue signal and compensate for any distortions that may occur when the data is transmitted via a 60 m shielded twisted-pair cable to the digitiser board, known as the TELL1 board [47]. One repeater board and one TELL1 board are required per sensor. In addition to providing an interface to the ECS via a credit card PC the TELL1 board contains four A-Rx cards that digitise the data. Each A-Rx card has 16 channels of 10-bit Analogue to Digital Converters (ADCs) that sample the analogue data from four Beetle chips at a rate of 40 MHz. The sampling time for each individual ADC channel can be tuned using phase adjustable programmable clocks to compensate for a skew in the arrival time of the signal that may occur as a result of differences in the lengths of the cables. Each TELL1 board has four Field Programmable Gate Arrays (FPGAs), to which the data is sent after digitisation. The FPGAs apply an Finite Impulse Response (FIR) filter to remove any crosstalk, perform digital filtering,

pedestal and common mode noise subtraction, and clustering.

Performance

Performance was an important issue during the VeLo module construction with only those modules carrying sensors which had 99 % of their strips operational accepted. A subset of the final production VeLo modules have been assessed in a testbeam environment under the same conditions that will be imposed during LHC operation (see Chapter 4). The signal to noise ratio was found to vary between 22 and 24 for the R sensors and 23 and 28 for the ϕ sensors (see Chapter [?]). The hit resolution for the sensors quoted as a function of the strip pitch has been measured as 8.5+0.26×(pitch-40) μm [48].

3.2.2 Ring Imaging Cherenkov detectors

Particle identification is provided by the Ring Imaging Cherenkov detectors (RICH) [49]. Two RICH detectors are required because as the polar angle increases the momenta spectrum becomes softer, meaning that a single radiator medium can not be used. RICH1 detects low momentum charged particles in the range 1-60 GeV/c, whereas RICH2 detects charged particles with high momentum, approximately 15-100 GeV/c.

Both RICH detectors work by the same principle. Photons are emitted, in a cone of Cherenkov radiation, when a charged particle traverses the dielectric medium with a velocity greater than the velocity of light in that medium. The angle at which the Cherenkov light is emitted, θ_c, is related to the velocity of the particle, v, by Equation 3.4, where n is the refractive index of the medium and c is the velocity of light.

$$\cos\theta_c = \frac{c}{n \cdot v} \tag{3.4}$$

A combination of spherical and plane mirrors focus and reflect the image of the photons outside the LHCb acceptance and on to the photon detector planes, where the light is collected by Hybrid Photon Detectors (HPDs). Each HPD is sensitive to single photons in the wavelength range 200-600 nm.

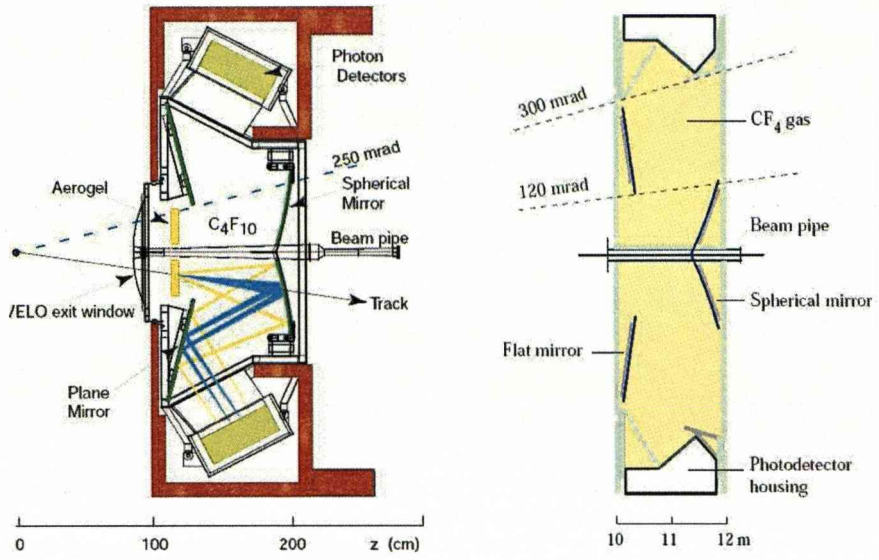

(a) RICH1 (b) RICH2

Figure 3.9: Schematic diagrams of the RICH detectors.

RICH1

RICH1, illustrated in Figure 3.9(a), is the most upstream of the two RICH detectors. It is located between the VeLo and the Turicensis Tracker, and covers the full LHCb acceptance. It employs a combination of two radiators; a 5 cm thick wall of solid silicon aerogel (n=1.03) followed by gaseous C_4F_{10} (n=1.0014) contained within a gas tight enclosure. The optical system of RICH1 has a vertical symmetry, with the sets of mirrors placed above and below the beamline.

RICH2

RICH2, shown in Figure 3.9(b) is located downstream of the magnet, between the last tracking station and the first muon station, covering an acceptance of 15-120 mrad. A radiator medium of gaseous CF_4 (n=1.0005) is used. The optical system of RICH2 has a horizontal symmetry, with the sets of mirrors positioned to the left and right of the beamline.

3.2.3 Particle identification

The RICH system provides particle identification (PID) by considering the pattern of hit pixels in the HPDs compared to the pattern that would be expected for reconstructed tracks with a given set of mass hypotheses. A likelihood is determined from this information, which is then maximised by varying the mass hypothesis.

The mass of a particle, m_0, can be deduced from Equation 3.5, where p is the measured track momentum.

$$p = \gamma \cdot m_0 \cdot c \tag{3.5}$$

The relativistic γ is given by Equation 3.6, where $\beta = \frac{v}{c}$.

$$\gamma = \sqrt{\frac{1}{1-\beta^2}} \tag{3.6}$$

3.2.4 Magnet

A warm dipole magnet [50] covering the full LHCb acceptance enables the momenta of charged particles to be determined from the curvature of their tracks. An integrated magnetic field of 4 Tm for tracks originating close to the primary interaction point yields a desired momentum resolution of 0.4% for particles with momenta up to 200 GeV/c. The magnet consists of two identical saddle shaped aluminium coils positioned mirror symmetrically in an iron yoke, as illustrated in Figure 3.10. The design of the magnet is dictated by the need for an extremely high magnetic field between the Turicensis Tracker and tracking stations and a magnetic field of less than 2 Tm near the RICH. The variation in the strength of the magnetic field across the tracking system is shown in Figure 3.11.

3.2.5 Tracking system

Along with the VeLo, the Turicensis Tracker [33] and the three tracking stations, T1-T3, form the tracking system of the LHCb detector. The tracking system provides efficient reconstruction of charged particle tracks and precise measurements of their momenta.

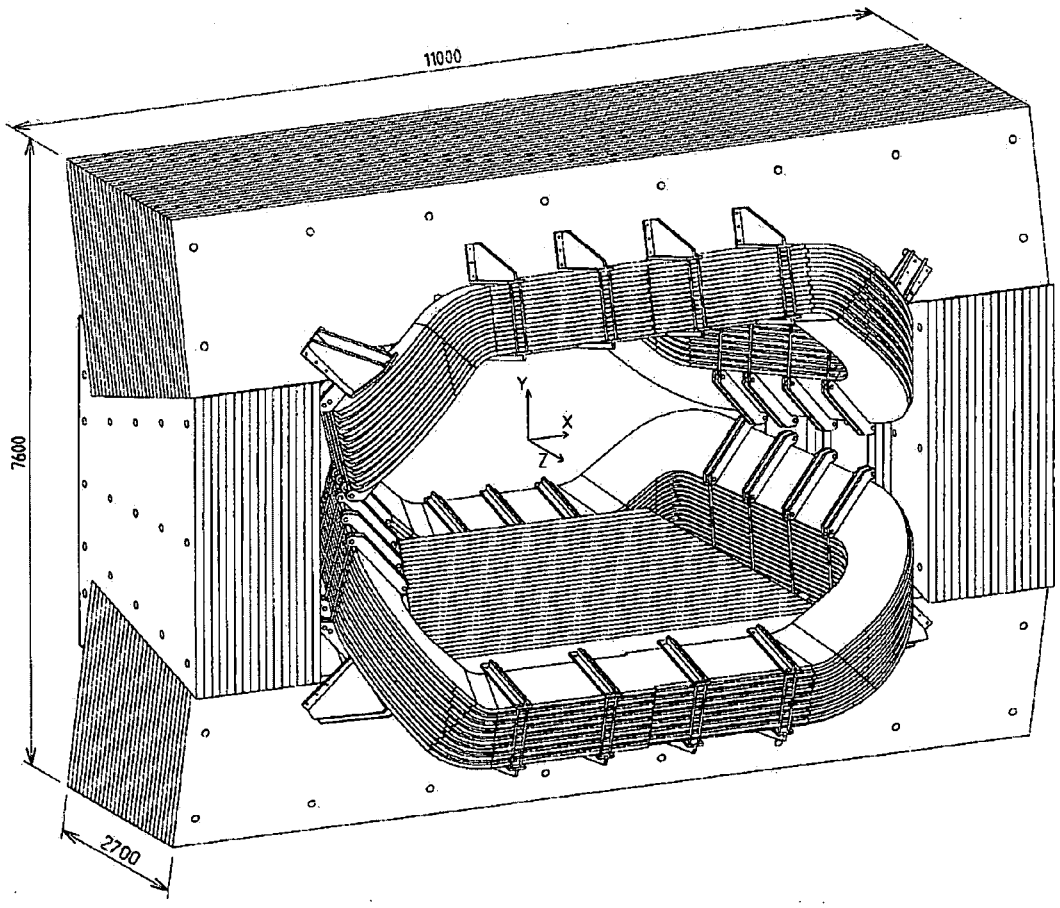

Figure 3.10: A schematic diagram of the LHCb magnet

Turicensis Tracker

The Turicensis Tracker (TT) is a silicon microstrip detector. It is located in front of the magnet and covers the full LHCb acceptance. The TT is an essential component in the study of long lived neutral particles that decay outside of the volume of the VeLo and low momentum particles that are deflected outside of the detector acceptance by the magnet before reaching the downstream tracking stations.

The TT consists of four planes of silicon arranged into two stations. The first and final planes of silicon have vertical readout strips (x layers), the second plane of silicon has readout strips rotated by a stereo angle of +5° (u layer), whereas the third plane of silicon has readout strips that are rotated by a stereo angle of -5° (v layer). This 'xuvx' geometry provides accurate measurements of track co-ordinates. The silicon has a strip pitch of 200 μm giving a single hit resolution of 50 μm.

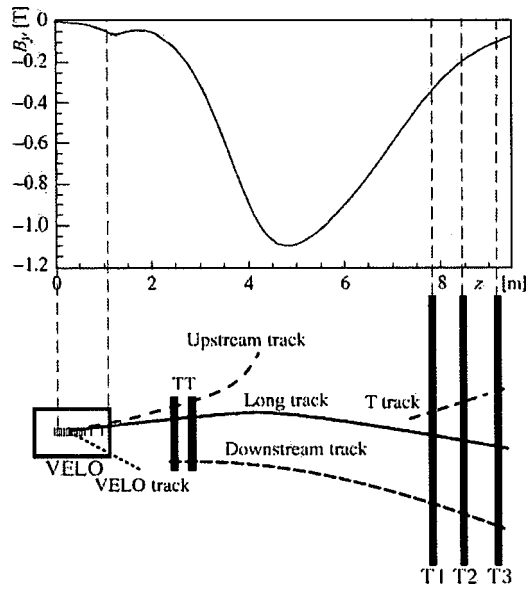

Figure 3.11: A plot illustrating the variation in the magnetic field strength between the VeLo and T1-T3 tracking stations.

Tracking stations

The three tracking stations are located immediately after the magnet. The particle fluxes are high close to the beamline but fall rapidly with increasing distance. Therefore, each station is divided into two; the inner tracker (IT) [51] and the outer tracker (OT) [52], each employing a different detector technology. Together, the IT and the OT cover the full LHCb detector acceptance.

The IT is a small silicon microstrip detector closest to the beamline. It is constructed of four individual detectors placed above, below, and each side of the beampipe, each with four planes of silicon, providing a 'xuvx' orientation

The OT surrounds the IT, it is a drift chamber detector, using straw tube technology. Each station comprises of four layers of modules with two layers of staggered drift tubes in each module, again providing a 'xuvx' geometry. The straw tubes have radius of 5 mm, and are filled with a gas mixture of argon(70%) and carbon dioxide (30%), resulting in a maximum drift time of 25 ns.

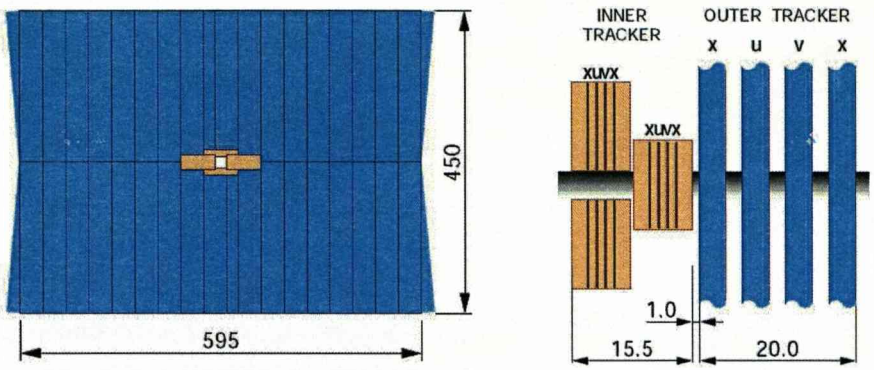

(a) The front view of a tracking station. The IT is seen in the centre, surrounded by the OT

(b) The top view of a tracking station

Figure 3.12: Schematic diagrams illustrating the front and top views of a tracking station.

3.2.6 Track reconstruction

The trajectories of particles traversing the LHCb detector are reconstructed by combining hits registered in the tracking detectors; the VeLo, TT and T stations. There are five types of tracks; VeLo tracks, T tracks, Long tracks, Upstream tracks and Downstream tracks.

- **VeLo tracks** are tracks that only traverse the VeLo. They are created by particles that are produced at large angles or those which are produced in the backwards hemisphere, of which, the VeLo has a limited coverage. VeLo tracks are useful in the reconstruction of primary vertices. Tracks seen in the VeLo can only be reconstructed if the particle gives at least three hits in both R and ϕ sensors;

- **T tracks** are seen in the T stations, only. The particles that leave these tracks are produced from secondary interactions. For a T track to be reconstructible the particle must leave a minimum of one x and one stereo hit in each of the three T stations;

- **Upstream tracks** traverse the VeLo and TT detectors, only. These are generally low momenta tracks created by particles that do not fully traverse the magnet, but instead are deflected outside of the detector acceptance;

- **Downstream tracks** traverse the TT and T stations, only. They are generally created by long lived particles, for example K^0_S, which decay outside of the VeLo tank;

- **Long tracks** traverse all the tracking detectors. The momemta of these tracks can be precisely determined because they have momentum and vertex information associated with them, meaning that they are very important in the reconstruction of B meson decays.

Long tracks are used exclusively in physics analysis studies because they have excellent momentum resolution and a short extrapolation distance to the production vertex. The reconstruction efficiency of these tracks is also high. The reconstruction efficiency of the $B_s \rightarrow J/\psi(\mu^+\mu^-)\phi(K^+K^-)$ decay discussed in Chapter 5 is 82.5% [33].

The relative momentum and impact parameter resolutions of reconstructed long tracks are shown in Figure 3.13. The relative momentum resolution as a function of the track momentum is given in Figure 3.13(a). The momentum resolution, δp, is defined as the RMS of the difference between the reconstructed and true track momentum. Figure 3.13(b) shows the impact parameter resolution in millimetres as a function of the inverse of the transverse momentum.

3.2.7 Calorimeters

The calorimeter system [53] is located downstream of the RICH2 detector. It provides a measurement of the energy and hit positions of electrons, hadrons and photons by their complete absorption into the material, which results in particle showering. The calorimetry system has four components; Scintillator Pad Detector, Pre-Shower, Electromagnetic calorimeter and the Hadronic calorimeter.

Scintillator Pad Detector

The Scintillator Pad detector (SPD), comprising of a 15 mm thick scintillator plane, forms the first layer of the LHCb calorimetry system. The SPD differentiates between charged and neutral particles, thus distinguishing electrons from neutral pions, π^0. Electrons will deposit energy in the scintillating material as they traverse it, whereas, the decay products of the π^0, photons, will have little interaction.

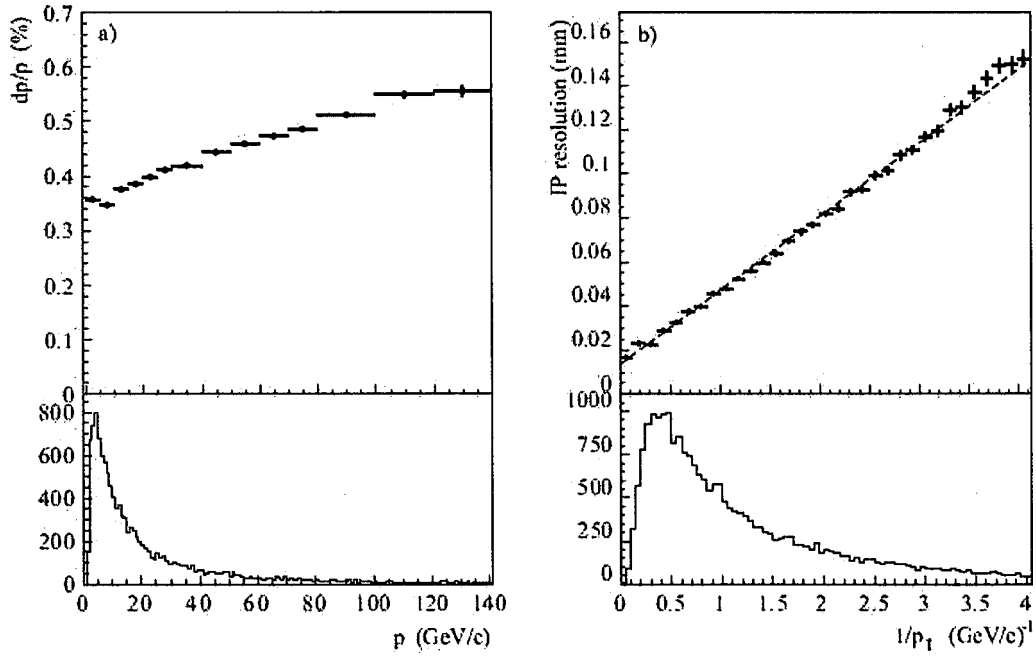

Figure 3.13: The relative momentum (left)and impact parameter (right) resolutions of reconstructed long tracks.

Pre-Shower

The Pre-Shower (PS) is the second component of the calorimetry system. It comprises of a 12 mm thick lead plate followed by a 15 mm thick layer of scintillating material. The PS provides electron and hadron separation by considering their interactions in the lead, which will induce electromagnetic showering but not hadronic. The scintillator material detects the shower development and the photons are collected and transported via Wavelength Shifter fibres (WLS) to multianode photomultipliers.

Electromagnetic calorimeter

The electromagnetic calorimeter (ECAL) is the third layer of the calorimetry system. It is a sampling calorimeter constructed from sixty six alternating layers of 2 mm thick sheets of lead and 4 mm thick scintillator plates aligned perpendicular to the beam axis. It yields a total radiation length of $25X_0$. The radiation length, X_0, is the distance over which a charged particle will lose $\frac{1}{e}$ of its energy through Bremsstrahlung radiation. The scintillating material is read out using 'Shaslik' technology [54], where the WLS fibres are embedded into each plate.

The ECAL energy resolution for energy, E, in GeV/c is given by Equation 3.7 [53]. The first term takes into account the statistical fluctuation in the shower and the second, the systematic uncertainties, for example calibration uncertainties. The symbol $\oplus$ denotes that these two terms are added in quadrature.

$$\frac{\sigma_E}{E} = \frac{10\%}{\sqrt{E}} \oplus 1\% \tag{3.7}$$

Hadronic calorimeter

The Hadronic calorimeter (HCAL) is the final component in the LHCb calorimetry system. The HCAL is a sampling calorimeter constructed from alternating layers of 16 mm thick iron sheets and 4 mm thick scintillator plates positioned parallel to the beam axis. It has an overall depth of $5.6\lambda_I$, where λ_I is the interaction length of a particle. It is a measure of the mean path length through matter that is required to reduce the energy of a charged particle by a factor of $\frac{1}{e}$. The scintillating material is read out by WLS fibres running along the edge of the plates.

The energy resolution of the HCAL is given by Equation 3.8 [53].

$$\frac{\sigma_H}{E} = \frac{80\%}{\sqrt{E}} \oplus 10\% \tag{3.8}$$

3.2.8 Muon system

The muon system [55] is comprised of five stations, M1-M5, as illustrated in Figure 3.14. The first station, M1, is located before the calorimeter. It provides a measurement of the transverse momentum of the muons before they interact with the calorimeter material, which causes an increase in the rate of multiple scattering. The M2-M5 stations are positioned after the calorimeter system, interspersed with 80 cm iron shielding plates. Each muon station is divided into four regions, R1-R4, corresponding to their increasing distance from the beampipe.

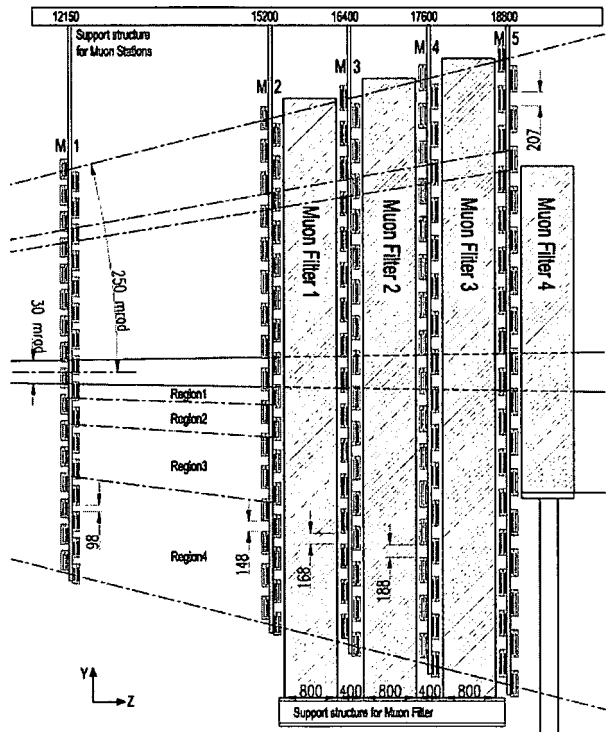

Figure 3.14: A schematic diagram showing a side view of the muon system in the y-z plane.

Two detector technologies are employed; Multi Wire Proportional Chambers (MWPC) and Gas Electron Multipliers (GEM). MWPC detectors are used in every region of all the muon stations except for the innermost region of M1, where triple GEM detectors are used. In this region the expected particle flux is too high and exceeds the safe MWPC ageing limit.

The MWPC detectors use a 2 mm wire spacing and a 5 mm thick gas gap, comprising of argon (45%), carbon dioxide (15%) and CF_4 (40%). In each of the regions R2-R4 of M1 two single gap MWPC detectors are used, reducing the amount of material in front of the calorimeters. In all regions of M2-M5 the MWPC detectors each have four gas gaps, arranged in groups of two.

The triple GEM detectors consist of three gas electron multiplier foils, at a distance of 1 mm apart, and placed between an anode and cathode plane. Two triple GEM detectors are used in the innermost region, R1, of M1.

The offline identification of muons is achieved by matching reconstructed tracks to hits in the muon chambers. A reconstructed track is extrapolated forwards into the muon system and a field of interest opened around the track in each of the muon stations. For a track to be selected as a muon it has to register a hit within the field of interest in a number of muon stations, which is defined by the momentum of the track. A summary of the muon stations which have to register a hit for tracks with a certain momentum is given in Table 3.1.

Track momentum (GeV/c)	Required muon stations
3<p<6	M2+M3
6<p<9	M2+M3+(M4 or M5)
p>10	M2+M3+M4+M5

Table 3.1: The muon stations required to register a hit within the field of interest for tracks in different momentum ranges

The muon identification efficiency, ϵ_μ, and misidentification rate, $\mathcal{R}$, are shown as a function of track momentum in Figure 3.15 for a sample of $B^0_d \to J/\psi K_S$ events. Using this sample ϵ_μ and $\mathcal{R}$ were found to be $94.3 \pm 0.3\,\%$ and $2.9 \pm 0.3\,\%$, respectively.

3.3 Trigger

The frequency of visible interactions in LHCb is expected to be 10 MHz, with a rate of only 100 kHz containing $b\bar{b}$ pairs. Approximately 15% of these $b\bar{b}$ pairs will be suitable for physics analysis because both the B meson and its decay products have to lie within the LHCb detector acceptance.

The LHCb experiment employs a three tier triggering system [56] to reduce the selected event rate from 10 MHz to 2 kHz. A flow diagram illustrating the functions of each part of the trigger is shown in Figure 3.16.

3.3.1 Level Zero trigger

The Level Zero trigger (L0) is a hardware implemented trigger using information from three sub-detectors: the pile-up, calorimetry and muon systems to reduce the selected

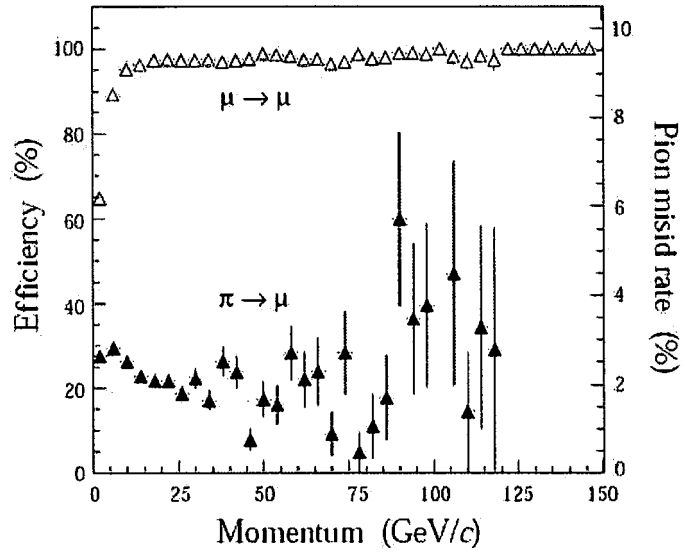

Figure 3.15: The muon identification efficiency (left-hand scale) and mis-identification rate (right-hand scale) as a function of track momentum in GeV/c. The open triangles correspond to muon identification, whereas the solid triangles represent muon mis-identification.

event rate from 10 MHz to 1 MHz. The decision to keep an event is taken by the L0 Decision Unit (L0DU) based on three criteria:

- **Decay product selection** - the highest transverse energy, E_T, particle and the two highest transverse momentum, p_T, muons are identified using information from the calorimetry and muon systems, respectively. The event is selected if at least one of the selected particles have E_T or p_T above the thresholds given in Table 3.2;
- **Track multiplicity selection** - information from the pile up and SPD are used to discard events that contain too high a number of tracks;
- **Multiple interaction selection** - information from the pile up system provides an estimation of the number of interactions per event and those with multiple interactions are rejected.

If an event is accepted the data from all of the sub-detectors is read out and sent to the LHCb processing farm, where the High Level trigger provides a more detailed analysis of the event.

L0	$h^{\pm}$	$\mu^{\pm}$	$\mu^{+}\mu^{-}$	$e^{\pm}$	γ	π^{0}
p_T or E_T (GeV/c)	3.5	1.3	Σ>1.5	2.6	2.3	4.5

Table 3.2: The p_T and E_T thresholds for the L0 trigger.

3.3.2 High Level trigger

The High Level trigger (HLT) [57] is a software implemented trigger using information from all of the LHCb sub-detectors. The event rate is reduced from 1 MHz to 2 kHz with the aid of algorithms implemented in C++ that run on a processing farm of approximately 1000 computing nodes. The HLT uses simple criterion to select events of interest and is subdivided into HLT1 and HLT2.

HLT1

HLT1 reduces the event rate from 1 MHz to 30 kHz. It confirms the L0 decision using information from the VeLo and tracking stations. HLT1 is composed of algorithms as illustrated in Figure 3.16.

HLT2

All events passing HLT1 are sent to HLT2, which performs an exclusive selection to reconstruct specific B final states and an inclusive selection to reconstruct generic B final states for resonances such as J/ψ decaying to two muons. The final HLT2 trigger decision is made by taking a *logical OR* operation on these two processes.

The expected trigger efficiencies at nominal luminosity for the $B_s \rightarrow J/\psi(\mu^+\mu^-)\phi(K^+K^-)$ decay mode are given in Table 3.3 [58].

Decay mode	ϵ_{L0}	ϵ_{HLT}	ϵ_{Total}
$B_s \rightarrow J/\psi(\mu\mu)\phi(K^+K^-)$	90%	80%	70%

Table 3.3: The expected trigger efficiencies for the $B_s \rightarrow J/\psi(\mu^+\mu^-)\phi(K^+K^-)$ decay at nominal luminosity

3.4 LHCb software

The LHCb software architecture is implemented using Gaudi [59], a C++ based object oriented framework that provides the basic functionality required during all stages of data processing within a high energy physics experiment. The simulation, reconstruction and analysis software packages are built against this framework, a description of which is given below.

The Gauss project [60] enables event generation and detector simulation. The proton-proton collisions at the LHC are generated using the Pythia [31] Monte Carlo generator, which also provides information on the position and the four-momenta of all the particles produced in a given event. A simulation of these particles as they traverse the detector is provided by the Geant4 toolkit [61]. An accurate description of the detector material and the magnetic field mapping are used to simulate the interactions of a given particle with the detector material, along with the trajectory of the particle in the magnetic field. Geant4 has the capability to fully simulate the interactions of hadrons with momenta greater than 10 MeV/c and leptons and photons with momenta greater than 1 MeV/c. Any interaction of a particle with an active area of the detector is stored as a hit, which contains links to the position and the type of the interaction

The final stage in the detector simulation is provided by the Boole project [62], which mimics the response of the readout electronics and L0 trigger hardware to the hits that have been generated by the Gauss application. The response of the individual sub-detectors to these hits is described by a set of algorithms that are specific to that sub-detector and have been fine tuned during testbeam and commissioning phases. Boole produces digitised data in the same format that will be produced in the real experiment.

The reconstruction of digitised events is performed by the Brunel package [63], the input of which can be either real data taken by the LHCb data acquisition system or the output from Boole. Brunel associates the clusterised output of Boole to form tracks, and provides particle identification information using the RICH detectors, the calorimetry and the muon systems. Finally, a protoparticle object containing links to

this information is written to a data summary tape (DST), which is used during physics analyses.

A physics analysis is performed using the DaVinci package [64]. The first process undertaken by DaVinci is to construct particles, with a defined type, from the protoparticles by placing a requirement on the quality of the PID information. Particles passing a common set of PID cuts are classed as the same type and form a set of standard particles. Vertices are then constructed and decay chains identified by combining particles. DaVinci has the functionality to make offline selections that identify the decay of interest whilst rejecting background processes.

The performance of the LHCb VeLo and its data acquisition boards is monitored using the Vetra project [65]. Vetra provides a bit-perfect emulation of the TELL1 processing algorithms, enabling the parameters that control the TELL1 boards to be tuned offline.

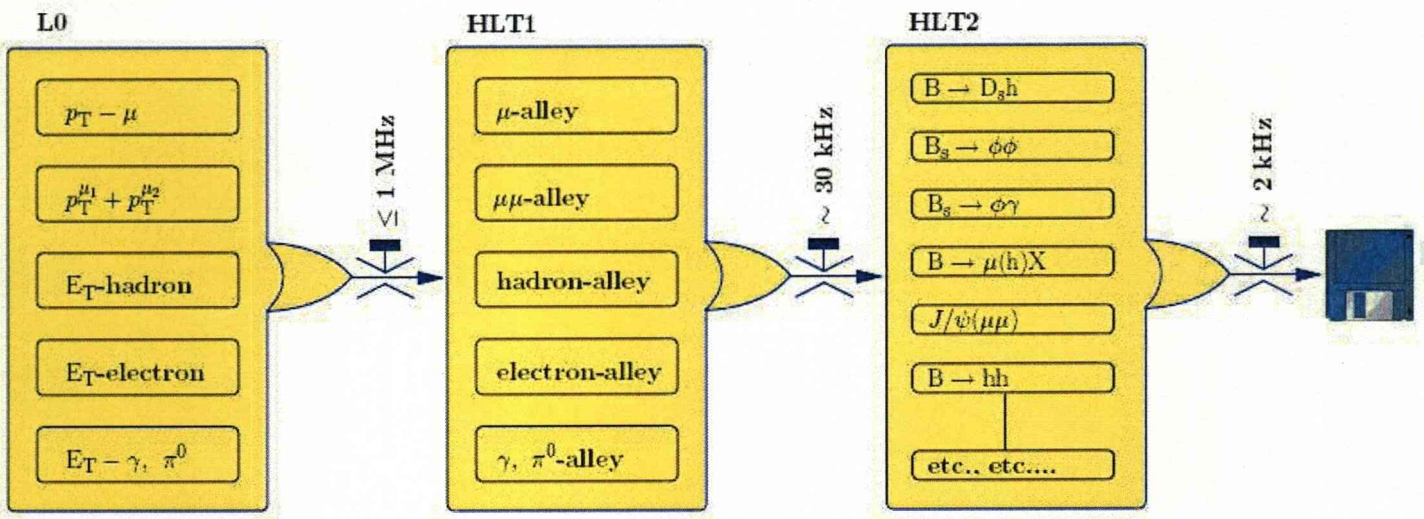

Figure 3.16: A flow diagram illustrating the trigger components; the hardware based L0 trigger that reduces the event rate from 10 MHz to 1 MHz, and the software implemented HLT, subdivided into HLT1 and HLT2, which takes the recorded event rate down to 2 kHz.

Chapter 4

Investigating crosstalk in the LHCb VeLo sensors

This chapter presents an analysis of the crosstalk observed in testbeam data taken with the final production VeLo modules. A brief description of the testbeam setup is given in Section 4.1, followed by a description of how the sensors are read out in Section 4.2. A discussion about crosstalk and its effect on the testbeam data is given in Section 4.3. The generation of Monte Carlo simulated testbeam data is discussed in Section 4.4, followed by the data analysis in Sections 4.5 and 4.6. The simulation of crosstalk is discussed in Section 4.7, and the data correction method in Section 4.8. Concluding remarks are given in Section 4.9.

4.1 VeLo testbeam

In autumn 2006 a testbeam was carried out at CERN to understand the characteristics and determine the performance of the final production VeLo modules before each VeLo half was assembled and the completed detector positioned in the LHCb pit. A schematic diagram illustrating the experimental setup employed during the testbeam is given in Figure 4.1. Ten modules were mounted on a detector half at the z positions given in Table 4.1, and placed inside the vacuum tank built for the final system. Nine of the ten VeLo modules used in the testbeam contained n in n silicon sensors, whilst the tenth module, M26, contained n in p silicon sensors.

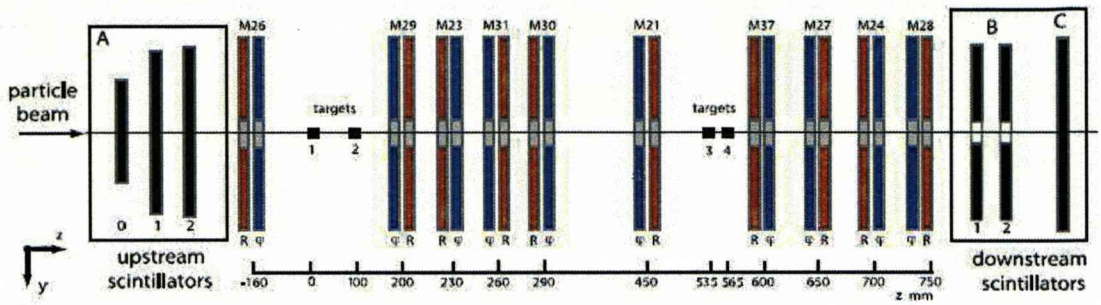

Figure 4.1: A schematic diagram of the top view of the experimental setup employed in the testbeam. From left to right are modules are: M26, M29, M23, M31, M30, M21, M37, M27, M24 and M28. The R sensors are shown in red and the ϕ sensors in blue.

Data were taken using two beam configurations; a 400 GeV/c proton beam and a 180 GeV/c meson beam, comprising mainly of pions. Four module readout configurations were employed, each reading out 6 modules simultaneously, enabling each module to be analysed in detail. The data used in the analysis presented in this chapter were taken with the modules read out in configuration 3. The modules active in this configuration are shown in Figure 4.2. This setup allows tracks to be extrapolated over a distance of 812 mm between modules M26 and M27, so that a measurement of the slope of the tracks can be obtained. The four modules grouped together enable an accurate measurement of the track positions to be determined.

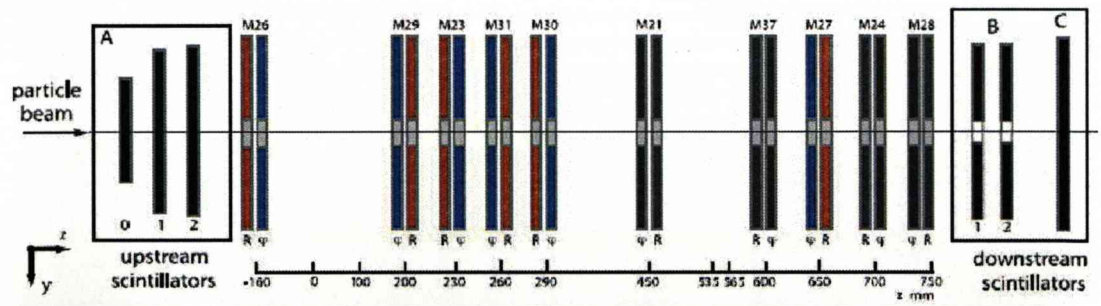

Figure 4.2: A schematic diagram of the top view of the experimental setup employed in configuration 3. The modules shown in black are not read out. From left to right the modules read out are: M26, M29, M23, M31, M30 and M27. The distance between the first and last modules is 812 mm.

The final electronics and cooling systems were employed during the testbeam, taking

data in air and in vacuum, with the modules reaching a temperature of $-3\,^{\circ}\mathrm{C}$ at a pressure of 10^{-3} mbar. This confirmed that the module positions remained stable during the transition between air and vacuum and throughout temperature cycling. Data were taken with the beam incident on the silicon sensors at 0°, 4° and 8° with respect to the beamline, providing a means of assessing the hit resolution as a function of angle. Data were also taken with the beam incident on two sets of lead targets, the positions of which were displaced from the beam axis to emulate the VeLo in open and closed positions. This created reconstructible primary vertices, enabling the fine tuning of the vertex reconstruction algorithms.

Sensor	z position (mm)	Sensor	z position (mm)
M26 R	-161	M26 ϕ	-159
M29 ϕ	199	M29 R	201
M23 R	229	M23 ϕ	231
M31 ϕ	259	M31 R	261
M30 R	289	M30 ϕ	291
M21 ϕ	449	M21 R	451
M37 R	599	M37 ϕ	601
M27 ϕ	649	M27 R	651
M24 R	699	M24 ϕ	701
M28 ϕ	749	M28 R	751

Table 4.1: The z positions of the silicon sensors of the modules mounted in the detector half.

4.2 VeLo sensor read out

The information from the sensor is read out in hardware channel order, the order in which the readout channels are read out is dictated by the positions of the routing lines on the sensor. The subsequent analyses are performed on software strip ordered data, this is the order of the strips from left to right as they physically lie on the sensor. For the ϕ sensors the strips in the inner region of the sensor are numbered first and

then those of the outer region. On the R sensors each quadrant is numbered, from the inner radius outwards, before the strips of the next quadrant are numbered. In hardware channel order the channels in each quadrant of the R sensor are still read out consecutively, however, the read out order of the channels on the ϕ sensors is more complicated. Figure 4.3 illustrates part of the read out chain for the ϕ sensors. It can be seen that inner and outer channels intermingle in the readout chain, with hardware channel zero being the last software strip in the inner region, and hardware channel one being the penultimate software strip in the outer region.

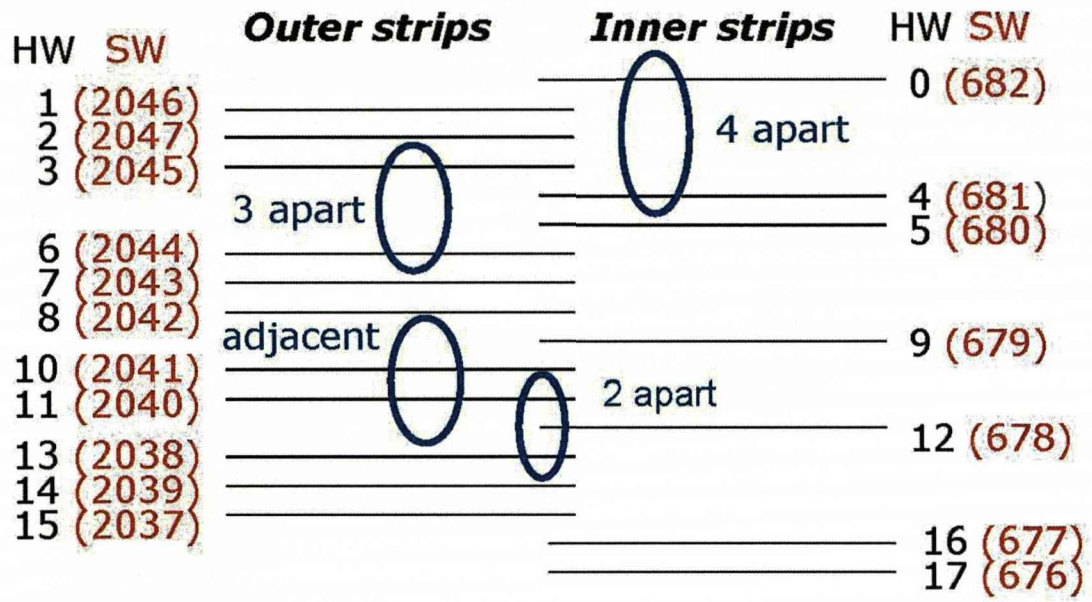

Figure 4.3: A schematic diagram illustrating the readout order of the channels on the ϕ sensors.

4.3 Crosstalk

Crosstalk is the phenomenon by which a signal in one readout channel spreads into another channel. This undesirable effect seen in the data taken with the VeLo modules is thought to have three possible causes:

- **Capacitive coupling** Capacitive coupling on the silicon sensors occurs between an implanted strip and a readout strip and also, between two implanted strips;

- **Sampling time** The information stored on the readout chip is nominally sampled in the peak charge position of each 25 ns bin or 4 ns after this to obtain optimal spillover suppression. If the sampling time is offset such that it is sampling too early then a channel could be sampled on the falling edge of the signal in the previous channel. Alternatively, if the sampling time is too late then a channel could be sampled on the rising edge of the signal in the next channel;

- **Cable compensation** Cable compensation is required because higher frequency signals are attenuated more than lower frequency signals as they travel down the 60 m cable from the repeater board to the TELL1 board. To account for this the Driver card on the ArX card of the repeater board amplifies the signals to ensure that at the end of the transfer line the signals received by the TELL1 boards are as close as possible to the input. In the testbeam the cables were not compensated because they were only 15 m in length, meaning that a frequency based correction, if, applied, would have resulted in signals of higher frequencies than those input being received by the TELL1 boards. The absence of cable compensation results in distortions of the signals as they are transferred down the cable, with the possibility of some signals arriving earlier or later than expected, thus, spreading into the signal from one channel into another.

Crosstalk affects the data by altering the distribution of charge within a cluster which may result in the loss of a strip from a cluster or the addition of a strip to a cluster. An oscilloscope trace illustrating the effects of crosstalk on the data is shown in Figure 4.4. An unaffected signal, shown as a blue peak on the trace, would be confined to a single 25 ns time bin, whereas a crosstalk affected signal (yellow) would be dispersed into the neighbouring bins.

4.4 Monte Carlo simulated data

Monte Carlo simulated testbeam data has been generated with the beam parameters tuned to match those of the beam that illuminated the sensors when the dataset used in this analysis was taken.

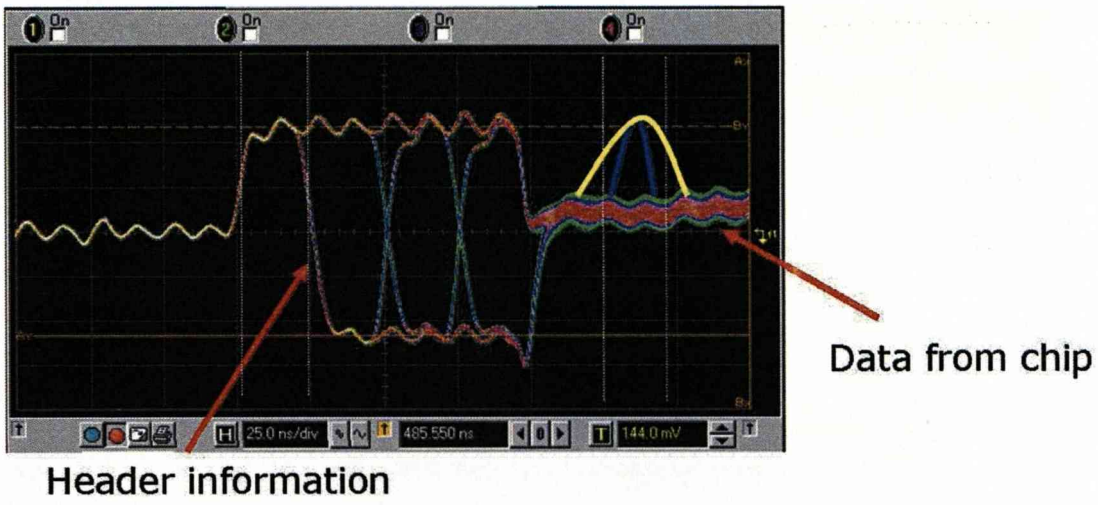

Figure 4.4: An oscilloscope trace showing the data readout by the Beetle chip. Each bin is 25 ns in width. The yellow peak represents a signal that has been affected by crosstalk. The signal has spread into the neighbouring bins. The blue peak represents a signal that is not affected by crosstalk.

4.5 Data analysis method

The analysis discussed in this chapter has been performed using Vetra and uses Zero Suppressed (ZS) data, where only strips with ADC values above a certain threshold are recorded in the data.

The standard LHCb VeLo clustering [68] has been performed on the data. The clustering algorithm searches software strip ordered data for a strip with an ADC value greater than a *seeding threshold* value. In principle this value can be different for each strip, however, during the testbeam it was kept constant at 10 ADC counts. Once a strip with an ADC value above this threshold is found it becomes a *seeding* strip and its neighbouring strips are considered to see if they have an ADC value above the *low threshold* value, which determines additional strips in the cluster. This value was set to 5 ADC counts throughout the testbeam. A cluster can be either:

- A one strip cluster as the strips either side of the seeding strip have ADC values below the low threshold value;
- A two strip cluster where one of the neighbouring strips has an ADC value above the low threshold value;

- A cluster containing three or more strips where the ADC values of both neighbouring strips are above the low threshold value.

Cuts were subsequently placed on the clustered data to remove any clusters formed on strips that were identified as noisy during module production at the University of Liverpool, and which are recorded in the VeLo module production database [69]. In addition, cuts have been placed on the beam profile to reduce the number of clusters caused by particles that have undergone significant multiple scattering. The beam profile distribution as the beam traversed the inner region of the ϕ sensor of M29 is shown in Figure 4.5, the red lines indicate the cuts placed on the distribution. A cut has also been placed on the data to remove clusters formed on strips that are read out on a chip boundary, where the binary header signal is attached to the analogue data signal. This removes any contribution from the header spillover into the data signal.

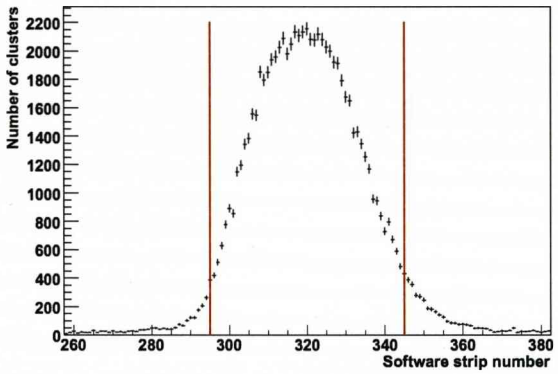

Figure 4.5: The profile of the beam as it traverses the ϕ sensor of M29. The red vertical lines indicate the cuts placed on the beam profile. Strip numbers below 683 are in the inner region of the ϕ sensor.

The fraction of two strip clusters as a function of strip pitch for the ϕ sensors is shown in Figure 4.6. The distribution deviates from theoretical expectation, which suggests that in low density regions, where the strips on the sensor are closer together, there should be a large fraction of two strip clusters. As the strip pitch increases the number of two strip clusters decrease until a plateau is reached. In this region the strips are too far apart for the charge to drift and be deposited on two strips, it is far more likely

for one strip clusters to be found in this region of the sensor. Each sensor of a given geometry, R or ϕ, has the same number of strips of the same length and the same pitch. Therefore, should yield a similar fraction of two strip clusters. Examining Figure 4.6 it can be seen that at a strip pitch of 70 μm the fraction of two strip clusters varies between 25 % and 41 %, depending on the module under consideration.

An explanation for the observed difference between the sensors is the effect of crosstalk on the data, as crosstalk, whatever its origin, will affect each sensor differently. This assumption will be investigated further in Sections 4.6, 4.7, and 4.8, where the ratio of charge in two strip clusters will be examined; a method for modelling crosstalk will be discussed; its effects will be removed from the data.

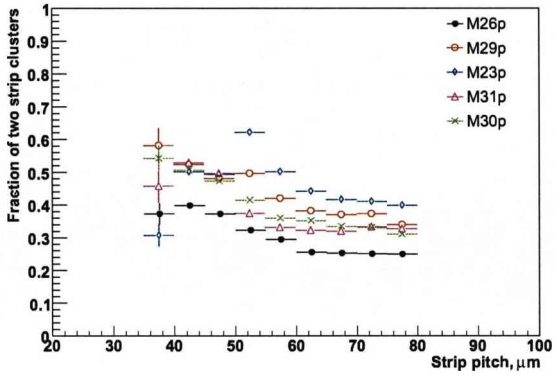

Figure 4.6: The fraction of two strip clusters as a function of strip pitch for ϕ sensors. Data for each sensor are represented by different coloured markers. The errors shown are statistical.

4.6 Investigating cluster charge ratio

Clusters can fall into one of two categories and are divided up accordingly, depending on whether the first channel that is read out has a higher or lower ADC value than the second channel.

Theoretically, it is expected that the number of clusters in each of the two categories will be similar, with similar ratios of charge, yielding symmetrical distributions. An asymmetrical distribution provides evidence of clusters in which there is a large ratio

of signal seen in the two channels. A significant number of such clusters suggests that there is crosstalk between the channels.

The ratio of ADC values in two strip clusters found in the simulated data before the effects of crosstalk have been included is given in Figure 4.7. Clusters where the ADC value of earlier channel in the readout chain is higher than the ADC value of the later channel are represented by the black solid line, whereas the markers represent clusters where the later channel that is read out has a higher ADC value than the earlier channel. It can be seen that the two distributions are consistent, showing that the simulation is the same in channel order.

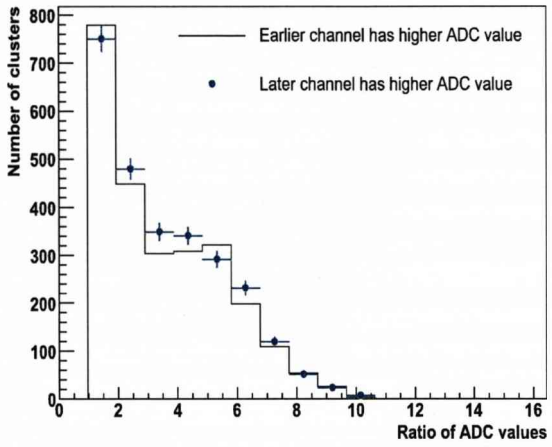

Figure 4.7: The ratio of ADC values in the Monte Carlo simulated data clusters. The black solid line represents clusters where the earlier channel in the readout chain has a higher ADC value than the later channel. The blue markers represent clusters where the later channel in the readout chain has a higher ADC value than the earlier channel.

The ratio of charge in two strip clusters found in the testbeam data is given in Figure 4.8 for the ϕ sensor of module M29, where the data is divided according to the proximity of the readout channels. Examining Figure 4.8(a) a significant asymmetry can be seen between the two distributions, which decreases as the number of channels separating the readout strips in the same cluster increases. There is a bump in the distribution represented by the black solid line on the plots that occurs between the ratios of eight and eleven, this is where the earlier channel that is read out has a higher ADC value

than the later channel. It may be caused by:

- One strip clusters, these can fake a two strip cluster if a small amount of its charge has bled into a second strip, pulling it just above the low threshold boundary which defines additional strips of a cluster;
- Two strip clusters where charge from the strip with the lowest ADC value has spread into the strip with the higher ADC value making the cluster very asymmetrical, and having a high ratio of charge;
- Three strip clusters that have been converted to a two strip cluster because the charge on the strip with the lowest ADC value has spread to one of the other strips in the cluster, and, so pulling it below the low threshold value.

The simulation takes into account the possibility of the data being affected by crosstalk on the sensors by adding 1 % of the charge on a strip to each of its nearest neighbours. Crosstalk that originates elsewhere, for example charge sharing in the readout cable; or an offset in the sampling time of the readout channels, is not accounted for. The exact contribution from each of these sources can not be distinguished in the data, however, in terms of providing a means of quantifying the crosstalk and correcting for it in the data the solution is the same.

4.7 Simulation of crosstalk

An algorithm has been developed to account for the effects of crosstalk in the data by migrating charge between strips. The algorithm takes the ADC values of the simulated data and performs three functions; adds noise, smears the data, and finally re-clusters the data. These processes are shown graphically in Figure 4.9.

The clustering process is applied to Non-Zero Suppressed data (NZS)[71], this is the complete readout for every channel for every event in the sensor. In order to smear and then re-cluster the data, the ZS data that we have has to resemble NZS data, where all channels have an ADC value, whether as a result of signal or noise. The noise values are re-introduced into the simulation using random numbers. Gaussian distributed random numbers with a mean of zero and a width of three are given to the channels that have no ADC value because it is estimated that the RMS value of the noise after

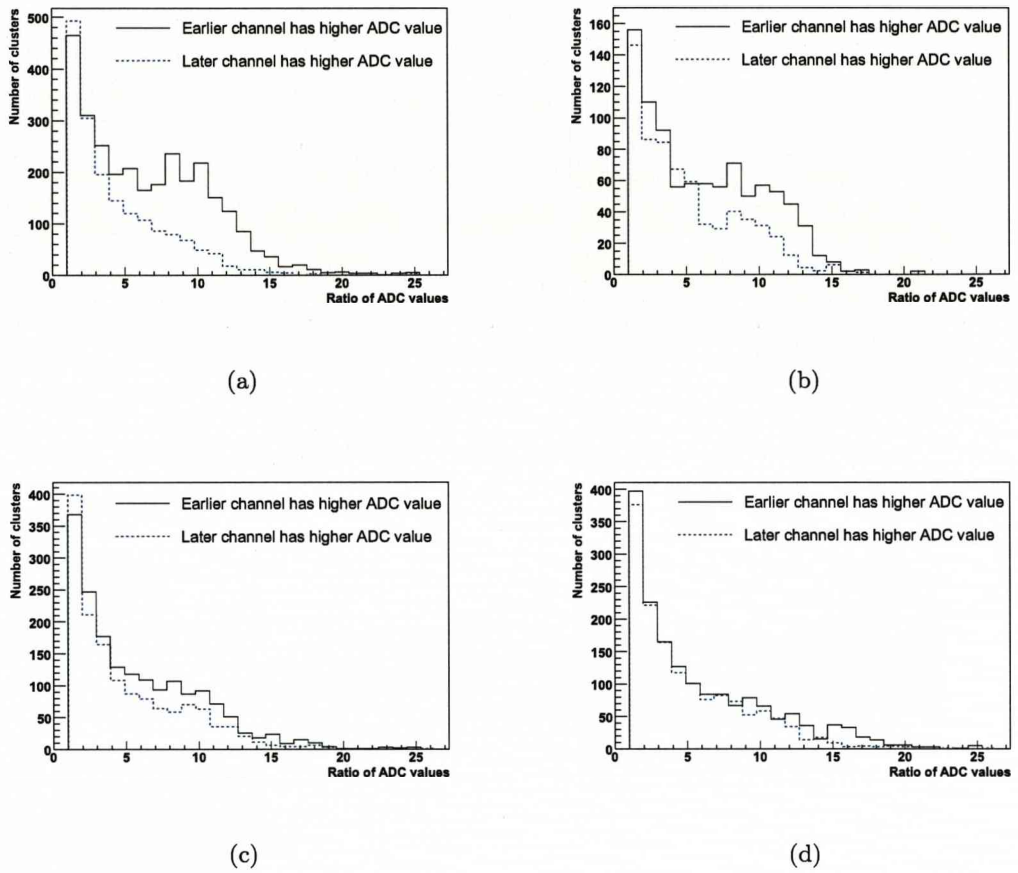

Figure 4.8: The ratio of ADC values for the ϕ sensor of module M29. The black solid line represents clusters where the first channel in the readout chain has a higher ADC value than the second channel. The blue dashed line represents clusters where the second channel in the readout chain has a higher ADC value than the first channel. The clusters are divided into four categories: where the channels in the same cluster are read out consecutively (a); channels in the same cluster are separated by two other channels in the readout chain (b); channels in the same cluster are separated by three other channels in the readout chain (c); and channels in the same cluster are separated by four other channels in the readout chain (d).

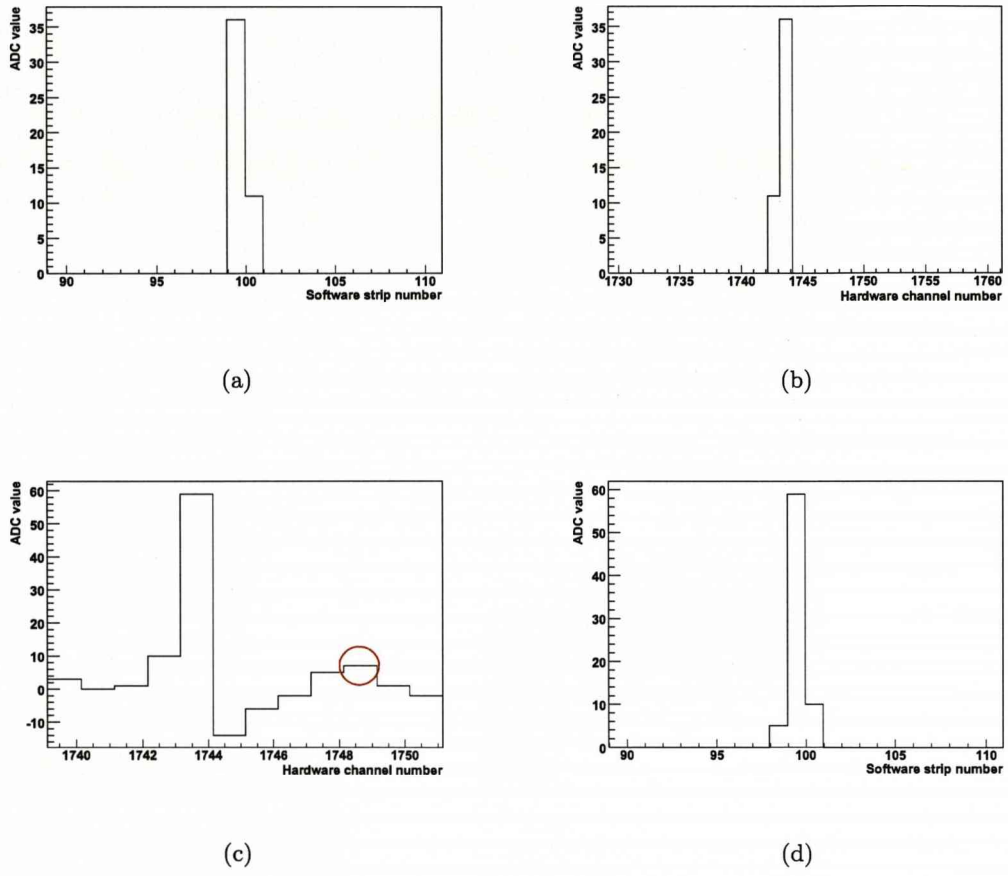

Figure 4.9: An illustration of the main steps required to re-model the Monte Carlo simulated data to best describe the testbeam data. (a) shows a two strip cluster in software strip order. It is converted into hardware channel order in (b). Random numbers are added to the data to make the data NZS-like and the data is smeared (c). The channel circled in red has been pulled above the low threshold boundary. The data is converted back into software strip order and clustered in (d). It can be seen that the original two strip cluster has become a three strip cluster.

the pedestal following is 3 ADC counts [72]. Uniformly distributed random numbers between -0.5 and 0.5 are added to the ADC values of the channels on which a cluster has formed.

The analysis uses the now NZS-like simulated data to model the crosstalk. This is done by smearing the Monte Carlo simulation to represent the charge sharing. This process is undergone with the data in hardware channel order (which is where the effect of crosstalk manifests itself). One set of smearing factors are required to describe the data taken with the R sensors because the strips in the same cluster are read out consecutively. Four sets of smearing factors are required for the ϕ sensors because strips in the same cluster can be separated by up to four other strips when they are read out (see Section 4.2), meaning that the crosstalk effect can spread up to four channels.

The process of smearing the ADC value of a channel is described by Equation 4.1. The ADC value of a channel, i, is affected by a factor, f_j, of the ADC values of the previous channels in the read out chain *(i-j)*, and a factor, g_j, of the ADC values of the channels that are to be read out next *(i+j)*. A charge conservation factor is also included in this equation.

$$adc_{i(smeared)} = \frac{adc_i}{1+\sum_j f_j+\sum_j g_j} + \sum_j f_j \cdot adc_{i-j} + \sum_j g_j \cdot adc_{i+j} \qquad (4.1)$$

The values of f_j and g_j can be positive or negative. A positive value indicates that some of the charge on a strip is dispersed to the neighbouring strips, whereas, a negative value means that charge is 'sucked in' from the neighbouring strips. The effect of positive and negative smearing values are shown graphically in Figure 4.10. In Figure 4.10(a) the black solid line shows the distribution before any smearing has been applied. A value of 36 ADC counts has been assigned to channel 1743, with random numbers given to the remaining channels. The blue dashed line represents the distribution after a smearing value of f_1= 0.2 has been applied, this has caused a fraction, 0.2×36, to be transferred to channel 1744. In Figure 4.10(b), where a negative value, f_1= -0.2 is applied, channel 1744 has been reduced, with the charge transferred into channel 1743. Figure 4.10(c) shows how applying a positive value of f_1 equal to 0.2 and a negative value of g_1 of -0.1 affects the distribution.

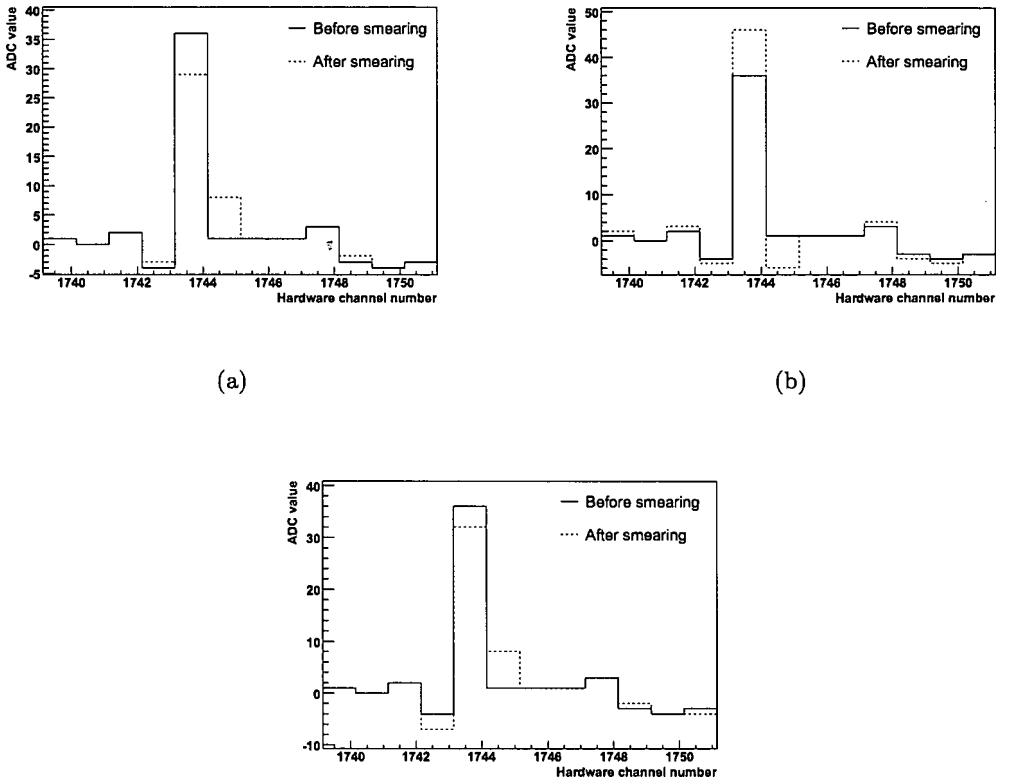

Figure 4.10: The effect of smearing factors on the Monte Carlo simulated data. The black solid line shows the data before any smearing factors have been applied, and the blue dashed line shows the data after it has been smeared. In (a) a positive smearing factor of f_1=0.2 is applied to the data; in (b) the data is smeared by a negative value of f_1=-0.2; and in (c) the data is smeared by f_1=0.2 and g_1=-0.1.

Once the smearing process has been completed the data is reverted back into software strip order and clustered. This process is based on the standard clustering algorithm for the VeLo, as discussed in Section 4.5, with the value of the seeding strip required to be greater than 10 ADC counts and the low threshold, to determine additional strips of the cluster, set to be 5 ADC counts.

4.7.1 Determining the correct smearing factors to emulate data

The key to successfully model the crosstalk is to obtain the best combination of smearing factors for each sensor that are needed to make the Monte Carlo simulation reflect the data. The data from each sensor is analysed individually, with the ϕ sensor data divided up according to how many channels the strips of the same cluster are separated by in the readout chain. The data is smeared by all combinations of f_j and g_j in the range -0.5 to +0.5, in increments of 0.02, and χ^2 comparison is carried out between the data and smeared simulation at every step. The combination of smearing factors that give the lowest χ^2 best describe the data. The distribution of the χ^2 values as a function of the smearing factor, f_1, for the ϕ sensor of M29, where the channels of the cluster are adjacent in the read out chain is shown in Figure 4.11. The blue circle highlights the lowest value. This is equivalent to a minimisation to two free parameters for the R sensors and eight for the ϕ sensors.

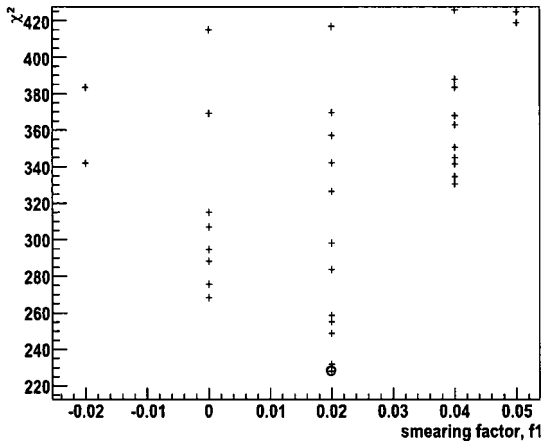

Figure 4.11: The distribution of the χ^2 values as a function of the smearing factor, f, for the ϕ sensor of M29. The lowest value is circled in blue.

4.7.2 Results and errors

The values of the smearing factors required to correct the data are given in Tables 4.2 and 4.3 for the R and ϕ sensors, respectively, along with their statistical errors.

4.7.3 Statistical errors

The statistical errors on the smearing factors are determined using the MINOS algorithm [73]. MINOS provides the best method for calculating the errors because it does not assume that the distribution has a parabolic shape, but instead follows the distribution out from the minimum to find where it crosses the next point. For distributions with several free parameters MINOS describes the error as being the minimum value of χ^2 plus a value by which the χ^2 must increase. This value depends on the confidence level required and the number of free parameters.

The χ^2 that is used to determine the best combination of smearing factors has two free parameters per number of channel separation, f_j and g_j. According to the MINOS method a value of 2.41 is required to calculate the values of the smearing factors to within one standard deviation (1σ). Thus, the error on each smearing factor is calculated by finding the value of the smearing factor after the χ^2 has changed by 2.41.

The mean values of the smearing factors that best describe the data recorded for each sensor are given at the bottom of Tables 4.2 and 4.3 for the R and ϕ sensors respectively, along with the RMS of these values and their χ^2. The standard deviation required to calculate the value of the χ^2 is 0.07 for the values of f_j and 0.04 for the values of g_j. These values are determined from the Gaussian distributions produced for the minimum values of f_j and g_j when varying the random seed and smearing the data. The number of degrees of freedom is four for the ϕ sensors and three for the R sensors. The number of degrees of freedom are determined by the number of sensors minus one, taking into account that the mean value of the smearing factor has been calculated. Consulting the table of critical values for χ^2 [74] it is found that the values of each smearing factor obtained for all like sensors are consistent with each other to within one sigma (1σ).

R sensors		
Module	f	g
M26	0.04±0.02	-0.34±0.01
M29	0±0.008	-0.28±0.01
M31	0.1±0.02	-0.44±0.01
M30	0.08±0.02	-0.35±0.01
Mean	0.06	-0.34
RMS	0.04	0.06
χ^2	0.41	3.17

Table 4.2: The values of smearing factors, f and g obtained for the R sensor data, together with the mean values, RMS and χ^2.

ϕ sensors								
Module	f_1	g_1	f_2	g_2	f_3	g_3	f_4	g_4
M26	-0.15±0.01	-0.28±0.01	0.1±0.02	0.02±0.02	0±0.01	-0.04±< 0.01	-0.03±< 0.01	-0.08±0.01
M29	0.02±0.01	-0.26±0.01	0.05±0.01	-0.1±0.01	-0.03±0.08	-0.04±0.01	-0.04±0.01	-0.08±0.01
M23	0.03±0.01	-0.22±0.02	0.04±0.01	-0.12±0.01	-0.1±< 0.01	-0.12±0.01	-0.04±0.01	-0.02±0.01
M31	0.1±0.02	-0.44±< 0.01	0.04±< 0.01	0±0.02	0±0.02	-0.02±< 0.01	-0.02±0.02	-0.06±0.02
M30	-0.16±0.01	-0.3±0.01	0.08±0.01	0.04±0.02	0±0.01	-0.05±< 0.01	0±0.01	-0.01±< 0.01
Mean	-0.03	-0.3	0.06	-0.03	-0.03	0.05	-0.03	-0.04
RMS	0.1	0.07	0.02	0.07	0.04	0.03	0.01	0.04
χ^2	2.7	4.38	0.15	3.33	0.39	1.25	0.06	1.27

Table 4.3: The values of smearing factors, f_j and g_j, obtained for the ϕ sensor data, together with the mean values, RMS and χ^2.

4.7.4 Systematic Uncertainty

A source of systematic uncertainty that can arise from modelling the crosstalk seen in the VeLo sensors is the process of creating NZS data from NZ data using random numbers for the 'zero suppressed' channels. To estimate the degree of bias in this method the Monte Carlo simulated data where no effects of crosstalk have been included has been smeared and then re-clustered. A χ^2 comparison between the original simulated data and the simulated data after it has been smeared and reclustered has found that the values of f_j and g_j that best represent the simulated data are consistent with zero, showing that the method is unbiased. Figure 4.12 shows the ratio of charge in two strip clusters for the original simulated data and the simulated data after it has undergone smearing and reclustering. The lines represent the original simulated data and the markers show the re-clustered simulation. The solid black line and marker represent the clusters where the earlier channel that is read out has a higher ADC value than the later channel and the blue dashed line and marker show clusters where the later channel in the read out scheme has a higher ADC value than the earlier channel.

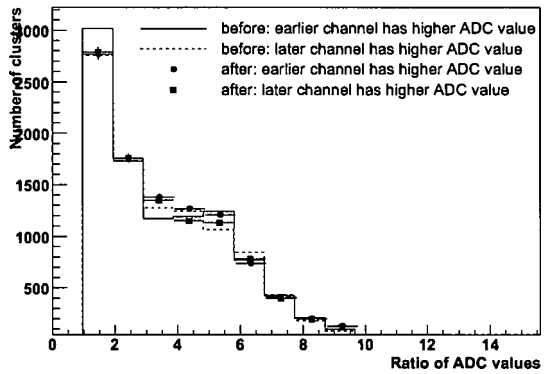

Figure 4.12: The ratio of ADC values seen in the Monte Carlo simulated data before and after random numbers have been added and the simulated data re-clustered. The lines correspond to the original Monte Carlo simulated data and the markers correspond to the simulated data after random number have been added and it re-clustered. The black solid line and markers represent clusters where the earlier channel in the readout scheme has a higher ADC value than the later channel. The blue dashed line and markers represent clusters where the later channel that is read out has a higher ADC value than the earlier channel.

4.8 Data Correction

Once the best set of smearing factors for each sensor have been identified the undesirable effects that crosstalk introduces into the data can be corrected.

Taking a cluster where the first channel is earlier in the readout chain than the second channel, the ADC value of the first channel in the cluster, ADC_0, is affected by a factor g of the second channel in the cluster, ADC_1, to produce the crosstalk affected ADC value that is seen in the data, and which is shown in Equation 4.2 as ADC'_0.

$$ADC'_0 = \frac{ADC_0}{1+f+g} + ADC_1 \cdot g \tag{4.2}$$

$$ADC'_1 = \frac{ADC_1}{1+f+g} + ADC_0 \cdot f \tag{4.3}$$

Solving Equations 4.2 and 4.3 simultaneously results in the expressions for the crosstalk corrected ADC values, for the first and second strips of the cluster as shown in Equations 4.4 and 4.5, respectively.

$$ADC_0 = \frac{ADC'_0 - \frac{ADC'_1 \cdot g}{1+f+g}}{1+f+g-\frac{f \cdot g}{1+f+g}} \tag{4.4}$$

$$ADC_1 = \frac{ADC'_1 - \frac{ADC'_0 \cdot f}{1+f+g}}{1+f+g-\frac{f \cdot g}{1+f+g}} \tag{4.5}$$

The smeared simulation that best represents the testbeam data for the ϕ sensor of M29 is shown in Figure 4.13 for the four read out configurations, with the ratio of ADC values after the data has undergone correction given in Figure 4.14. The data correction method has not made the two distributions completely symmetrical, as theory expects. One reason for this is that the method of making the data NZS-like, smearing and then re-clustering it has reduced the amount of information available about the cluster, thus making such plots approximate. The analysis undertaken has only considered clusters

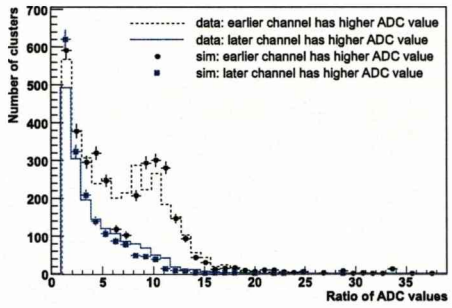

(a) Channels adjacent in read out

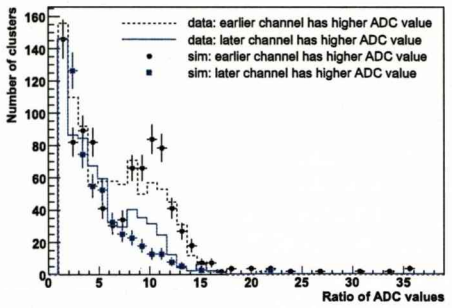

(b) Channels separated by two

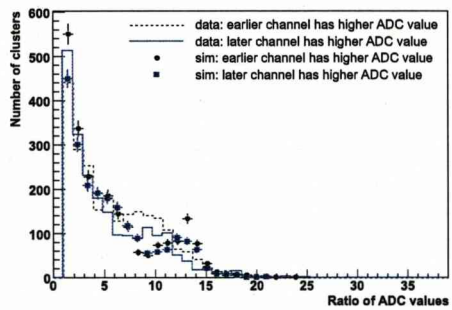

(c) Channels separated by three

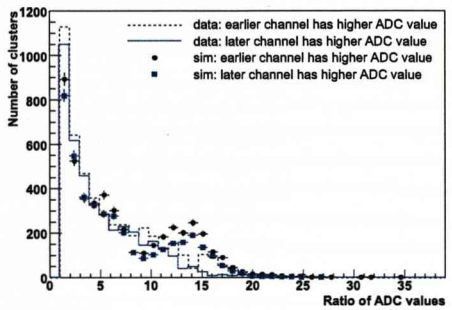

(d) Channels separated by four

Figure 4.13: The ADC ratio distribution for smeared simulated data (markers) that best matches testbeam data (lines) taken with the ϕ sensor of module M29.

that start off as two strip clusters and remain two strip clusters after data correction. The asymmetrical tail suggests that there are missing clusters in this region that had previously been one or three strip clusters as a result of the effect that crosstalk has on the data. It can be seen that the asymmetric tail becomes less prominent as the number of channels by which strips in the same cluster are separated increases. Calculations show that on average 12 % of one strip clusters and 5 % of three strip clusters are converted into two strip clusters as a result of the smearing process.

Using the crosstalk corrected data the fraction of two strip clusters as a function of strip pitch is examined again, yielding the results shown in Figure 4.15. At a strip pitch of 70 μm the difference in the fraction of two strip clusters seen in the different sensors

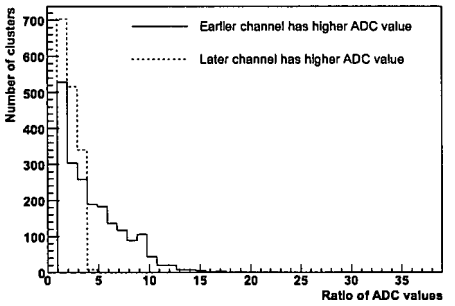

(a) Channels adjacent in read out

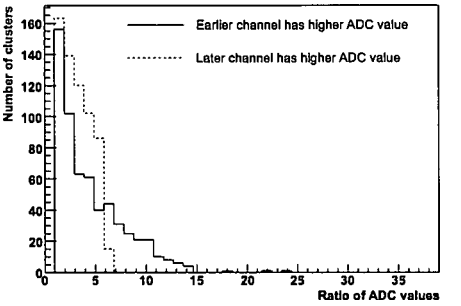

(b) Channels separated by two

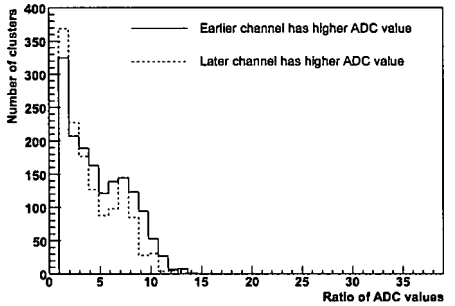

(c) Channels separated by three

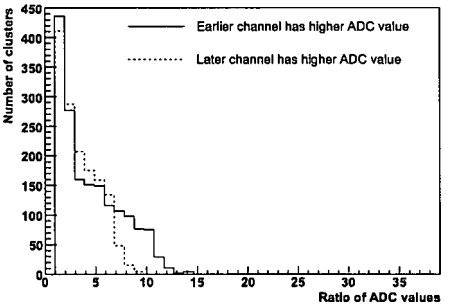

(d) Channels separated by four

Figure 4.14: Crosstalk corrected ADC ratio distribution for the ϕ sensor of module M29.

has been reduced by 6 %, varying between 23 % and 33 %.

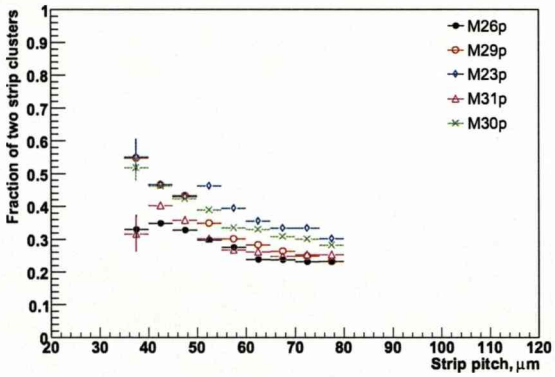

Figure 4.15: The fraction of two strip clusters in the crosstalk corrected data as a function of strip pitch. Data for each sensor is represented by the different coloured markers. The errors shown are statistical.

4.9 Conclusion

In order to quantify the crosstalk an algorithm has been developed that migrates charge between the channels of two strip clusters seen in Monte Carlo simulated data. The effect of this algorithm is to make the distribution of the ratio of ADC values match that of the two strip clusters seen in the testbeam data. This method produces a set of smearing factors, which can be used to alter the testbeam data to correct for the undesirable effects that crosstalk introduces into it. The magnitude of the smearing factors required to correct for crosstalk in the data were larger than expected, which suggests that the origin of the crosstalk exhibited in the data results from a combination of charge sharing in the readout cables and an offset in the sampling time of the readout channels.

The data correction method designed to mask the effects of crosstalk seen in the testbeam data has largely eliminated the undesirable features seen in the distribution of the ratio of ADC values. The asymmetric tails produced are a consequence of approximations made in the method: a certain amount of information about each cluster is lost in the smearing process; it also only considers two strip clusters found in the testbeam data that remain two strip clusters after data correction. One and three strip

clusters found in the testbeam data and converted into two strip clusters as a result of data correction are not taken into account in the analysis. Therefore, the findings are approximate and are not expected to fully correct for the effects of crosstalk.

A large amount of crosstalk is not expected in the LHC collision data. The fully commissioned LHCb detector will have a correctly tuned sampling time and use the full 60 m transfer cables, thus reducing the effects of crosstalk. Any residual crosstalk can be removed using the Finite Impulse Response (FIR) filter on the TELL1 board.

Chapter 5

Signal to Noise Ratio in LHCb VeLo Sensors

This chapter will discuss the signal to noise ratio of the LHCb VeLo silicon sensors. An introduction is given in Section 5.1, followed by discussions about signal and noise in Sections 5.2 and 5.3, respectively. The signal to noise ratio is discussed in Section 5.4. Concluding remarks are given in Section 5.5.

5.1 Introduction

The signal to noise (S/N) ratio analysis presented in this chapter has been carried out using NZS data taken at the testbeam discussed in Chapter 4, Section 4.1. As with the crosstalk analysis data used in this analysis were taken in module configuration 3, in which modules: M26, M29, M23, M31, M30 and M27 were powered.

The S/N ratio of each sensor is an important quantity in monitoring the performance of the VeLo subdetector.

5.2 Signal

A schematic diagram of the process in which a charged particle induces a signal in the silicon sensor is given in Figure 5.1. A minimum ionising particle traversing the silicon interacts with the atoms in the silicon lattice via Coulomb scattering. The collision results in the ejection of one or more electrons from the silicon atoms, leaving behind

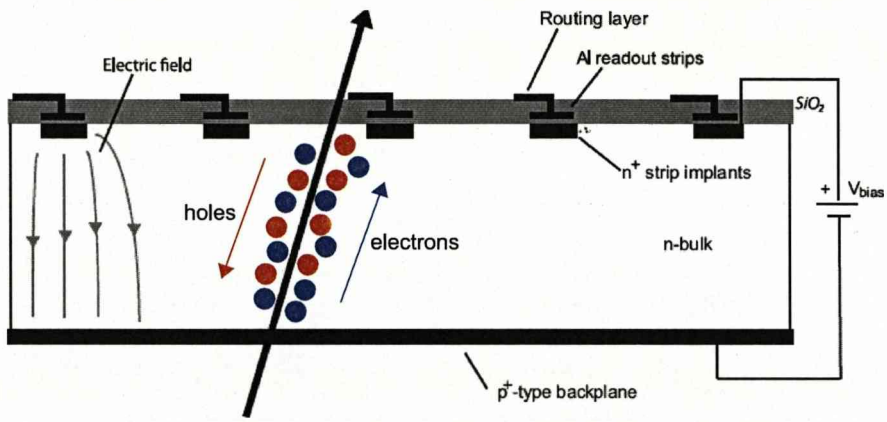

Figure 5.1: A schematic diagram illustrating the passage of a minimum ionising particle through a n in n silicon sensor.

a positively charged hole. The electric field induced by the HV power supply (V_{bias}) ensures that the positive and negative charge carriers travel in opposite directions. The electrons arrive at the strips and the signal is read out by the Beetle readout chips.

The shape of the signal takes the form of a Landau distribution [75]. The mean energy loss is significantly higher than the most probable value of energy loss. The tail of the distribution is caused by high energy electrons known as *delta rays*. The path of a charged particle through the silicon lattice is deflected by Coulomb repulsion with an electron in the silicon atom closest to it. This imparts energy on the electron, and the closer the charged particle passes to the silicon atom the more energy that is transferred. Electrons that gain a large amount of energy are ejected from the silicon atoms and cause secondary interactions.

5.3 Noise

Noise present in the system can adversely affect the ability to detect a particle induced signal. There are two primary sources of noise in silicon detectors; the front end transistor (FET) of the front end pre-amplifier, and leakage currents. The leakage current is essentially shot noise. It increases the more a sensor is irradiated, reducing

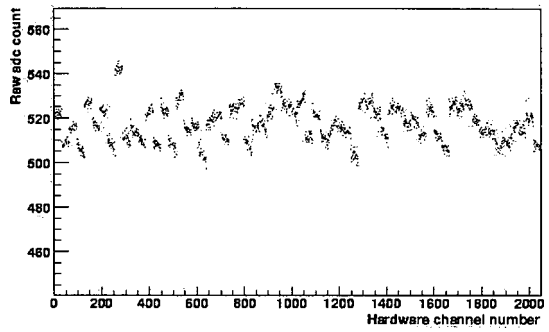

(a)

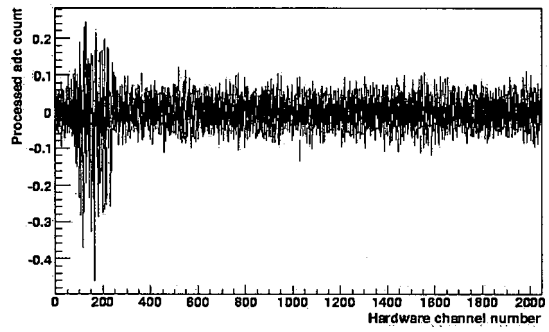

(b)

Figure 5.2: The raw (a) and processed (b) data for the ϕ sensor of M29 taken with the beam incident on the silicon sensors at 0°. Processed data refers to the data after it has undergone pedestal and common mode corrections.

the sensitivity of the S/N ratio measurement [76]. Operating the VeLo modules at a temperature of below -5°C will reduce this effect.

A noise analysis is carried out to identify and characterise the noise observed in the system, enabling the data obtained from each sensor to be correctly interpreted and analysed. Common mode noise can be identified and subtracted from the raw data during the TELL1 board processing. Pedestal subtraction and common mode correction centre the distribution about zero. The resultant, *processed* data is used in analyses. Figure 5.2 shows the raw (a) and processed (b) data can be seen.

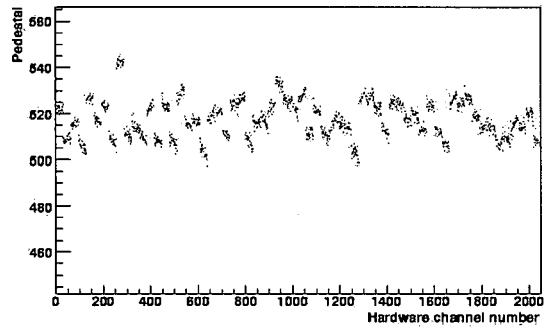

Figure 5.3: The pedestal as a function of hardware channel number for the ϕ sensor of M29.

5.3.1 Pedestal

The pedestal is an offset in the ADC value of a channel caused by the readout electronics. It is approximately 512 ADC counts, although the pedestal of a given channel is unique to that channel and varies over time due to its temperature dependence. The pedestal for each channel is calculated using a running average method [77].

5.3.2 Common mode

Common mode noise is noise affecting several channels in the sensor simultaneously. A sensor can be affected by electromagnetic fields induced by the charge of the proton beams. An inducted negative charge means that the front end amplifiers see a positive signal across the sensor. Common mode noise can also affect the group of 32 channels that are processed by the same port on the Beetle readout chips. A large signal in one strip draws a large current and so reduces the voltage of the power supply that is available to all of the front end amplifiers, thus, reducing the output of all of the other strips. Common mode correction identifies and removes this noise by performing a linear fit to the charge on each of the 32 channels in a group. The calculation is carried out on an event by event basis.

5.3.3 Residual Noise

The noise left in the system after pedestal subtraction and common mode correction can be determined on a per channel basis and is defined as the RMS of the ADC value of a strip. The RMS noise of a single strip is illustrated in Figure 5.5. This distribution

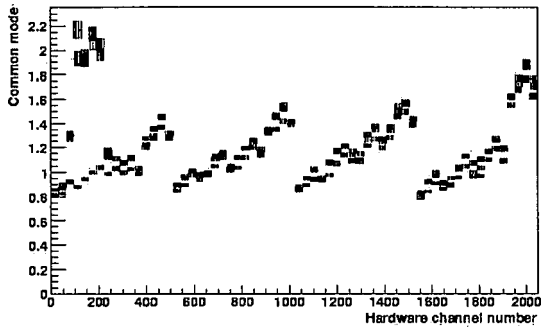

Figure 5.4: Common mode as a function of hardware channel number for the ϕ sensor of M29.

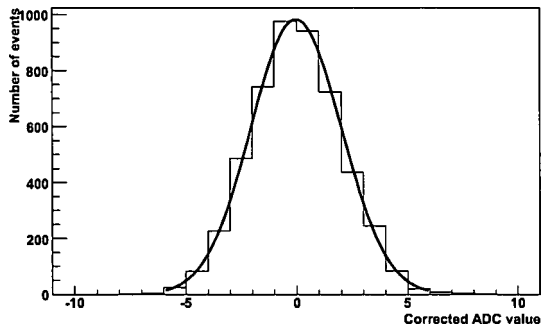

Figure 5.5: The RMS noise distribution for a single strip on the ϕ sensor of M29.

has a width of 2.0 ADC counts. The noise on a strip has a linear dependence on the combined capacitance of a strip and its routing lines, and therefore varies across each sensor and between the two types of sensor. The noise is expected to vary between one and three ADC counts [78].

For the purpose of this chapter the noise is calculated as an average across each sensor.

5.4 Signal to Noise Ratio

In this section a comparison between the theoretically expected and experimentally measured S/N ratio is made.

5.4.1 Theoretical Signal to Noise Ratio

The theoretically expected signal and noise, and, therefore, the S/N ratio, of a material can be determined if the physical and electrical characteristics of the material are known. A signal of 79 electrons is produced per micrometre of silicon [79]. Therefore, the expected signal in the 300 μm thick silicon sensors that form the active area of the VeLo modules is typically 23700 electrons. Theoretically it is assumed that the source of the noise in the system is the pre-amplifier of the Beetle chip. The equivalent noise charge (ENC) is given in Equation 5.1. The constant, A, is the noise of the pre-amplifer without a sensor attached and B is the response of the pre-amplifier to strips of different lengths. The values of A and B are 450 electrons and 50 electrons/pF, respectively [80]. The capacitative load of the detector, C, is 10 pF, yielding an expected noise of 850 electrons. Therefore, the maximum signal to noise ratio of the 300 μm thick silicon sensor is 28 signal electrons for every noise electron.

$$ENC = A + B \cdot C \tag{5.1}$$

In practice the silicon sensors are not exactly 300μm thick, and so the maximum signal that can be induced in a sensor varies between sensors. The theoretical S/N ratio for each sensor powered in the testbeam is given in Table 5.1.

5.4.2 Experimentally Measured Signal to Noise Ratio

Experimentally the S/N ratio is determined by fitting the processed ADC distribution. Such a plot exhibits a noise peak around zero and a signal peak at higher ADC values, as can be seen in Figure 5.6. A Gaussian fit is applied to the noise distribution to extract the mean value of the noise and a Landau is fitted to the signal distribution to extract the most probable value of the signal. The signal and noise values, along with the S/N ratio obtained for each of the silicon sensors employed in configuration 3 are given in Table 5.2.

A comparison between the maximum S/N ratio that can be obtained and the measured value shows that the experimentally obtained S/N ratio is somewhat lower than the

Sensor	Thickness (μm)	Signal (e)	S/N ratio
M26 R	316	24964	29.4
M26 ϕ	307	24253	28.5
M29 ϕ	304	24016	28.3
M29 R	307	24253	28.5
M23 R	309	24411	28.7
M23 ϕ	311	24569	28.9
M31 ϕ	304	24016	28.3
M31 R	301	23779	28.0
M30 R	309	24411	28.7
M30 ϕ	303	23937	28.2
M27 ϕ	305	24095	28.4
M27 R	300	23700	27.9

Table 5.1: The theoretical S/N ratio for each sensor. The maximum signal induced in a sensor is determined from its thickness. The noise is a constant 850 electrons as calculated by Equation 5.1.

theoretical value. A reason for this is the effects of crosstalk on the data. It was established in Chapter 4 that the data taken at the testbeam was affected by crosstalk and the results from that analysis indicate that the data taken with both the R and ϕ sensors exhibit crosstalk of the order of 30 %. In terms of the S/N ratio this means that a strip can lose up to 30 % of the charge deposited on it to its neighbouring strips, thus reducing the most probable value of the signal whilst the noise distribution remains constant.

An offset in the sampling time may result in the signal being sampled earlier or later than the peak charge position. This means that the amount of signal read out, and therefore, the S/N ratio, would be reduced.

5.5 Conclusion

The results of the S/N analysis presented in this chapter are comparable with other analyses [81]. However, the analysis presented in Chapter 4 indicates that the data taken at the testbeam was affected by crosstalk, which in turn affects the S/N ratios

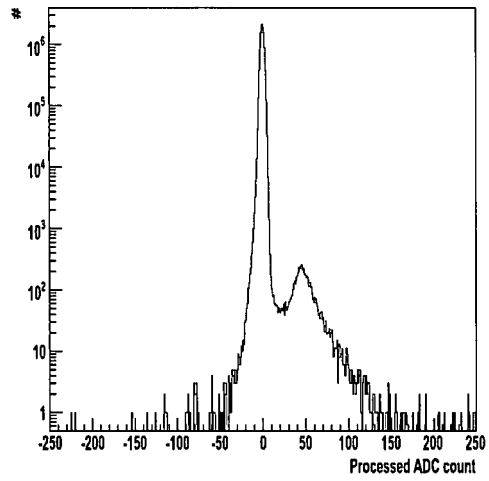

Figure 5.6: The processed ADC count for the ϕ sensor of M29. It clearly exhibits a noise peak on the left and a signal peak on the right

Sensor	Signal (e)	Noise (e)	S/N ratio
M26 R	47.4	1.9	24.6
M26 ϕ	48.4	1.8	27.7
M29 ϕ	45.2	1.9	23.9
M29 R	50.1	2.3	22.2
M23 R	59.4	2.5	23.7
M23 ϕ	49.3	1.9	26.1
M31 ϕ	51.2	2.2	22.8
M31 R	46.9	2.0	24.0
M30 R	46.8	2.2	21.7
M30 ϕ	46.9	1.9	24.7
M27 ϕ	45.6	1.9	24.5
M27 R	49.1	2.2	22.4

Table 5.2: The experimentally measured S/N ratio.

obtained. Further work on this analysis is required to remove the effects of crosstalk from the raw data before running the TELL1 board emulation.

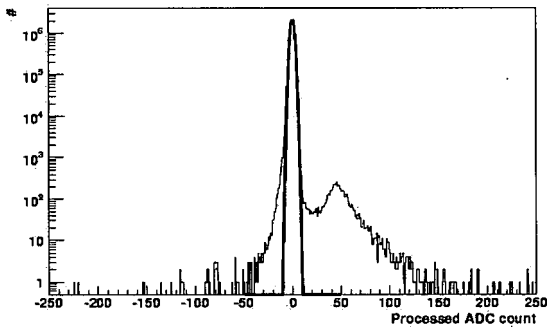

(a)

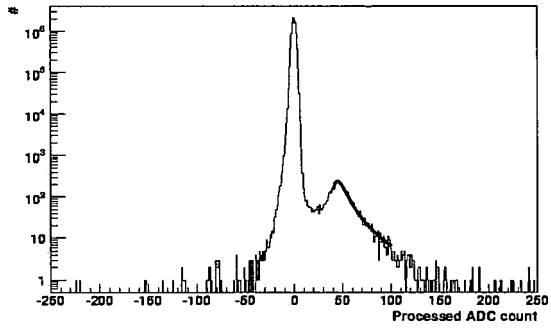

(b)

Figure 5.7: A plot of the Gaussian fit applied to the noise peak is shown in (a), with a mean value of 1.9. The Landau fit applied to the signal peak is shown in (b), yielding a most probable value of 45.2.

Chapter 6

A measurement of the reconstructed mass of the B_S meson

This chapter presents the selection and reconstructed mass measurement of the B_s meson that decays via the mechanism $B_s \to J/\psi(\mu^+\mu^-)\phi(K^+K^-)$. An estimation of the number of $B_s \to J/\psi(\mu^+\mu^-)\phi(K^+K^-)$ decays that will be observed in LHCb is discussed in Section 6.1. An introduction to the signal and background samples is given in Section 6.2 followed by a discussion of the event selection method in Section 6.4. In Section 6.5 a measurement of the B_s mass is discussed. Concluding remarks are given in Section 6.6.

6.1 Signal yield

The expected annual signal yield for a specific decay channel is directly proportional to the integrated luminosity of the colliding machine, this is shown by Equation 6.1. The total number of $b\bar{b}$ pairs produced is given by the product of the integrated luminosity, $\int \mathcal{L}$, and the estimated cross-section for $b\bar{b}$ production at the LHC, $\sigma_{b\bar{b}}$. At $\sqrt{s}$ of 14 TeV $\sigma_{b\bar{b}}$ is estimated to be $\sim 500\,\mu b$. A factor of two is required to obtain the total number of b quarks produced. The probability of a b quark hadronising into a specific B meson, f_B, and the visible branching fractions, Bf_{vis}, for the decay channel are also taken into account. The probability of a b quark hadronising into a B_s meson

is 10 %. The visible branching fraction for the $B_s \to J/\psi(\mu^+\mu^-)\phi(K^-K^-)$ decay is calculated using Equation 6.2, with the values required given in Table 6.1. The number of particles produced within 400 mrad of the z axis (the detector acceptance) is required. The efficiency of this calculation is known as the generator level efficiency, ϵ_{tot}. The generator level efficiency for the $B_s \to J/\psi(\mu^+\mu^-)\phi(K^+K^-)$ decay is 18 %.

$$s = \int \mathcal{L} \cdot \sigma_{b\bar{b}} \cdot 2 \cdot f_B \cdot Bf_{vis} \cdot \epsilon_{tot} \tag{6.1}$$

$$Bf_{vis} = Bf_{B_s \to J/\psi\phi} \cdot Bf_{J/\psi \to \mu^+\mu^-} \cdot Bf_{\phi \to K^+K^-} \tag{6.2}$$

Decay mode	Branching fraction
$B_s \to J/\psi\phi$	$(9.3 \pm 3.3) \times 10^{-4}$
$J/\psi \to \mu^+\mu^-$	$(5.93 \pm 0.06) \times 10^{-2}$
$\phi \to K^+K^-$	$(4.92 \pm 0.06) \times 10^{-1}$
$B_s \to J/\psi(\mu^+\mu^-)\phi(K^+K^-)$	27×10^{-6}

Table 6.1: The visible branching fraction for the $B_s \to J/\psi(\mu^+\mu^-)\phi(K^+K^-)$ decay channel. These values are taken from the PDG [24].

In one nominal year of data taking the LHC will have an integrated luminosity of 2 fb^{-1} yielding 0.97 million $B_s \to J/\psi(\mu^+\mu^-)\phi(K^+K^-)$ signal events within the LHCb acceptance. However, an integrated luminosity per year of 2 fb^{-1} is not expected until at least 2011 assuming that the LHC begins operation in autumn 2009. The first physics run will then take place in 2010 at $\sqrt{s}$ of 10 TeV, reaching an integrated luminosity of 0.2 fb^{-1} with $b\bar{b}$ cross section of 473 μb and yielding 92 thousand $B_s \to J/\psi(\mu^+\mu^-)\phi(K^+K^-)$ signal events within the LHCb acceptance.

6.2 Identifying the $B_s \to J/\psi(\mu^+\mu^-)\phi(K^+K^-)$ decay channel

Reconstructing the B_s meson and its decay products requires separating events that contain the $B_s \to J/\psi(\mu^+\mu^-)\phi(K^+K^-)$ decay from those which do not. The separation method is optimised by considering samples of Monte Carlo simulated events in the LHCb detector.

The analysis presented in this chapter has been carried out using events generated by the Monte Carlo generator, Pythia [31], at the LHCb target luminosity of $2\times10^{32}\,\mathrm{cm}^{-2}\mathrm{s}^{-1}$. A finite number of events have been produced and the complete data sets, corresponding to the number of events given in Table 6.2, have been used in this analysis.

Data set	Number of events
Signal	1200000
Inclusive B	520000
Inclusive J/ψ	3700000
Minimum Bias	940000

Table 6.2: The size of the signal and background samples used in the analysis presented in this chapter.

6.2.1 Signal sample

A signal sample contains particles from the decay under investigation. For the analysis discussed in this chapter the signal sample will contain positively and negatively charged muons and kaons, which form the J/ψ and ϕ candidates, respectively. Together the J/ψ and ϕ candidates form the B_s candidates.

An example of a $B_s \rightarrow J/\psi(\mu^+\mu^-)\phi(K^+K^-)$ event in the LHCb detector is shown in Figure 6.1.

Monte Carlo association is used to determine if the reconstructed particles are signal particles. If 70 % of the hits on a track are from the same Monte Carlo particle then the reconstructed particle is said to be *associated.* It is classed as a reconstructed signal particle.

6.2.2 Background sample

A background sample is composed of processes that mimic the signal process under investigation. It contains decays that have a similar topology to the $B_s \rightarrow J/\psi(\mu^+\mu^-)$ $\phi(K^+K^-)$ decay. The specific contents of a background sample depends on the type of background sample used. Three background samples have been used to estimate

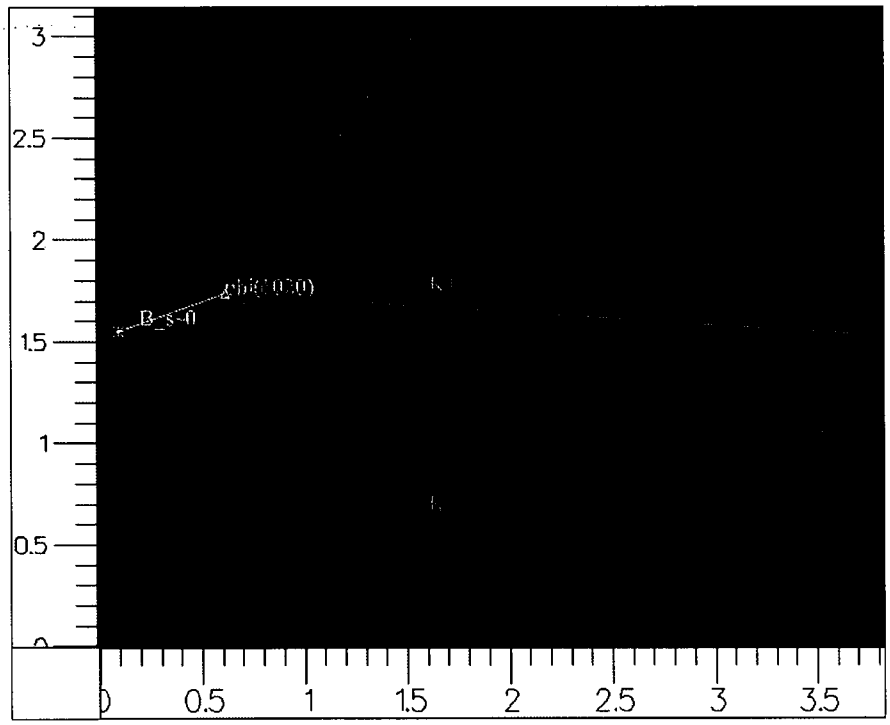

Figure 6.1: An event display showing a $B_s \to J/\psi(\mu^+\mu^-)\phi(K^+K^-)$ event in the LHCb detector.

the background processes presented in this chapter; Inclusive B, Inclusive J/ψ and Minimum Bias.

- **Inclusive B** consists of events containing b quarks, which hadronise into all flavours of B mesons. The final state particles decay according to the branching fractions in the PDG.

- **Inclusive J/ψ** contains events with real J/ψ particles that are produced promptly from the proton-proton interactions and not via a B decay. These may combine with a real or misidentified ϕ to mimic the signal.

- **Minimum bias** is composed of gluons and light quark (u, d, s) initiated jets. Random combinations of these tracks, occasionally with a real ϕ meson can mimic the signal. Fake J/ψ's can be made from pions and kaons that are mis-identified as muons as a result of *punch through*, where the particles are not stopped in the calorimeters and are then identified in the muon chambers as muons. Pions may also decay in flight, decaying into muons that produce hits in the muon system. Muons may also be produced from secondary interactions in the calorimeters.

6.3 Efficiency and Purity

The efficiency describes the performance of the selection cuts in identifying signal events. It is defined as the ratio of the number of signal B_s passing a given set of cuts and the number of signal B_s when no cuts are applied. The purity describes the effectiveness of the selection cuts at minimising background events. The purity of a selection criteria is obtained by dividing the number of signal B_s passing a given set of cuts by the sum of the number of the signal B_s and the number of background candidates passing the same set of selection cuts. These two quantities are conflicting. To obtain a high efficiency of identifying signal events the selection cuts must be weak enough not to remove too much signal, yet to obtain a highly pure sample of reconstructed signal particles the selection cuts must be tight enough not to contaminate the signal with background events.

6.4 Event selection

The selection of the $B_s \rightarrow J/\psi(\mu^+\mu^-)\phi(K^+K^-)$ decay channel is made by placing a set of requirements known as *selection cuts* on the kinematic variables of the particles in the decay. To effectively distinguish signal from background these cuts should preferentially be satisfied by signal events and not background events. The decay channel is broken down to consider the $J/\psi \rightarrow \mu^+\mu^-$ and $\phi \rightarrow K^+K^-$ decay mechanisms individually before considering the $B_s \rightarrow J/\psi(\mu^+\mu^-)\phi(K^+K^-)$ decay. In this section the pre-selections made by the trigger and using sets of standard particles are discussed in addition to the offline selection criteria.

6.4.1 Pre-selection

With real data the pre-selection will start at the trigger level with the L0 and HLT triggers performing selections on the decay modes of interest to suppress the minimum bias background whilst maintaining a high signal efficiency. Although the HLT2 trigger has a dedicated $B_s \rightarrow J/\psi(\mu^+\mu^-)\phi(K^+K^-)$ selection [83] this would not be used to make a measurement of the mass of the B_s because it places a cut on the mass of the B_s candidates requiring that it be within $0.3\,\mathrm{GeV/c^2}$ of the PDG reference value. This would clearly bias the measurement. Instead, the pre-selection of this decay mode could be made at the trigger level by using the Inclusive J/ψ trigger, of which there

are two; an unbiased lifetime selection and a selection that applies a cut on the impact parameter of the J/ψ candidates. The cuts employed in each of these selections are shown in Tables 6.3 and 6.4.

p_T (μ)	>0.5 GeV/c
p_T (J/ψ)	>1 GeV/c
mass ($\mu^+\mu^-$)	$\pm$0.07 GeV/c^2
J/ψ vertex χ^2/dof	<20

Table 6.3: The HLT2 unbiased Inclusive J/ψ selection criteria.

p_T (μ)	>0.7 GeV/c
mass ($\mu^+\mu^-$)	>2.9 GeV/c^2
Lifetime ($\mu^+\mu^-$)	100 fs
Impact parameter ($\mu^+\mu^-$)	> 0.02 mm

Table 6.4: The HLT2 Inclusive J/ψ lifetime biased selection criteria.

A sub-set of the Inclusive J/ψ trigger is the B$\rightarrow$J/ψX selection, which further tightens the cuts on the J/ψ, requiring that the muons have a p_T greater than 1.5 GeV/c and that the combined mass of the oppositely charged muons be within 0.05 GeV/c^2 of the J/ψ reference mass.

The starting point of the analysis presented in this chapter is the sets of standard particles that are pre-defined in DaVinci. The sets of standard particles have been constructed by applying weak conditions on the PID hypothesis of the protoparticle to assign a type to a particle. Each reconstructed track is assigned a PID by combining information from the RICH detectors, the calorimetry and the muon system. The RICH detectors are used to identify hadrons, namely π, K and p, they also have the ability to identify leptons. The calorimeters are used to identify electrons and the neutral particles, π^0 and γ, while the muon system provides muon identification. A different PID hypothesis may be assigned to a given particle by different sub-systems. A likelihood function is constructed using the hypotheses proposed by the relevant sub-detectors to obtain a combined probability that a particle is of a certain type. The

likelihood functions are given in Equation 6.3. L(e), L(μ) and L(h) are the likelihoods that a particle is an electron, muon and hadron, respectively. L_{RICH}, L_{CALO} and L_{MUON} refer to the hypothesis proposed by the RICH detectors, calorimeters and muon system, respectively.

$$\begin{aligned} L(e) &= L_{RICH}(e) \cdot L_{CALO}(e) \\ L(\mu) &= L_{RICH}(\mu) \cdot L_{MUON}(\mu) \\ L(h) &= L_{RICH}(h) \end{aligned} \tag{6.3}$$

A delta log likelihood (DLL) test is carried out, first assuming that the particle is a π^0 and comparing this to other PID proposals. The DLL function is given in Equation 6.4, where L(A) and L(B) are the likelihood of a particle being of type A and type B, respectively.

$$\Delta L_{AB} = lnL(A) - lnL(B) \tag{6.4}$$

The standard muon and kaon sets used in this analysis are defined by DLL(μ-π)>-3 and DLL(K-π)>0, respectively.

6.4.2 Selection cuts

The selection criteria placed upon the J/ψ, ϕ and the B_s candidates are presented in this section. Cuts on the p_T of the incoming particles and the combined mass of these particles are common to the J/ψ and ϕ selections. Common to all three selections is a cut on the χ^2/dof of the vertex fit between two tracks. In addition, the proper lifetime significance of the B_s candidates is taken into account.

The values of the selection cuts outlined for the J/ψ, ϕ and the B_s candidates have been determined by optimising the reference values presented in [33] and [82]. This optimisation has been achieved by considering how the data would be treated if it were data taken by the detector and not Monte Carlo generated data. With real data the number of true signal particles passing a selection, N_{true}, would be determined by Equation 6.5.

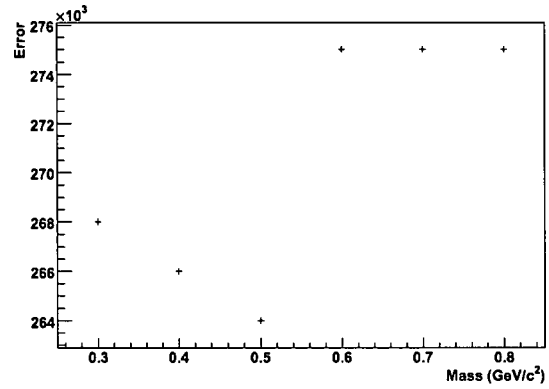

Figure 6.2: The error on the number of true particles passing a selection cut on the mass of the J/ψ as a function of the $|M_{\mu^+\mu^-}| < X$, where X is the value of the cut. The minima of the distribution indicates that a mass cut 0.05 GeV/c^2 is the optimal cut on the variable.

$$N_{true} = \frac{N - N_{bkg}}{\epsilon} \quad \pm \frac{\sqrt{N}}{\epsilon} \tag{6.5}$$

The total number of particle passing the selection criteria, N, is known from the data analysis. The number of background events passing the selection, N_{bkg} and the efficiency, ϵ, are estimates from Monte Carlo studies. The statistical error on this measurement enables the selection criteria to be optimised. A continuous variable that separates signal events from background events will have a large statistical error if the selection efficiency is low and a small error if the efficiency is high. Considering each variable as a function of the error on the number of true signal events obtained by cutting on that variable will yield a distribution such as that shown in Figure 6.2, where the cut on the mass of the J/ψ against the error on the number of true J/ψ's obtained using that cut is shown. The value of the cut at the minima of the distribution is taken as the optimal cut on that variable.

The plots presented in this chapter have been scaled to represent the data that will be taken in one nominal year of data taking at the LHC. The integrated luminosity of the machine is related to the number of events, N, by Equation 6.6. In one nominal year of data taking at $\sqrt{s}$ of 14 TeV the integrated luminosity is expected to be 2fb^{-1}. The cross section, σ, for the signal and background processes, along with the generator cut

efficiency, ϵ_{tot}, for that process is given in Table 6.5. The value with which to scale the number of particles in each sample is also shown.

$$\int \mathcal{L} = \frac{N}{\epsilon_{tot} \cdot \sigma} \tag{6.6}$$

Process	σ (fb)	ϵ_{tot}	Scaling factor
Signal	1.35×10^{6}	0.18	0.4
Inclusive B	6.98×10^{11}	0.4374	1.2×10^{6}
Inclusive J/ψ	2.86×10^{11}	0.198	3.1×10^{4}
Minimum Bias	102.9×10^{12}	1	2.2×10^{8}

Table 6.5: The cross section of the samples along with generator level efficiency of the sample and the factor required to scale the data to 2fb^{-1}.

J/ψ selection

The J/ψ is selected by imposing the following requirements on the reconstructed candidates:

- $p_T(\mu)$ >1 GeV/c
- $|M_{\mu^+\mu^-} - M_{J/\psi}| < 0.05\,\text{GeV/c}^2$
- $\chi^2 < 6$

The muons that combine to make the J/ψ have a high p_T, muons with a lower p_T tend to originate from the Minimum Bias background. The p_T distribution for positively charged muons is shown in Figure 6.3. Employing a momentum cut of 1 GeV/c on both the positive and negative muons to select J/ψ's retains 75 % of the signal.

Placing a requirement on the mass of a reconstructed resonance is a powerful method of eliminating background processes. A mass cut is applied by opening a window around the Particle Data Group (PDG) [24] reference value for the mass of the particle under consideration and selecting only those candidates within this window. The PDG reference values, along with their errors, for the J/ψ, ϕ and the B_s are given in Table 6.6. The mass distribution of the J/ψ candidates is given in Figure 6.4(a), the green dashed

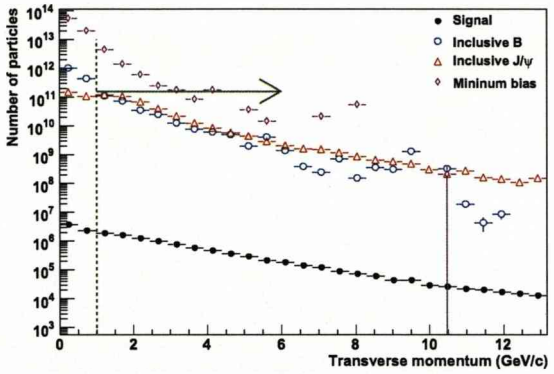

Figure 6.3: The p_T distribution of the positively charged muons. The dashed line shows the value of the cut and the solid green arrow indicates the direction of the cut.

Particle	Mass (GeV/c^2)
J/ψ	3.0970±0.00001
ϕ	1.0195±0.00002
B_s	5.3663±0.0006

Table 6.6: The PDG reference values for the mass of the J/ψ, ϕ and the B_s.

lines indicate that a mass window of 0.05 GeV/c^2 is opened around the reference mass of the J/ψ. Selecting J/ψ candidates based on their mass alone will separate real J/ψ's from background processes with an efficiency of 92 %.

The effect on the mass distribution of requiring that both of the muons have a p_T of greater than 1 GeV/c is shown in Figure 6.4(b). Applying both the mass and p_T cuts to select J/ψ's results in a signal efficiency of 69 %.

A vertex fit is applied to the muon pair to determine the position of the tracks in relation to each other. The slope of the tracks is altered to make them originate from a common point. The χ^2 per degree of freedom (dof) of the vertex fit gives an indication of the likelihood that the two tracks form a real vertex. The smaller the χ^2 the more likely it is that the two tracks originate from the same vertex. The distribution of the χ^2/dof of the vertex fit is shown in Figure 6.5(a). Applying a cut on this variable alone to select a J/ψ yields a selection efficiency of 93 %.

The effect on this distribution of first requiring that both of the muons have a p_T of

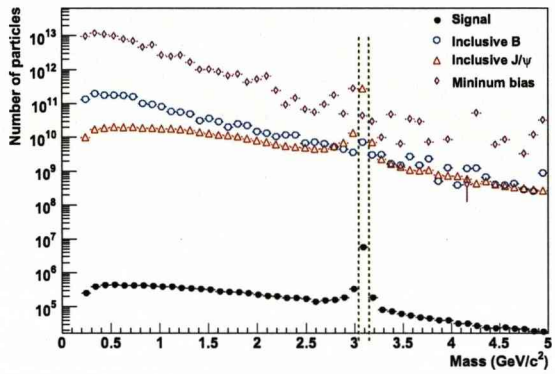

(a)

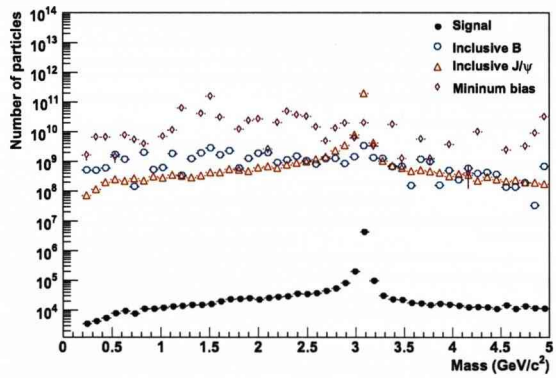

(b)

Figure 6.4: The mass distribution of the oppositely charged muon pair that form the J/ψ is shown in (a). The green dashed lines show the width of the mass window that is opened around the reference mass of the J/ψ. (b) shows the mass distribution after requiring that the muons have a p_T of greater than 1.0 GeV/c.

greater than 1 GeV/c and a combined mass of within 0.05 GeV/c^2 of the J/ψ mass can be seen in Figure 6.5(b). Cutting on all three variables selects J/ψ's with an efficiency of 65 %.

ϕ selection

The ϕ meson is selected by imposing the following criteria on the reconstructed candidates:

- p_T(K) $>$ 1.5 GeV/c
- $|M_{K^+K^-} - M_\phi| < 0.02$ GeV/c^2
- $\chi^2 < 25$

The p_T distribution for positive kaons is shown in Figure 6.6. Selecting ϕ's by requiring that both kaons have a p_T of greater than 1.5 GeV/c yields a signal efficiency of 52 %.

A cut selecting only those ϕ particles that are within 0.02 GeV/c^2 of the PDG reference value for the ϕ mass (see Table 6.6) is placed on the ϕ candidates as indicated by the green dashed line in Figure 6.7(a). Selecting ϕ's using this criterion alone yields a signal efficiency of 95 %.

The effect on this distribution of first requiring that both of the kaons have a p_T of greater than 1.5 GeV/c is shown in Figure 6.7(b). Selecting ϕ candidates by employing cuts on both the p_T and mass distributions yields a signal efficiency of 50 %.

The χ^2/dof of the vertex fit of the oppositely charged kaon pair is shown in Figure 6.8(a). A cut requiring a χ^2/dof of less than 25 is applied to this distribution. The χ^2/dof cut applied to the kaons that form the ϕ need not be as tight as that placed on the muons from a J/ψ because kaons that originate from a high momentum ϕ particle have a small opening angle, meaning that the vertex is difficult to reconstruct. As a result, the χ^2/dof of the vertex is insufficient in separating signal and background events. Applying this cut alone to select ϕ candidates identifies real ϕ's with an efficiency of 98 %.

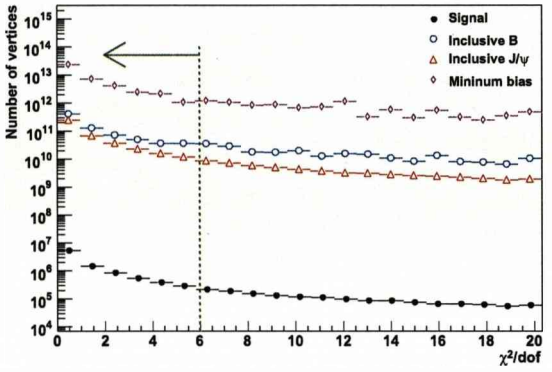

(a)

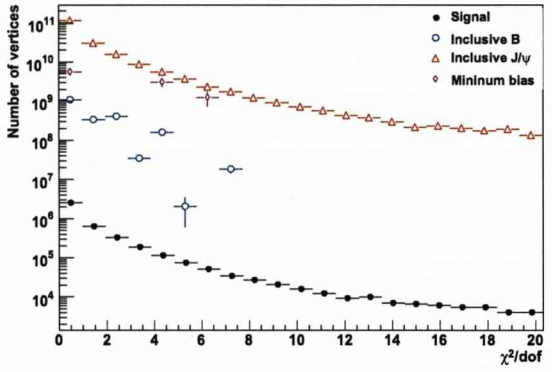

(b)

Figure 6.5: The χ^2/dof of the vertex fit applied to the oppositely charged muon pair is shown in (a). The green dashed line shows the value of the cut and the solid green arrow indicates the direction of the cut. (b) shows the χ^2/dof of the vertex fit after selecting muons with a p_T of greater than 1.0 GeV/c and requiring that the dimuon pair have a mass within 0.05 GeV/c^2 of the J/ψ mass.

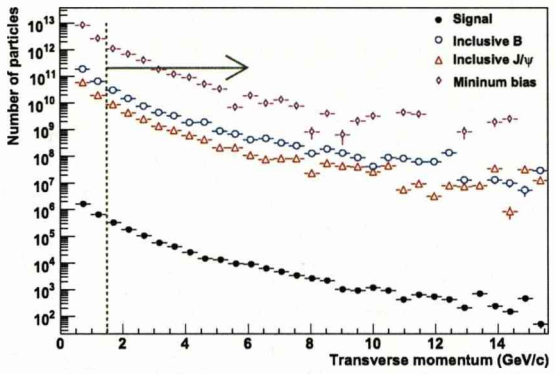

Figure 6.6: The p_T distribution of the positively charged kaons. The green dashed line shows the value of the cut and the solid green arrow indicates the direction of the cut.

The effect on the χ^2/dof of the vertex fit distribution of first requiring that the kaons have a p_T of 1.5 GeV/c and $|M_{K^+K^-}-M_\phi|<0.02\,\mathrm{GeV/c^2}$ is illustrated in Figure 6.8(b). Combining the three cuts to select real ϕ particles results in an efficiency of 49 %.

B_s selection

The B_s meson is reconstructed by combining the selected J/ψ and ϕ candidates from each event using the criteria outlined above. The criteria then placed on the B_s candidates are:

- χ^2/dof of vertex fit < 7
- Proper time significance > 5

The χ^2/dof of the vertex fit applied to the reconstructed J/ψ and ϕ is shown in Figure 6.9(a), indicating that only those B_s candidates where the four tracks form a vertex with a χ^2/dof of less than 7 are considered. Applying only a cut on the χ^2/dof of the vertex fit to select real B_s mesons yields a signal efficiency of 95 %.

Combining this cut with the J/ψ and ϕ selections results in the identification of real B_s mesons with an efficiency of 16 %.

An important requirement in reconstructing the B_s is that the primary and secondary

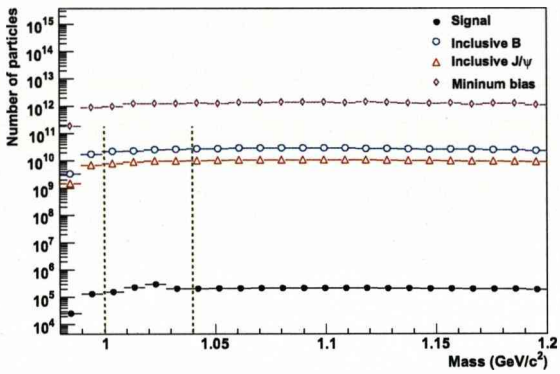

(a)

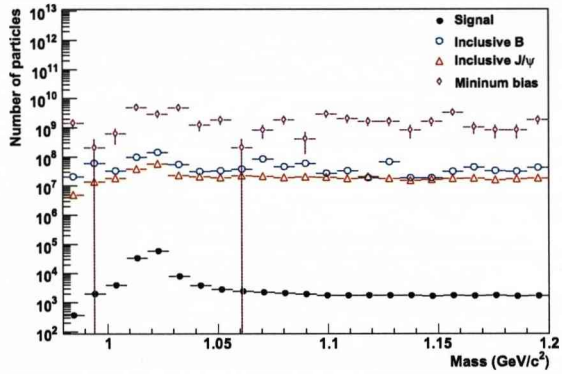

(b)

Figure 6.7: The mass distribution for the oppositely charged kaon pair is shown in (a). The green dashed lines show the width of the mass window that is opened around the reference mass of the ϕ. (b) shows the mass distribution after selecting kaons with a p_T of greater than 1.5 GeV/c.

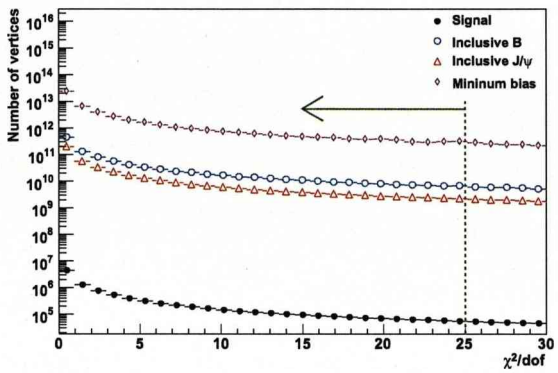

(a)

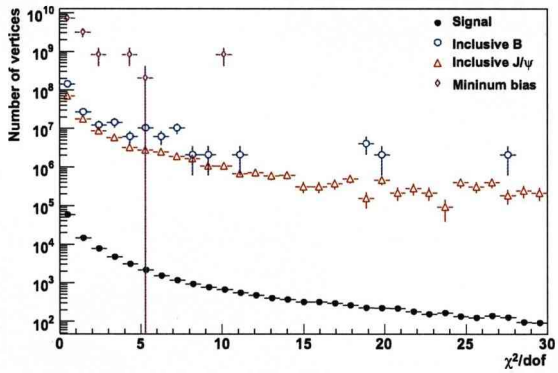

(b)

Figure 6.8: The χ^2/dof of the vertex fit applied to the oppositely charged kaon pair is shown in (a). The green dashed line shows the value of the cut and the solid green arrow indicates the direction of the cut. (b) shows the χ^2/dof of the vertex fit after selecting only those kaons with a p_T of greater than 1.5 GeV/c and requiring that the oppositely charged kaon pair have a mass within 0.02 GeV/c^2 of the ϕ mass.

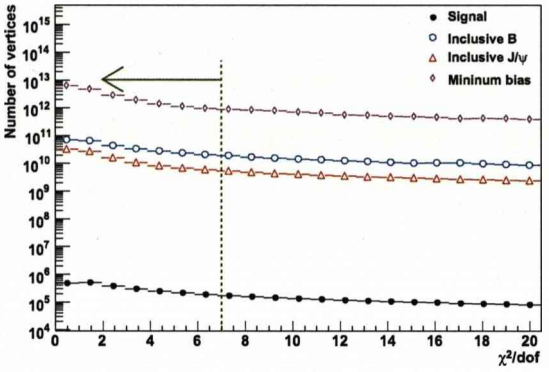

(a)

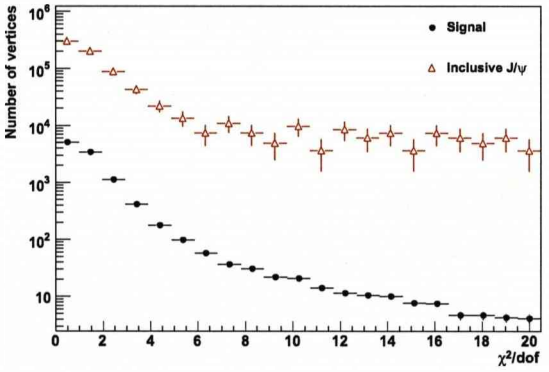

(b)

Figure 6.9: The χ^2/dof of the vertex fit applied to the J/ψ and ϕ combination is shown in (a) without any selection applied. The green dashed line shows the value of the cut and the solid green arrow indicates the direction of the cut. (b) shows the χ^2/dof of the vertex fit after the J/ψ and ϕ candidates have been selected.

vertices can be clearly identified. This is achieved by placing a requirement on the minimum lifetime of the B_s in the form of a proper time significance cut using the lifetime fitter. The proper lifetime significance is determined by taking the ratio of the lifetime, τ, of the B_s candidate and its error, σ_τ. The distribution of the proper lifetime significance is shown in Figure 6.9(a), the dashed green line indicates that only those B_s candidates with χ^2 of the proper lifetime significance greater than 5 are selected. Using only this selection criterion to select the B_s results in a signal efficiency of 39 %.

The selection cuts used to identify the B_s and its decay products are applied sequentially as shown in Table 6.7. Each row corresponds to the accumulation of that cut and the cuts defined above it.

The selection criteria presented in this section are summarised in Table 6.8 along with the reference values that have been taken from [33] and [82]. It can be seen that the cuts on the momentum of the ϕ candidates, and the cuts on the χ^2 of proper lifetime fit and the proper time resolution of the B_s candidates are not required in this analysis. The optimal cuts are somewhat tighter than the reference values.

6.5 B_s mass measurement

A measurement of the mass of the reconstructed B_s meson is obtained by employing all of the selection cuts discussed in Section 6.4.2 and applying a fit to the signal and remaining background distributions. Figure 6.11(a) shows the mass of the B_s meson after all of the cuts have been applied. The shape of the signal distribution can be described by a Gaussian function. The shape of the remaining Inclusive J/ψ background is not well defined because although the complete Inclusive J/ψ sample has been analysed the statistics are still too low. To better define the shape of the background the mass windows around the J/ψ and ϕ masses have been widened. The mass of the B_s meson with a mass window of 0.1 GeV/c^2 opened around the masses of both the J/ψ and ϕ is shown in Figure 6.11(b). The shape of the background can be deduced by comparing this Inclusive J/ψ background fitted with a one degree polynomial to that fitted with a two degree polynomial. The parameters of the two fits are given in Table 6.9. The third parameter of the second degree polynomial fit is consistent with zero, meaning that the

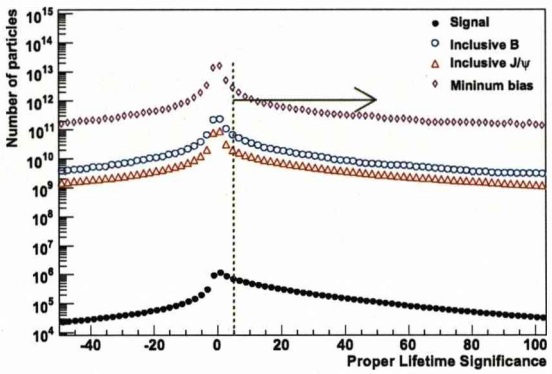

(a)

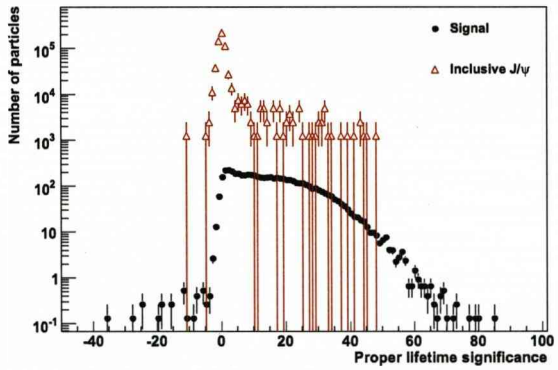

(b)

Figure 6.10: The χ^2 distribution of the proper time significance is shown in (a). The green dashed line shows the value of the cut and the solid green arrow indicates the direction of the cut. (b) shows the effect of a cut on the χ^2/dof of the vertex fit on the χ^2 of the proper time significance.

shape of the Inclusive J/ψ background is consistent with a one degree polynomial.

The lack of statistics means that to successfully fit the background distribution a better estimate of its shape is needed. The Inclusive J/ψ background distribution is fitted with a one degree polynomial function and pseudo-data is generated according to that function. Figure 6.13 shows the one degree polynomial fit applied to the reconstructed background data (a) and the generated pseudo-data (b). The pseudo-data is then added to the reconstructed signal data and the combined Gaussian and first degree polynomial fit is then applied across the whole range of the mass distribution as shown in Figure 6.14.

The mass of the reconstructed B_s meson is the mean value of the Gaussian fit, which is extracted from the fit parameters. The mass of the B_s meson is estimated to be 5.3686±0.0004 GeV/c^2, where the error quoted is statistical. Comparing this to the PDG reference value, 5.3663±0.0006,GeV/c^2, it can be seen that there is a 6σ discrepancy, which results from a systematic uncertainty that is larger than the statistical contribution.

The signal to background (S/B) ratio in 2fb^{-1} of data can be estimated from Figure 6.14. Taking a mass window of 0.04 GeV/c^2 around the reference mass of the B_s meson the S/B ratio is found to be 0.6.

6.5.1 Systematic uncertainties

In this section possible sources of systematic uncertainties are discussed along with methods of how they could be estimated with data. Systematic uncertainties from the following sources are considered:

- Detector calibration;
- Selection criteria;
- Fitting procedure.

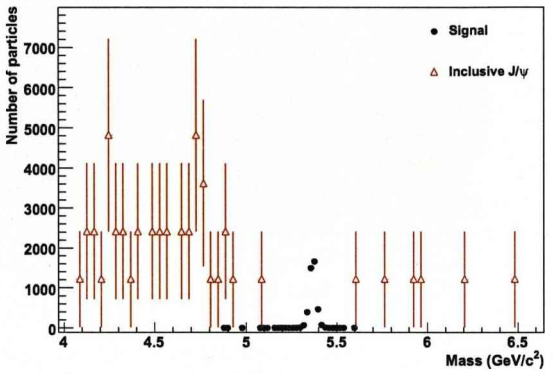

(a)

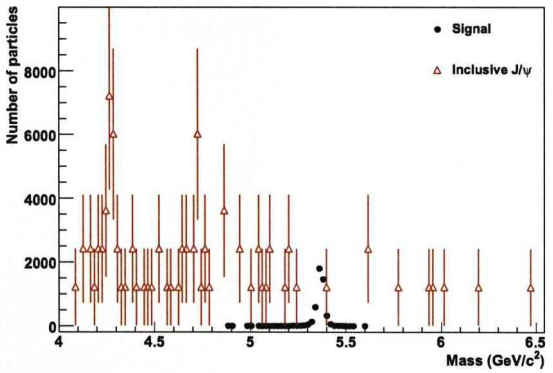

(b)

Figure 6.11: The B_s mass for the signal and remaining background data after all of the selection criteria have been applied is shown in (a). The mass windows opened around the PDG reference mass of the J/ψ and ϕ are $0.05\,GeV/c^2$ and $0.02\,GeV/c^2$, respectively. (b) shows the mass of the reconstructed B_s meson after extending the mass windows around the J/ψ and ϕ PDG reference mass to $0.1\,GeV/c^2$.

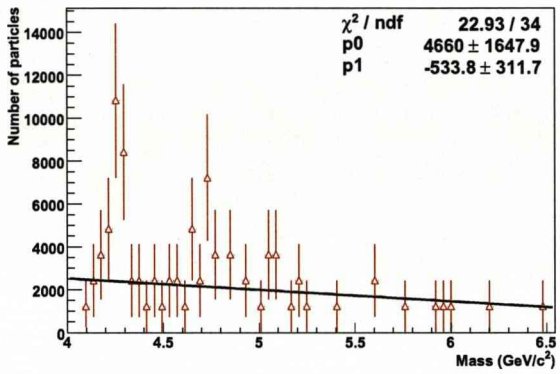

(a)

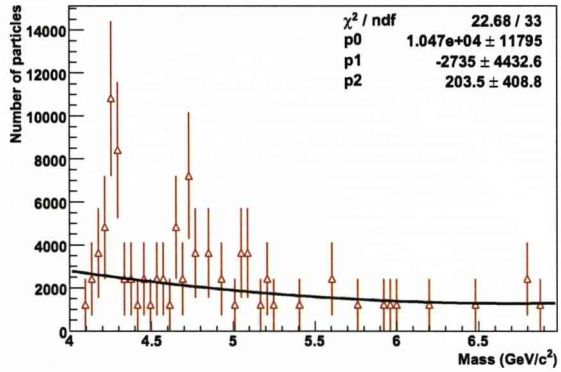

(b)

Figure 6.12: The Inclusive J/ψ background events that pass all of the selection cuts is shown with a one degree polynomial fit in (a) and a two degree polynomial fit (b). The third parameter of the two degree polynomial fit is consistent with zero, showing that the background data is best described by a one degree polynomial function.

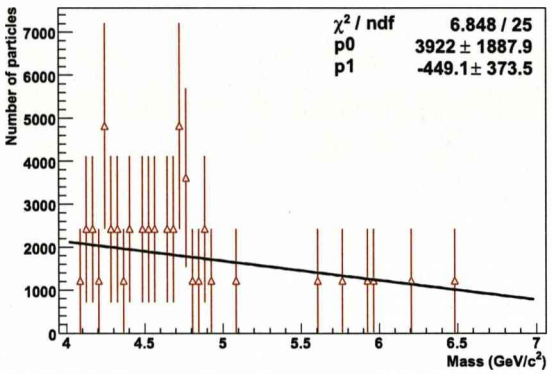

(a)

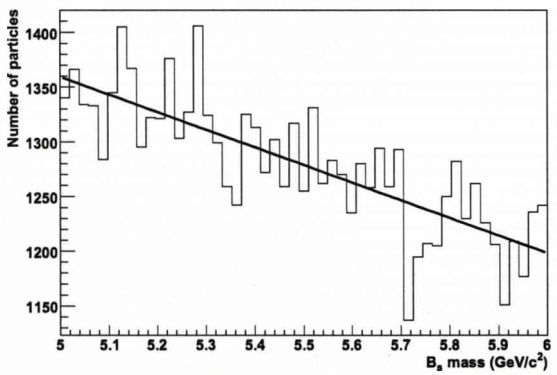

(b)

Figure 6.13: The Inclusive J/ψ background data that passes all of the selection cuts is shown in (a). The black line is a one degree polynomial fit applied to the data. (b) shows the pseudo-data generated from function applied to the background data.

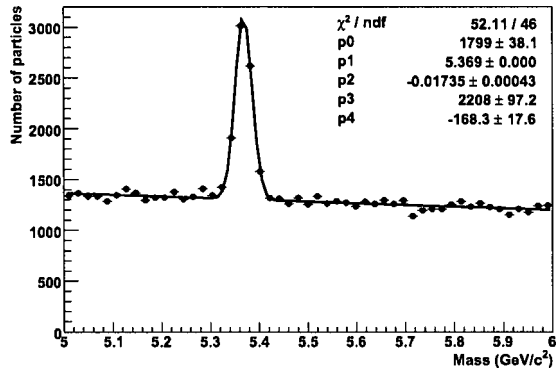

Figure 6.14: The signal and pseudo-data (markers) with a combined Gaussian and first degree polynomial fitted to the distribution (black line).

Detector calibration

An analysis relies upon the tracking of charged particles through the detector, making the possibility that the detector could be incorrectly calibrated an important source of systematic uncertainty. The alignment of the detector is the dominant systematic uncertainty associated with the calibration of the detector, however, the mapping of the magnetic field, the detector geometry and materials description may also have an effect. They all need to be precisely known and included in the detector simulation in order to make an accurate measurement of the mass of the B_s meson.

Misalignments in the tracking system will result in the incorrect reconstruction of a particle's path through the detector. This is of particular significance to the VeLo, which as discussed in Chapter 3 is retractable and will be retracted during each beam fill. Alignment has been a key issue during the construction of the VeLo. Precision tests have been carried out to ensure that the relative position of both of the R and ϕ sensors and the sensors to the pedestal are within the design specification (see Chapter 3, Section 3.2.1). Each half has also undergone a full metrology to determine the absolute positions of each of the components [84]. In addition, detailed studies have been carried out on the alignment of the VeLo halves with respect to each other and a software based correction has been developed to correct for misalignments during the mechanical retraction and insertion of the VeLo halves [85].

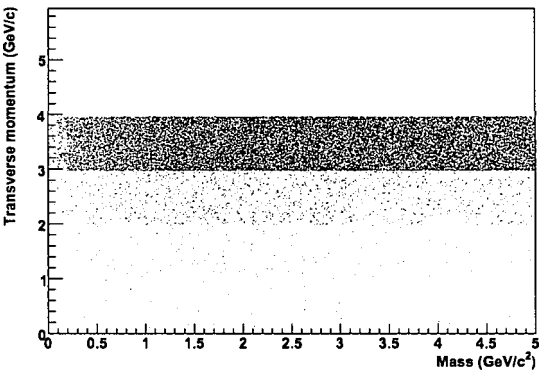

Figure 6.15: The mass of the reconstructed J/ψ candidates verses their p_T.

An inaccurate mapping of the magnetic field will lead to an incorrect measurement of a particle's momentum and in turn an incorrect measurement of its mass. The momentum of a particle is deduced from the degree of curvature of its track in the magnetic field, it is then used by the RICH detectors to calculate the mass of the particle. Figure 6.15 shows the mass of the reconstructed J/ψ verses its transverse momentum. Such a plot is used to check that the mapping of the magnetic field is correctly understood. This plot exhibits a linear behaviour. Any deviation from this would suggest that the magnetic field is not correctly modelled, but it could be corrected for by fitting, and applying this p_T dependent correction to the tracks before a physics analysis is carried out.

If too much material is included in the materials description of the detector there will be an increase in multiple scattering and the number of nuclear interactions that the particles undergo. This will have three effects:

- Reconstructed tracks in the VeLo will be less straight than the current simulation, which results in a worse position resolution.
- There will be an increase in the number of hits produced by secondary particles, resulting in a larger number of fake tracks.
- A larger fraction of reconstructed tracks will not traverse the entire detector, meaning that there will be fewer long tracks available for physics analyses.

At the start of data taking it is expected that there will be a maximum of 10 μm additional smear on impact parameter resolutions of 20-40 μm [78]. This will be removed with calibrations using data.

Selection criteria

Systematic uncertainties can be introduced via the particle selection process by applying cuts that can bias the measurement of the mass of the B_s meson. This can be tested by varying one cut at a time and plotting the mass of the reconstructed B_s meson obtained as a function of the cut value. The B_s mass should in theory remain constant.

The selection cuts applied by the HLT2 trigger may also contribute to the systematic uncertainty. This can be tested with data by comparing the mass of the B_s meson obtained using the different Inclusive J/ψ triggers.

Fitting procedure

The fitting procedure can provide a source of systematic uncertainties. The fitting procedure discussed in Section 6.5 is known as a *binned* fit, where the fit is applied directly to a histogram and uses the average value of the B_s mass in each bin. The sensitivity of this method can be tested by performing an *unbinned* fit. This method compiles a list of the values of the mass of the reconstructed B_s from each event and applies the fit directly to these values. The systematic uncertainties of the binned fitting method can be investigated by considering the sensitivity of the fits applied to the signal and background distributions.

The sensitivity of the Gaussian fit to the signal distribution can be tested by altering the bin width. The systematic uncertainty results from the definition of the shape of the Gaussian distribution. Reducing the bin width means an increased number of bins, which results in a more defined shape of Gaussian distribution and, therefore, a more accurate mean value of the B_s mass, but a larger statistical error. Increasing the bin width will yield a Gaussian distribution with a less defined shape but lower statistical errors. This procedure will determine the bin width that will optimise the reduction of both the systematic and statistical uncertainties.

The shape of the signal mass distribution must also be taken into consideration. The mass of a reconstructed particle actually takes the form of a Breit-Wigner distribution but a Gaussian distribution is a good approximation. Applying a combined Breit-Wigner and one degree polynomial fit to the signal and background distribution provides a means of testing if the shape of the signal distribution is correctly defined.

The shape of the background can be checked by fitting the distribution over a larger range. This should give the background a better defined shape and provide a check of whether the function used is correct.

6.6 Conclusions

In one nominal year of data taking at the LHC it is estimated that 0.97 million B_s mesons will be produced and decay as $B_s \rightarrow J/\psi(\mu^+\mu^-)\phi(K^+K^-)$. A Monte Carlo study has been conducted and a selection criteria for separating $B_s \rightarrow J/\psi(\mu^+\mu^-)\phi(K^+K^-)$ signal events from those of background events has been outlined. The $B_s \rightarrow J/\psi(\mu^+\mu^-)$ $\phi(K^+K^-)$ decay has been selected with an efficiency of 13 % and a S/B ratio of 0.6.

Using this selection criteria a measurement of the mass of the B_s meson has been made and found to be $5.3686 \pm 0.0004\,\mathrm{GeV/c^2}$, where the error quoted is statistical. Compared to the PDG reference value, $5.3663 \pm 0.0006,\mathrm{GeV/c^2}$, it can be seen that there is a $6\,\sigma$ discrepancy, which results from a systematic uncertainty that is larger than the statistical contribution. Possible sources of systematic uncertainty are: detector calibration; the selection criteria; the fitting procedure. It is expected that at the start of data taking mis-calibrations of the detector will result in a $10\,\mu$m additional smear on impact parameter resolutions of 20-40 μm, this will be corrected with data monitoring. Systematic uncertainties caused by the selection criteria can arise from offline selections or those made at trigger level. The functions used in the fitting procedure can introduce systematic uncertainties, as can the binning of the histograms. The systematic uncertainties on the B_s mass measurement have not been quantified but methods of how this could be done with data have been discussed.

	Signal	Inclusive B	Inclusive J/ψ	Minimum Bias	Efficiency (%)
Number of events	1200000	520000	3700000	940000	
Number of candidates	38482530	1661922	200097930	394962	
$p_T(\mu) > 1$GeV/c	14216820	53124	7675491	3753	73
$\lvert M_{\mu^+\mu^-} - M_{J/\psi}\rvert < 0.05\,\mathrm{GeV/c^2}$	10622340	3230	6312811	48	68
χ^2/dof of vertex fit $(\mu^+\mu^-) < 6$	9719588	1986	5808648	48	64
$p_T(K) > 1.5\,\mathrm{GeV/c}$	534329	60	147224	1	35
$\lvert M_{K^+K^-} - M_\phi\rvert < 0.02\,\mathrm{GeV/c^2}$	100640	0	4436	0	33
χ^2/dof of vertex fit $(K^+K^-) < 25$	95401	0	3902	0	32
B_s χ^2/dof of vertex fit < 7	44697	0	1391	0	16
B_s proper lifetime significance > 5	34966	0	185	0	13

Table 6.7: The $B_s \to J/\psi(\mu^+\mu^-)\phi(K^+K^-)$ selection criteria. Each row corresponds to the accumulation of that cut and the cuts defined above it.

Variable	Reference selection	Analysis selection
$p_T(\mu)$	$> 0.5\,\mathrm{GeV/c}$	$> 1.0\,\mathrm{GeV/c}$
$\lvert M_{\mu^+\mu^-} - M_{J/\psi} \rvert$	$< 0.05\,\mathrm{GeV/c^2}$	$\pm 0.05\,\mathrm{GeV/c^2}$
$(\mu^+\mu^-)$ vertex χ^2/dof	< 9	< 6
p_T(K)	$> 0.5\,\mathrm{GeV/c}$	$> 1.5\,\mathrm{GeV/c}$
(K^+K^-) vertex χ^2/dof	< 40	< 25
$p(K^+K^-)$	$> 12\,\mathrm{GeV/c}$	-
$\lvert M_{K^+K^-} - M_\phi \rvert$	$< 0.02\,\mathrm{GeV/c^2}$	$\pm 0.02\,\mathrm{GeV/c^2}$
B_s vertex χ^2/dof	< 20	< 7
B_s χ^2 of proper lifetime fit	< 100	-
B_s proper time resolution	$< 100\,\mathrm{fs}$	-
B_s proper time significance	> 5	> 5
$\lvert M_{B_s rec} - M_{B_s} \rvert$	$< 0.05\,\mathrm{GeV/c^2}$	-

Table 6.8: The selection criteria presented in this chapter compared to the reference criteria presented in [33].

	First degree polynomial	Second degree polynomial
Parameter	Value	Value
0	$(4.7\pm1.6)\times10^3$	$(1.1\pm1.2)\times10^4$
1	$(5.3\pm3.1)\times10^2$	$(2.7\pm4.4)\times10^3$
2		$(2.0\pm4.1)\times10^2$

Table 6.9: The fit parameters of the first and second degree polynomial functions fitted to the Inclusive J/ψ background.

Chapter 7

Conclusion

The Large Hadron Collider (LHC) is the world's most powerful particle accelerator, capable of colliding particles up to a centre of mass energy of 14 TeV. The LHC is in its final stages of commissioning and is expected to begin operation in autumn 2009. The LHCb experiment is one of the four detectors at the LHC, it will study the 10^{12} $b\bar{b}$ pairs that will be produced in a nominal year of data taking.

This thesis has incorporated two important bodies of research in preparation for data taking; the quality assurance and performance of the silicon modules that form the VeLo, the primary tracking detector of LHCb, and a Monte Carlo study of the $B_s \rightarrow J/\psi$ $(\mu^+\mu^-)\phi(K^-K^-)$ decay mode.

The analysis of testbeam data taken with ten final production VeLo modules is presented in Chapters 4 and 5, where the crosstalk found in the data and the signal to noise ratio of the silicon sensors are discussed, respectively. The testbeam studies show that the data taken with the VeLo modules exhibits the effects of crosstalk, a phenomenon by which the signal in one readout channel spreads into another. The analysis presented in Chapter 4 outlines a method of identifying, quantifying and correcting for the affect that crosstalk has on the testbeam data. Charge is migrated between the strips in two strip clusters found in Monte Carlo simulated data to make the distribution of the ratio of ADC values match that of the testbeam data. The values obtained to describe the charge migration can be used to correct the data for crosstalk. The quantification procedure found that the channels on both R and ϕ sensors have approximately

a 30 % anti-correlation with the channel that is read out immediately after it. The large amount of crosstalk seen in the data taken with the VeLo modules suggests that it arises from a combination of incorrect sampling time calibration and the absense of cable compensation at the testbeam. When the LHC begins operation the sampling time will be correctly tuned and the full 60 m cables will be used as opposed to the 15 m cables employed in the testbeam. This will reduce the amount of crosstalk observed in the data. Any remaining crosstalk can then be removed using the Finite Impulse Response (FIR) filter on the TELL1 board.

The signal to noise ratio of the silicon sensors is an important quantity required to monitor the performance of the VeLo modules. The signal to noise ratio is determined by performing pedestal subtraction and common mode correction on the raw data and then extracting the most probable value of the signal and mean value of the noise from the resultant processed data. The mean signal to noise ratio for the R sensors is 23.1 and for the ϕ sensors is 25.0. This is somewhat lower than the theoretical maximum. Possible reasons for this could be an incorrect sampling time and the effects of crosstalk on the data.

The selection of the $B_s \rightarrow J/\psi(\mu^+\mu^-)\phi(K^-K^-)$ decay channel resulting in a measurement of the mass of the B_s meson is presented in Chapter 6. In a nominal year of data taking the LHC will have an integrated luminosity of $2fb^{-1}$ resulting in the production of 0.97 million $B_s \rightarrow J/\psi(\mu^+\mu^-)\phi(K^-K^-)$ signal events within the LHCb detector acceptance. The selection criteria results in the reconstruction of the B_s mesons with an efficiency of 13 % and a signal to background ratio of 0.6. The reconstructed B_s meson was found to have a mass of $5.3686 \pm 0.0004\,\mathrm{GeV/c^2}$, where the error quoted is statistical. Comparing this to the PDG world average value, $5.3663 \pm 0.0006\,\mathrm{GeV/c^2}$, it is found that there is a $6\,\sigma$ discrepancy. This arises from a systematic uncertainty that due to time constraints has not been quantified. Possible sources of systematic uncertainties are; mis-calibration of the detector, a bias in the selection criteria and a bias in the fitting procedure. These sources have been discussed in detail and methods for quantifying their contributions to the systematic uncertainty have been outlined.

The measurement of the mass of the B_s meson using Monte Carlo simulated data

provides an estimate of the sensitivity of LHCb in measuring this quantity. Taking into account systematic uncertainties, it is considered that within one year of data taking at nominal luminosity the LHCb experiment should be able to make a measurement of the mass of the B_s meson that is competitive with the world's best average as stated by the Particle Data Group.

Bibliography

[1] I. J. R. Aitchison and A. J. G. Hey. *Gauge theories in particle physics*

[2] M. Srednicki. *Quantum Field Theory.* Cambridge University Press. ISBN 978-0-521-86449-7.

[3] The Particle Data Group. *Quantum Chromodynamics and its coupling.* http://pdg.lbl.gov/2009/reviews/rpp2009-rev-qcd.pdf

[4] The Particle Data Group. *SU(3) Isoscalar factors and representation matrices.* http://pdg.lbl.gov/2009/reviews/rpp2009-rev-su3-isoscalar-factors.pdf

[5] S. L. Glashow. *Partial-symmetries of Weak Interactions.* Nucl. Phys. B, 22, 1961.

[6] S. Weinberg. *A Model of Leptons.* Phys. Rev. Lett. 19, 1967.

[7] A. Salam. *Weak and electromagnetic interactions.* Elementary Particle Theory, ed:Svartholm, Almqvist and Wiksell,Stockholm 367, 1968.

[8] Y. Fukuda et al. *Evidence for oscillation of atmospheric neutrinos.* Phys. Rev. Lett. 81:1562-1567, 1998. e-Print: arXiv:hep-ex/9807003v2.

[9] R. Ofierzynski. *W boson mass and properties at LEP.* Prepared for the International Europhysics Conference on High Energy Physics (EPS-HEP2007), Manchester, England, 19-25 Jul 2007. Published in J.Phys.Conf.Ser.110:042019, 2008.

[10] F. Englert and R. Brout. *Broken Symmetry and the Mass of Gauge Vector Mesons.* Phys. Rev. Lett. 13 321-322, 1964.

[11] P. W. Higgs. *Broken Symmetries and the Masses of Gauge Bosons.* Phys. Rev. Lett. 13 508, 1963

[12] G. S. Guralnik, C. R. Hagen and T. W. B. Kibble *Global Conservation Laws and Massless Particles.* Phys. Rev. Lett. 13 585, 1964.

[13] E. Noether. *Invariant variation problems.*Nachr. d. König. Gesellsch. d. Wiss. zu Göttingen, Math-phys. Klasse. 235-257, 1918.

[14] J. H. Christenson, J. W. Cronin, V. L. Fitch, and R. Turlay. *Evidence for the 2π Decay of the K_2^0 Meson.* Phys. Rev. Lett., 13 138-140, 1964.

[15] S. L. Olsen. *Observation of large CP violation in the B-meson system.* Int.J.Mod.Phys.A17:2926-2935. 2002.

[16] N. Cabbibo. *Unitary symmetry and leptonic decays* Phys. Rev. Lett. 10. pp. 531-533. 1963.

[17] M. Kobayashi and T. Maskawa. *CP-Violation in the renormalisable theory of weak interactions.* Progress of Theoretical Physics. 49 652-657, 1972.

[18] L. Wolfenstein. *Parametrization of the Kobayashi-Maskawa Matrix.* Phys. Rev. Lett. 51 1945-1947. 1983.

[19] M. Dittmar et. al. *Parton Distributions.* e-Print: arXiv:0901.2504 [hep-ph].

[20] M. Talby on behalf of the D0 and CDF collaborations. *B_s^0 mixing and decays at the Tevatron.* Flavour Physics and CP Violation Conference, Bled, 2007. e-Print: arXiv:0707.1007v2 [hep-ex].

[21] C. Davies. *Precision lattice QCD calculations and predictions of fundamental physics in heavy quark systems.* Journal of Physics. Conference series 46 107-121, 2006.

[22] E. B. Gregory et. al. *Precision B(c) and B(s) mass calculations.* Presented at 26th International Symposium on Lattice Field Theory (Lattice 2008), Williamsburg, Virginia, 14-20 Jul 2008. e-Print: arXiv:0810.1845 [hep-lat].

[23] The ALEPH Collaboration. *First Measurement of the B_s meson mass.* Physics Letters B 311 425-436, 1993.

[24] W. M. Yeo et al. (Particle Data Group). http://pdg.lbl.gov

[25] G. Aad et al. The ATLAS experiment at the CERN Large Hadron Collider. JINST, 3(S08003). 2008.

[26] S. Chatrchyan et al. The CMS experiment at the CERN Large Hadron Collider. JINST, 3(S08004). 2008.

[27] K. Aamodt et al. The ALICE experiment at the CERN Large Hadron Collider. JINST, 3(S08002)

[28] A. Algusto Alves et al. The LHCb experiment at the CERN Large Hadron Collider. JINST, 3(S08005). 2008.

[29] G. Marchiori. *Measurement of the CKM angle gamma at BaBar.* arXiv:0810.0502 [hep-ex] 6 Oct 2008

[30] S. Burdin. *CP parameters of the B systems from Tevatron.* arXiv:0809.2886v3 [hep-ex] 4 Nov 2008

[31] T. Sjöstrand. *PYTHIA 6.4 Physics and Manual.* http://home.thep.lu.se/ torbjorn/pythia/lutp0613man2.pdf

[32] LHCb Vertex Locator Technical Design Report. CERN/LHCC/2001-011

[33] LHCb Reoptimized Detector Design and Performance. Technical Design Report. CERN/LHCC 2003-030

[34] T. Nakada. *The LHCb Experiment.* Acta Physica Polonica B. Vol 38 (2007)

[35] O. Behrendt. *The LHCb Vertex Locator.* EPS HEP 2007.

[36] P. R. Turner. *VELO Module Production - Sensor Testing.* LHCb-2007-072; CERN-LHCb-2007-072.

[37] J. L. Carroll, T.Huse. *VELO Module Production - Module Assembly.* LHCb-2007-076; CERN-LHCb-2007-076.

[38] T. Huse. *VELO Module Production - Sensor to Sensor Metrology.* LHCb-2007-085; CERN-LHCb-2007-085.

[39] S. Löchner, M. Schmelling. *The Beetle Reference Manual - chip version 1.3, 1.4 and 1.5.* LHCb-2005-105

[40] M. Wormald. *VELO Module Production - Pitch Adaptor and Chip Gluing.* LHCb-2007-075; CERN-LHCb-2007-075.

[41] M. Whitley, M. Wormald. *VELO Module Production - Back End Bonding.* LHCb-2007-078; CERN-LHCb-2007-078.

[42] M. Whitley, M. Wormald. *VELO Module Production - Front End Bonding.* LHCb-2007-079; CERN-LHCb-2007-079.

[43] M. Whitley, M. Wormald. *VELO Module Production - Sensor End Bonding.* LHCb-2007-080; CERN-LHCb-2007-080.

[44] J. L. Carroll. *VELO Module Production - Hybrid to Pedestal Matching.* LHCb-2007-086; CERN-LHCb-2007-086.

[45] The LHCb VeLo group. *P-type sensor review.* http://indico.cern.ch/conferenceDisplay.py?confId=14003

[46] R. Frei. *VELO Repeater Motherboard: RPT Board.* http://buytaert.home.cern.ch/buytaert/velo_repeater_motherboard.pdf

[47] G. Haefeli et al. *The LHCb DAQ interface board TELL1.* Nucl. Instrum. and Meth. A 560 (2006) 494502.

[48] A. Papadelis. *Characterisation and commissioning of the LHCb VELO detector.* CERN-THESIS-2009-044.

[49] LHCb RICH Technical Design Report. CERN/LHCC/2000-0037

[50] LHCb Magnet Technical Design Report. CERN/LHCC/2000-007

[51] LHCb Inner Tracker Technical Design Report. CERN/LHCC/2002-029

[52] LHCb Outer Tracker Technical Design Report. CERN/LHCC/2001-24

[53] LHCb Calorimeters Technical Design Report. CERN/LHCC/2000-0036

[54] A. Benvenuti et al. *An electromagnetic shashlik calorimeter with longnitudinal segmentation.* arXiv:hep-ex/9902008v1 6 February 1999.

[55] LHCb Muon System Technical Design Report. CERN/LHCC/2001-010

[56] LHCb Trigger System Technical Design Report. CERN/LHCC/2003-031

[57] A description of the LHCb High Level Trigger (HLT). http://lhcb-trig.web.cern.ch/lhcb-trig/HLT/HltDescription.htm

[58] H. Ruiz. *The LHCb trigger: algorithms and performance.* CERN-LHCb-CONF-2009-024.

[59] M. Cattaneo et al. *Status of the GAUDI event-processing framework* Proc. of CHEP 2001

[60] The Gauss Project. http://lhcb-release-area.web.cern.ch/LHCb-release-area/DOC/gauss/

[61] S. Agostinelli et al. *Geant4 - a simulation toolkit.* Nucl. Instrum. and Meth. A. Volume 506, Issue 3, Pages 250-303. July 2003.

[62] The Boole Project. http://lhcb-release-area.web.cern.ch/LHCb-release-area/DOC/boole/

[63] The Brunel Project. http://lhcb-release-area.web.cern.ch/LHCb-release-area/DOC/brunel/

[64] The DaVinci Project. http://lhcb-release-area.web.cern.ch/LHCb-release-area/DOC/davinci/

[65] C. Parkes, T. Szumlak. *Description of the Vetra Project and its Application for the VELO Detector.* LHCb-2008-022; CERN-LHCb-2008-022.

[66] http://indico.cern.ch/conferenceDisplay.py?confId=8974. November 2006

[67] https://twiki.cern.ch/twiki/bin/view/LHCb/HappyPionTable

[68] G. Haefeli, A. Gong. *LHCb VELO and ST clusterization on TELL1.* EDMS 690585. January 2006.

[69] University of Liverpool LHCb Group. *Vertex Locator Module Production Database.* http://hep.ph.liv.ac.uk/lhcb/. 2005-2007

[70] K. Hennessy. *Beetle Pipeline and Header Analysis.* http://indico.cern.ch/conferenceDisplay.py?confId=7233. October 2006

[71] G. Haefeli, A. Gong. *VELO and ST Non-Zero Suppressed Bank Data Format.* EDMS 692431. January 2006.

[72] D. E. Hutchcroft. *Private Communication.* August 2007.

[73] http://www.fresco.org.uk/minuit/cern/node30.html

[74] http://www.statsoft.com/textbook/sttable.html

[75] L. Landau. *On the energy loss of charged particles by ionisation.* J. Physics. vol 8 p201. 1944.

[76] C. Leroy et al. *Study of charge collection and noise in non-irradiated and irradiated silicon detectors.* Nucl. Inst. and Meth. A388 (1997) 289-296.

[77] D. E. Jones. *Noise and Pedestal Calculation Method Studies on LHCb Velo.* LHCb-2007-108; CERN-LHCb-2007-108.

[78] Private communication with D. E. Hutchcroft. 2006.

[79] Private communication with G. Casse and N. A. Smith. 2005.

[80] Private communication with I. Tsurin. 2009.

[81] K. Hennessy. University College Dublin.
http://www.ucd.ie/physics/research/particle/downloads/sntalk.pdf

[82] G. Raven. *Selection of the $B_s \rightarrow J/\psi\phi$ and $B^+ \rightarrow J/\psi K^+$.* LHCb 2003-118.

[83] G. Conti and A. Hitcheur. *Trigger selection of $B \rightarrow J/\psi(\mu\mu)X$ channels.* LHCb-2008-071; CERN-LHCb-2008-071.

[84] M. John. *VELO module metrology.* LHCb-2008-014; CERN-LHCb-2009-014.

[85] S. Viret, C. Parkes and M. Gersabeck. *Alignment procedure of the LHCb Vertex Detector.* Nucl. Instr. and Meth. A596 (2008) 157-163.